

Constraints on neutrino oscillation parameters implied by OPERA experiment data

Kliček, Budimir

Doctoral thesis / Disertacija

2018

Degree Grantor / Ustanova koja je dodijelila akademski / stručni stupanj: **University of Zagreb, Faculty of Science / Sveučilište u Zagrebu, Prirodoslovno-matematički fakultet**

Permanent link / Trajna poveznica: <https://um.nsk.hr/um:nbn:hr:217:743192>

Rights / Prava: [In copyright](#)/[Zaštićeno autorskim pravom.](#)

Download date / Datum preuzimanja: **2024-07-15**



Repository / Repozitorij:

[Repository of the Faculty of Science - University of Zagreb](#)



June 13, 2018 16:06
Printed version



University of Zagreb

Faculty of Science
Department of Physics

Budimir Kliček

**CONSTRAINTS ON NEUTRINO
OSCILLATION PARAMETERS IMPLIED
BY OPERA EXPERIMENT DATA**

DOCTORAL THESIS

Zagreb, 2018.



University of Zagreb

Faculty of Science
Department of Physics

Budimir Kliček

**CONSTRAINTS ON NEUTRINO
OSCILLATION PARAMETERS IMPLIED
BY OPERA EXPERIMENT DATA**

DOCTORAL THESIS

Supervisors:
dr. sc. Mario Stipčević
dr. sc. Stefano Dusini

Zagreb, 2018.



Sveučilište u Zagrebu

Prirodoslovno-matematički fakultet
Fizički odsjek

Budimir Kliček

**OGRANIČENJA NA PARAMETRE
NEUTRINSKIH OSCILACIJA
UVJETOVANA PODACIMA
EKSPERIMENTA OPERA**

DOKTORSKI RAD

Mentori:
dr. sc. Mario Stipčević
dr. sc. Stefano Dusini

Zagreb, 2018.

Supervisor information

Dr. sc. Mario Stipčević is a senior scientific associate at the Ruder Boškovic Institute in Zagreb, Croatia (RBI) and the author of over 85 scientific articles in physics cited over 2100 times. He has given 11 invited conference talks published 17 popular articles in the field of electronics and is a holder of one granted patent. In 1991 he joined NOMAD neutrino experiment at CERN where he was offered a scholarship for a PhD in high energy physics at CERN's experiment Atlas. He obtained his PhD in 1994 at L'Universite de Savoie, Chambéry, France. Continuing his work in neutrino physics, he worked on NOMAD and NOMAD-STAR, notably on charm background. In 2004 he joined the OPERA neutrino experiment at Gran Sasso as a leader of the Zagreb group. In 2011 he was a Fulbright scholar at University of California Santa Barbara (UCSB), followed by one year sabbatical leave at UCSB and Duke University, working on high speed quantum cryptography. Since 2014, he is a head of Photonics and Quantum Optics Research Unit of Centre of Excellence for Advanced Materials and Sensing Devices at RBI. Since 2017 he is an editorial board member of Nature's Scientific Reports. Research interests: neutrino physics, quantum information and entanglement, holography, APD based single photon detectors. URL: <http://www.irb.hr/eng/People/Mario-Stipcevic>

Dr. sc. Stefano Dusini is a senior scientist of Istituto Nazionale di Fisica Nucleare (Italian National Institute for Nuclear Physics research) in Padova, an author of 242 peer reviewed articles in physics cited over 13,000 times, 12 invited conference talks. After the PhD obtained at University of Trento (Italy) in 1998, with a thesis on the search for Higgs boson decaying to 4μ at LHC using Neural Network techniques, he joined ZEUS collaboration. His activity was concentrated on the search for excited fermions in electron-proton collision at HERA collider (DESY, Hamburg Germany). In 2001 Stefano Dusini signed, with the INFN group of Padova, the OPERA experimental proposal with the commitment to construct and run the the RPC system of the muon spectrometers of the OPERA detector. He was heavily involved in the definition of the muon spectrometer and in the test of the RPC detectors. He gave also an important contribution to the OPERA MC simulation framework. Stefano Dusini was very active in the OPERA analysis working group, working on the electronic detectors for the estimation of event rate in OPERA and on emulsion MC for the estimation of background suppression with the OPERA *Track Follow Down technique*. In 2008 Stefano Dusini was nominated OPERA Deputy Physics Coordinator remaining in charge till 2014. In 2015 he joined the Euclid Consortium as AIV Manager of the Warm Electronics of the NISP instrument of the ESA space mission Euclid. He is also member of the JUNO collaboration and coordinator of the analysis working group of the "3" PMT system" of JUNO.

*Dedicated to late prof. dr. sc. Ante Ljubičić,
who searched for the invisible.*

Abstract

The OPERA experiment in the CNGS beam was designed to measure the appearance of tau neutrinos in the high purity muon neutrino beam. The physical run lasted for five years in the period 2008 – 2012 with the total accumulated CNGS intensity of $1.797 \cdot 10^{20}$ protons-on-target. The primary goal was achieved by observing five tau neutrino candidate events, which corresponds to the significance of the ν_τ observation of more than 5σ . In addition to this, constraints on $|\Delta m_{32}^2|$ mass splitting in the $\nu_\mu \rightarrow \nu_\tau$ channel, and the mixing angle θ_{13} in the $\nu_\mu \rightarrow \nu_e$ channel were obtained from the experimental data. This thesis produces a constraint on $|\Delta m_{32}^2|$ dominated by $\nu_\mu \rightarrow \nu_\mu$ disappearance channel by analysing the OPERA electronic detector data. Unlike appearance channels, the disappearance channel is dominated by the systematic uncertainty of the CNGS neutrino beam, which is in absence of a near detector estimated to be (10–20)%. To overcome this limitation, NC interaction rate was used to normalize the flux by basing the analysis on the measurement of NC/CC event ratio observed in the OPERA electronic detectors. A special statistical model was constructed to properly extract confidence intervals from the measured data. A dedicated Monte Carlo simulation was produced for the purposes of this work, which was also used for the $|\Delta m_{32}^2|$ and θ_{13} constraints by the OPERA Collaboration. Using the constructed statistical model and the large dedicated MC sample, an upper limit of $|\Delta m_{32}^2| < 4.1 \cdot 10^{-3} \text{ eV}^2$ at 90% C.L. was obtained in this work.

Keywords: neutrino, oscillation, OPERA, CNGS, appearance, disappearance, LNGS, observation, long-baseline

Expanded abstract in Croatian

Prošireni sažetak na hrvatskom jeziku

Neutrini međudjeluju s materijom samo preko slabih sila. Međudjelovanje je moguće preko nabijenih slabih struja (eng. Charged Current, CC) u kojima se neutrino nakon raspršenja pretvara u lepton odgovarajućeg okusa, te neutralnih slabih struja (eng. Neutral Current, NC) u kojima neutrino nakon raspršenja ostaje neutrino. Standardni model fizike čestica predviđa tri okusa neutrina: elektronski, mionski i tau.

Teorija oscilacija neutrina predviđa mogućnost opažanja¹ neutrina u stanju okusa različitom od onoga u kojemu je nastao. Vjerojatnost da će neutrino izvornog stanja okusa α međudjelovati s materijom preko nabijenih slabih sila u stanju okusa β dana je jednadžbom (2.42). Za tri generacije neutrina vjerojatnost oscilacija u vakuumu je u potpunosti definirana sa 6 parametara: dvije razlike kvadrata masa neutrina Δm_{21}^2 , Δm_{32}^2 definirane jednadžbom (2.41a) i četiri elementa matrice miješanja neutrina (2.57) u koju ulaze kutovi miješanja θ_{12} , θ_{23} , θ_{13} i CP narušavajuća faza δ_{CP} .

U vrijeme pisanja ovoga doktorskoga rada, svi parametri oscilacija neutrina osim δ_{CP} izmjereni su s dovoljnom preciznošću da se isključe moguće degeneracije u teoriji². Svjetski prosjek eksperimentalnih vrijednosti parametara prikazan je u Tablici 2.4.

U modernoj fizici oscilacija neutrina, parametri oscilacija mjere se opažanjem sunčevih neutrina, reaktorskih neutrina, atmosferskih neutrina i ubrzivačkih neutrina. Sunčevi neutrini nastaju pri fuzijskim reakcijama u Suncu. Reaktorski neutrini nastaju beta raspadima fisijskih produkata u nuklearnim reaktorima. Atmosferski neutrini nastaju u raspadima sekundarnih mezona proizvedenih pri sudaru protona i jezgara helija iz kozmičkih zraka sa gornjim slojevima atmosfere. Ubrzivački neutrini nastaju slično kao i atmosferski samo što se protoni ubrzavaju u ubrzivačima, a meta nije atmosfera nego neki materijal postavljen u laboratoriju.

Sunčevi neutrini su izvorno elektronskog okusa i energija otprilike od 100 keV do 2.0 MeV, a reaktorski neutrini su elektronski antineutrini energija otprilike od 2 MeV

¹Opažanje okusa neutrina moguće je samo preko opažanja okusa nabijenog leptona proizvedenog u CC raspršenjima. To znači da je okus neutrina definiran CC međudjelovanjima.

²Degeneracija se događa ako je bilo koja razlika kvadrata masa $\Delta m_{ij} = 0$ ili ako za bilo koji kut miješanja vrijedi $\sin \theta_{ij} = 0$ ili $\cos \theta_{ij} = 0$. U tim slučajevima je broj efektivnih generacija neutrina manji od 3.

do 8 MeV. Pošto je masa miona oko 105 MeV, energija tih neutrina nije dovoljna za proizvodnju miona preko nabijenih slabih struja. Zbog toga se oscilacije tih neutrina mogu promatrati samo u kanalu nestanka okusa, tj. promatra se vjerojatnost oscilacija $\nu_e(\bar{\nu}_e) \rightarrow \nu_e(\bar{\nu}_e)$. Eksperimenti koji mjere sunčeve neutrine osjetljivi su na Δm_{21}^2 i θ_{12} , kao i reaktorski eksperimenti koji nisu blizu reaktora (jedini takav eksperiment je KamLAND u Japanu prosječne udaljenosti od reaktora oko 180 km). Reaktorski eksperimenti koji se nalaze blizu reaktora (~ 1.5 km) osjetljivi su na Δm_{32}^2 i θ_{13} .

Tok atmosferskih neutrina sastavljen je od neutrina i antineutrina koji su izvorno mionskog ili elektronskog okusa. Mionski (anti)neutrini nastaju pri raspadu sekundarnih mezona i miona, a elektronski većinom pri raspadu miona. Oni imaju vrlo širok spektar energija te mogu preko CC raspršenja proizvesti i mione i tau leptone. Zbog toga su pogodni za opažanje oscilacija neutrina i u kanalu nestanka i u kanalu pojave okusa³. Atmosferski neutrini najpogodniji su za mjerenje oscilacijskih parametara Δm_{32}^2 i θ_{23} u kanalu nestanka, dok je manjom preciznošću moguće mjeriti Δm_{32}^2 , θ_{23} i θ_{13} u kanalu pojave okusa.

Ubrzivački neutrini su mionski neutrini ili antineutrini. Iako nastaju istim fizikalnim procesima kao atmosferski neutrini, u laboratorijskim uvjetima moguće je izabrati glavnu komponentu okusa. Njihova energija ovisi o energiji protona koji se sudaraju s metom, a današnji eksperimenti pokrivaju energetska područja neutrina otprilike od 1 GeV do 40 GeV. Detektori neutrina u tim eksperimentima udaljeni su od izvora par stotina kilometara. Pomoću njih se mjere isti parametri oscilacija neutrina kao i pomoću atmosferskih, no mjerenja su preciznija jer se ovdje radi o kontroliranim laboratorijskim uvjetima.

Svjetski prosjek parametara Δm_{21}^2 i θ_{12} izračunat je iz kombinacije mjerenja eksperimenta KamLAND [1] koji mjeri reaktorske neutrine na velikoj (180 km) udaljenosti od reaktora i rezultata eksperimenata koji opažaju sunčeve neutrine.

Parametar θ_{13} mjeri se u kanalu nestanka reaktorskih neutrina u eksperimentima Daya Bay [2, 3], RENO [4] i Double Chooz [5] u kojima su detektori postavljeni na malim udaljenostima (~ 1.5 km) od reaktora, te u kanalu pojave okusa u ubrzivačkim neutrinским eksperimentima kao T2K [6], MINOS [7] i OPERA [8, 9]. Mjerenja

³Na primjer može se promatrati vjerojatnost oscilacija $\nu_\mu \rightarrow \nu_e$.

reaktorskih neutrina su preciznija od mjerenja ubrzivačkih neutrina ponajviše zbog intenzivnijeg toka neutrina, pa samo ona ulaze u izračun svjetskog prosjeka za θ_{13} .

Parametar θ_{23} mjere eksperimenti koji opažaju atmosferske i ubrzivačke neutrine u kanalu nestanka izvornog okusa. Svjetski prosjek izračunat je iz mjerenja ubrzivačkih neutrina u eksperimentima $\text{NO}\nu\text{A}$ [10], T2K [11] i MINOS [12], te iz mjerenja atmosferskih neutrina u eksperimentu Ice Cube [13].

Razlika kvadrata masa Δm_{32}^2 može se mjeriti u reaktorskim eksperimentima u kojima je detektor blizu reaktora opažanjem nestanka elektronskih antineutrina, te u atmosferskim i ubrzivačkim eksperimentima mjerenjem nedostatka mionskih (anti)neutrina ili mjerenjem pojave okusa u kanalima $\nu_\mu \rightarrow \nu_e$ i $\nu_\mu \rightarrow \nu_\tau$. Svjetski prosjek izračunat je iz rezultata mjerenja reaktorskih eksperimenata Daya Bay [2] i RENO [4], iz rezultata ubrzivačkih eksperimenata $\text{NO}\nu\text{A}$ [10], T2K [11] i MINOS [12], te atmosferskog eksperimenta Ice Cube [13]. OPERA je jedini eksperiment do sada koji je objavio rezultat mjerenja Δm_{32}^2 u pojavnom kanalu [14, 15]. U ovome radu postavljeno je dodatno ograničenje na taj parametar iz podataka eksperimenta OPERA preko analize u kojoj je glavni kanal oscilacija nestanak mionskih neutrina.

Eksperiment OPERA dizajniran je za opažanje pojave tau neutrina u kanalu oscilacija $\nu_\mu \rightarrow \nu_\tau$ kroz neposredno opažanje tau leptona proizvedenih u CC raspršenjima tau neutrina. OPERA opaža neutrine iz ubrzivačkog snopa CNGS [16] koji se proizvodio pomoću protona ubrzavanih u CERN-ovom SPS ubrzivaču. CNGS snop se prvenstveno sastoji od mionskih neutrina s energijama u rasponu od 1 GeV do 40 GeV. Detektor OPERA nalazio se u 732 km udaljenom podzemnom laboratoriju LNGS u Italiji.

Tau leptoni koje proizvode neutrinu energija CNGS snopa prolaze malu udaljenost od oko 1 mm prije nego što se raspadnu na neutrine i nabijene čestice⁴. Da bi se opazio tako kratki trag čestice potrebna je velika prostorna razlučivost detektora, dok je s druge strane potrebno da detektor ima veliku masu zbog vrlo malog udarnog presjeka neutrina.

Velika prostorna razlučivost postignuta je upotrebom nuklearnih emulzija koje imaju razlučivost reda veličine 1 μm , dok je glavna meta na kojoj se neutrinu raspršuju olovo. Osnovni element detektora OPERA je emulzijska maglena komora⁵, tzv. ECC cigla, koja

⁴Glavni modovi raspada tau leptona prikazani su u tablici A.1.

⁵Eng. emulsion cloud chamber, ECC

se sastoji od naizmjenice posloženih listova emulzije i pločica olova (slika 3.4.). Dvije mete za neutrine detektora OPERA sastojale su se od ukupno ~ 150 tisuća cigli ukupne mase 1.25 kt. ECC cigle su bile okružene scintilatorskim detektorima koji su služili da bi se odredilo u kojim su se ECC ciglama dogodila raspršenja neutrina. Iza svake od meta nalazio se magnetni spektrometar koji je služio za određivanje količine gibanja nabijenih čestica, osobito miona.

Eksperiment OPERA je nakon petogodišnjeg perioda prikupljanja podataka pronašao 5 događaja klasificiranih kao međudjelovanja tau neutrina. S obzirom da je očekivani broj pozadinskih⁶ događaja 0.25, vjerojatnost da je svih 5 opaženih događaja rezultat pozadine iznosi $3.4 \cdot 10^{-7}$, što znači da je signifikantnost opažanja tau neutrina u CNGS snopu 5.1σ . Takva signifikantnost se u fizici elementarnih čestica smatra *otkrićem* fizikalnog fenomena. Dodatno, ovo opažanje ograničava vrijednost parametra $|\Delta m_{32}^2|$ na interval $[2.0, 5.0] \cdot 10^{-3} \text{ eV}^2$ uz pouzdanost 90%. OPERA je jedini eksperiment koji je izmjerio ovaj parametar u pojavnom kanalu oscilacija neutrina.

Pošto je detektor OPERA sposoban mjeriti i prepoznati CC raspršenja elektronskih neutrina, napravljena je i analiza pojave elektronskih neutrina u CNGS snopu. Zbog velike kontaminacije CNGS snopa izvornim elektronskim neutrinima, nije moguće sa sigurnošću opaziti pojavu elektronskih neutrina iz neutrinjskih oscilacija. Očekivani broj opaženih raspršenja elektronskih i antielektronskih neutrina uz pretpostavku da nema neutrinjskih oscilacija je $33.1 \pm 0.7(\text{stat}) \pm 3.1(\text{syst})$, a uz pretpostavku standardnih oscilacija je $34.3 \pm 0.5(\text{stat}) \pm 3.4(\text{syst})$. U eksperimentu OPERA opaženo je 35 raspršenja elektronskih neutrina. Time je postavljeno ograničenje na kut miješanja $\sin^2 \theta_{13} < 0.12$ uz pouzdanost 90% u $\nu_\mu \rightarrow \nu_e$ kanalu neutrinjskih oscilacija.

Analiza predstavljena u ovom radu postavlja dodatno ograničenje na parametar $|\Delta m_{32}^2| < 4.1 \cdot 10^{-3} \text{ eV}^2$ uz pouzdanost 90%. To ograničenje je primarno uvjetovano $\nu_\mu \rightarrow \nu_\mu$ kanalom neutrinjskih oscilacija.

Za potrebe ovoga rada napravljena je posebna Monte Carlo simulacija eksperimenta OPERA. Međudjelovanja neutrina simulirana su računalnim programom *Genie 2.8.6*. Korištena je postojeća definicija geometrije detektora i objekata koji ga okružuju, napravljena pomoću programskog paketa *ROOT*.

⁶Događaji koji su klasificirani kao međudjelovanja tau neutrina a zapravo to nisu.

Postojeće programsko okruženje *OpRelease* za proizvodnju simuliranih događaja u eksperimentu OPERA poboljšano je kako bi se mogla koristiti simulirana raspršenja generirana programom *Genie*. Između ostaloga, za to je bio potreban ponovni izračun stopa međudjelovanja neutrina u svim materijalima detektora i njegovog okruženja, za sve izvorne i pojavne okuse neutrina. Taj izračun bio je potreban za određivanje prostorne raspodjele vjerojatnosti simuliranih međudjelovanja neutrina. Propagacija čestica kroz materiju simulirana je programskim paketoim *Geant3*. Odzivi elektroničkih senzora u detektoru simulirani su pomoću standardnih programa kolaboracije OPERA. Za rekonstrukciju neutrinskih događaja iz simuliranih odziva elektroničkih detektora koriste se isti algoritmi kao i za rekonstrukciju izmjerenih odziva, što omogućava neposrednu usporedbu simuliranih događaja s izmjerenim događajima. Napravljen je i algoritam koji svakom simuliranom događaju pridjeljuje težinu povezanu s ukupnim očekivanim brojem međudjelovanja te vrste, na način da je ukupna težina svih simuliranih međudjelovanja jednaka ukupnom očekivanom broju međudjelovanja CNGS neutrina u detektoru i okolnim materijalima.

Simulirano je ukupno oko 412 milijuna raspršenja neutrina u detektoru OPERA i okolnim materijalima, od kojih oko 2.5 milijuna okida⁷ OPERA detektor. Treba naglasiti da gotovo sva raspršenja neutrina u meti detektora okidaju detektor. Velika razlika između broja okinutih događaja i broja simuliranih raspršenja nastaje zbog toga što se simuliraju raspršenja i u stijeni koja okružuje detektor, a produkti tih međudjelovanja rijetko prolaze kroz senzore OPERA-e. Ukupna težina okinutih događaja, to jest očekivanih događaja registriranih na eksperimentu OPERA, uz pretpostavku da nema oscilacija neutrina je 96051, a uz pretpostavku standardnih oscilacija je 95056. Ukupan izmjereni broj događaja je 93458, što se lijepo slaže s predviđenim brojem događaja, s obzirom da je pogreška na tok CNGS neutrina (10 - 20)%. Taj skup simuliranih događaja korišten je za analizu predstavljenu u ovome radu i djelomično u analizama pojava oscilacijskih kanala $\nu_\mu \rightarrow \nu_\tau$ i $\nu_\mu \rightarrow \nu_e$ unutar kolaboracije OPERA.

Da bi se smanjio utjecaj nepouzdanosti toka CNGS neutrina, u analizi je korišten omjer opaženog broja NC i CC događaja. NC međudjelovanja ne ovise o okusu neutrina, što ih čini invarijantnima na neutrinske oscilacije. Kako omjer broja događaja ne slijedi

⁷To znači da je međudjelovanje neutrina opaženo kao događaj u detektoru.

ni Poissonovu ni Gaussovu distribuciju vjerojatnosti koja se najčešće koristi u literaturi, konstruiran je poseban statistički model koji pravilno opisuje statistiku analize temeljene na mjerenju omjera broja događaja. Za analizu su se koristili samo događaji koji su rekonstruirani u meti detektora OPERA.

Ti događaji su klasificirani u dvije kategorije: NC-slični i CC-slični. CC slični događaji su oni koji sadržavaju dobro rekonstruiran trag miona⁸, dok su NC slični događaji oni kod kojih niti jedan rekonstruirani trag čestice nije klasificiran kao trag miona.

Simulirani događaji su identičnim načinom klasificirani na CC-slične i NC-slične. Efekt neutrinjskih oscilacija uključuje se u simulaciju množenjem težine svakog pojedinog događaja s odgovarajućom vjerojatnošću neutrinjskih oscilacija. Tom klasifikacijom dobiven je vrlo čisti uzorak CC događaja. Uzorak NC događaja je bio manje čist zbog toga što sadrži većinu događaja nastalih u pojavnim kanalima, te CC događaje koji nemaju rekonstruiran trag miona.

U NC događajima nije moguće mjeriti energiju dolaznog neutrina zbog toga što neutrino u konačnom stanju odnosi nepoznatu količinu energije⁹. Kao zamjena za energiju neutrina uzeta je ukupna energija deponirana u meti detektora E_{tt} , pošto je ta veličina dobro definirana i za NC i za CC međudjelovanja.

Ograničenje na parametar oscilacija Δm_{32}^2 dobiveno je uspoređivanjem NC/CC omjera kao funkcije E_{tt} dobivenog stvarnim i simuliranim podacima. Simulirani podaci bili su varirani s obzirom na Δm_{32}^2 , te su isključene one vrijednosti tog parametra za koje p -vrijednost za slaganje podataka i simulacije manja od 10%. Time je dobivena gornja granica na vrijednost parametra $|\Delta m_{32}^2| < 4.1 \cdot 10^{-3} \text{eV}^2$.

Ključne riječi: neutrino, oscilacije, OPERA, CNGS, pojava, nestanak, LNGS, opservacija, duga osnovica

⁸Nastalog u CC raspršenju mionskog neutrina.

⁹Za razliku od CC interakcija gdje u konačnom stanju nema neutrina.

Contents

1	Introduction	1
2	Overview of neutrino physics	4
2.1	Interaction of neutrinos with matter	4
2.1.1	Weak interactions	4
2.1.2	Interactions of neutrinos with electrons	7
2.1.3	Interactions of neutrinos with nuclei	8
2.2	Neutrino oscillations	10
2.2.1	The mechanism of neutrino oscillations	10
2.2.2	Parametrization of the 3-generation mixing matrix	16
2.2.3	CP violation and neutrino mass hierarchy	21
2.2.4	Neutrino oscillations in matter	24
2.2.5	Neglecting the solar mass splitting	24
2.3	Neutrino sources	26
2.3.1	Natural sources	26
2.3.2	Artificial sources	31
2.4	Current experimental values of neutrino oscillation parameters	35
2.4.1	Measurement of Δm_{21}^2 and $\sin^2 \theta_{12}$	37
2.4.2	Measurements of Δm_{32}^2 and $\sin^2 \theta_{13}$	37
2.4.3	Measurements of Δm_{32}^2 and $\sin^2 \theta_{23}$	41
3	The OPERA experiment	44
3.1	CNGS beam	44
3.2	OPERA baseline	45
3.3	The OPERA detector	48
3.3.1	Emulsion cloud chamber - ECC	48
3.3.2	OPERA apparatus	51
3.3.3	Event reconstruction	54
3.4	Physics results	58
3.4.1	Discovery of $\nu_\mu \rightarrow \nu_\tau$ appearance	58
3.4.2	Constraints on neutrino oscillation parameters	60
4	Monte Carlo simulation of the OPERA experiment	62
4.1	Interaction rates	62
4.2	Simulating the effects of neutrino oscillations	65
4.3	OPERA detector geometry	66
4.3.1	Implementation in <i>ROOT</i>	66
4.3.2	Classification of materials	68
4.4	OPERA MC chain	69

4.4.1	Beamfiles	70
4.4.2	OpSim	72
4.4.3	OpDigit	74
4.4.4	OpRec	79
4.4.5	OpEmuRec	79
4.4.6	Event reweighting	81
4.5	Dedicated Monte Carlo production	83
5	Analysis	87
5.1	Statistical formalism	87
5.1.1	Test statistic and the p -value	88
5.1.2	Likelihood function	88
5.2	Construction of the likelihood function	89
5.2.1	Statistics of a counting histogram	90
5.2.2	Statistics of a ratio of two Poisson random variables	91
5.2.3	NC-like and CC-like event selection	93
5.2.4	Neutrino energy proxy variable	97
5.2.5	Construction of likelihood function	97
5.3	Construction of test statistics	98
5.3.1	Construction of test statistic distributions and p -values	100
5.4	Measurement of $ \Delta m_{32}^2 $	102
5.4.1	Effect of the beam uncertainty on the measurement	107
6	Conclusions	110
	Bibliography	112
	Appendix A OPERA tau candidate selection cuts	119
	Appendix B Confidence intervals for the binomial distribution	122
	Appendix C Photograph of OPERA using OPERA nuclear emulsion	124
	Curriculum vitae	126

Chapter 1

Introduction

The neutrino was first proposed by Wolfgang Pauli in the late 1930s as a last-ditch resort to save the energy conservation in the nuclear beta decay processes. He proposed the existence of a light neutral particle which carries away the apparently missing energy. The energy conservation was saved with his proposal, but the price to pay was an introduction of a new mysterious undetectable particle to the theory. The undetectable particle was since detected, its properties systematically probed over the years by various experiments, but its mystery remains.

The masses of neutrinos are still unknown. Neutrino oscillation theory, which predicts that neutrinos may be detected in a different flavour than they were produced in, requires that neutrinos have mass. However, this mass can not be measured by observing neutrino oscillation phenomena, since they depend on neutrino mass differences rather than absolute masses.

The other part of the mystery is that we still do not know whether neutrino is its own antiparticle. Of all elementary fermions present in the Standard Model of the modern particle physics, only neutrinos are candidates to have this property since they have no charges.

The only known way neutrinos can interact with rest of the matter is via weak interactions, which are in turn the only force present in the Standard Model which violates parity and the CP symmetry¹. CP symmetry violation implies that particles behave differently

¹Possible parity and CP violations induced by other forces are a matter of physics beyond the Standard Model. None have been observed as of yet.

than antiparticles², which has far reaching consequences in our understanding of the origin of the universe. It is the most important ingredient in the answer to the question why our universe is apparently made completely out of matter and not antimatter. The CP symmetry breaking has been experimentally observed in weak interactions of quarks, but is yet to be observed or disproved in neutrino interactions, adding to their mystery.

This work is mainly concerned with the experimental probing of neutrino oscillation phenomena. It adds a bit of an experimental knowledge to our understanding of the nature of neutrino by making an independent constraint on one of the neutrino oscillation parameters.

The structure of the thesis

After this introduction, the thesis continues with Chapter 2, which provides an overview of neutrino physics relevant for this work. It starts with a brief overview of interactions of neutrinos with matter. Following next is a somewhat detailed description of neutrino oscillation theory with emphasis on standard three-generation mixing, which is important for this thesis because it defines the theoretical parameters which are later experimentally determined. The second part of the chapter then describes modern landscape of neutrino sources and neutrino oscillation experiments which provide currently known experimental values of oscillation parameters.

The OPERA experiment and its physics output are described in Chapter 3. It begins with the description of CNGS neutrino beam, followed by a description of the OPERA detector and the way neutrino interaction events are reconstructed. The chapter ends with description of physics results obtained by OPERA experiment so far, including the constraints implied on neutrino oscillation parameters.

Chapter 4 deals with the Monte Carlo simulation of the OPERA experiment. First, a formal calculation of expected number of neutrino interactions in the OPERA detector is presented. Software framework used to produce the simulated events is then described in somewhat detailed manner, highlighting the author's contribution to the OPERA Monte Carlo efforts. Finally, a dedicated MC production created for the purposes of this work

²On an antimatter world, an antimatter scientist using their antimatter apparatus to measure an antineutrino interaction rate on antimatter would obtain different results than scientists on our world get when they measure interaction rates of neutrinos on ordinary matter.

is described. This production is used in the next chapter to obtain the constraint on neutrino oscillation parameters.

The Chapter 5 describes OPERA data analysis performed in this work and the physical results obtained by it. It starts with the description of statistical methods used to build the statistical model which connects the observed data and neutrino oscillation theory. This statistical model is then used to obtain the upper limit on the neutrino oscillation parameter $|\Delta m_{32}^2|$.

This thesis concludes in the Chapter 6.

Chapter 2

Overview of neutrino physics

2.1 Interaction of neutrinos with matter

This section contains a brief overview of neutrino interactions with matter. A detailed treatise on the subject from the theoretical point of view may be found in [17], and from the experimental point of view in [18].

2.1.1 Weak interactions

In the Standard Model of particle physics, neutrinos interact with the rest of the universe only via weak interactions. Weak interactions are a consequence of coupling of fermion fields (quarks and leptons) to massive W^\pm and Z boson fields. As their name suggests, these interactions are weak compared to electromagnetic and strong force interactions, which is a direct consequence of the large mass of mediating boson fields¹.

Charged current interactions

Charged current (CC) interactions are mediated by the charged² massive vector fields W^\pm . Their coupling to fermion fields are represented by Feynman diagrams shown in the Figure 2.1.

¹Actually, if W^\pm and Z were massless, weak interactions would be slightly stronger than electromagnetic ones

²Hence the name.



Figure 2.1: Couplings of W^+ and W^- bosons to fermions

Fermions f_u and f_d are *upper* and *lower* fermions, corresponding to CKM rotated quark generations in the quark sector, and lepton flavours in the lepton sector.

More precisely, they are defined in the lepton sector as:

$$\begin{pmatrix} f_u \\ f_d \end{pmatrix} = \begin{pmatrix} \nu_e \\ e^- \end{pmatrix} \text{ or } \begin{pmatrix} \nu_\mu \\ \mu^- \end{pmatrix} \text{ or } \begin{pmatrix} \nu_\tau \\ \tau^- \end{pmatrix}, \quad (2.1)$$

and in the quark sector:

$$\begin{pmatrix} f_u \\ f_d \end{pmatrix} = \begin{pmatrix} u \\ d' \end{pmatrix} \text{ or } \begin{pmatrix} c \\ s' \end{pmatrix} \text{ or } \begin{pmatrix} t \\ b' \end{pmatrix}, \quad (2.2)$$

where d' , s' and b' are lower quark states rotated by the CKM³ quark mixing matrix:

$$\begin{pmatrix} d' \\ s' \\ c' \end{pmatrix} = U_{\text{CKM}} \begin{pmatrix} d \\ s \\ c \end{pmatrix}. \quad (2.3)$$

The vertex factor for W^\pm coupling is given by

$$-i \frac{g}{2\sqrt{2}} \gamma_\mu (1 - \gamma_5), \quad (2.4)$$

where g is weak coupling constant connected with the electric charge e through the Weinberg angle θ_W :

$$g = \frac{e}{\sin^2 \theta_W}. \quad (2.5)$$

³Cabibo-Kobayashi-Maksawa

The W^\pm propagator is given by:

$$-i \frac{g_{\mu\nu} - q_\mu q_\nu / M_W^2}{q^2 - M_W^2}, \quad (2.6)$$

where q is boson's 4-momentum and M_W is it's mass.

Since all neutrino CC interactions inevitably produce charged leptons there is an inherent energy threshold in most of CC processes, because there must be enough energy in the center-of-mass frame to compensate for the mass of the charged lepton plus any other products of the interaction⁴. As a rule of thumb, the energy of a neutrino incident on a stationary target should be higher than the mass of charged lepton it produces.

CC interactions have some remarkable properties not present in other elementary interactions:

- They are the only known interactions which change the flavour of incoming elementary particles.
- They maximally violate the parity symmetry.
- They are the only known interactions which violate the CP symmetry.

Neutral current interactions

Neutral current interactions are mediated by the neutral massive Z^0 boson. The basic Feynman vertex is shown in Figure 2.2.

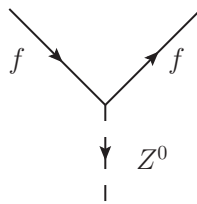


Figure 2.2: Coupling of Z^0 boson to fermions

The vertex factor is given by:

$$-i \frac{g}{2 \cos \theta_W} \frac{1}{2} \gamma^\mu \left(c_V^f - c_A^f \gamma^5 \right), \quad (2.7)$$

⁴Notable exceptions are neutrino captures on beta radioactive nuclei, e.g. inverse beta decay of tritium $\nu_e + {}^3_1\text{H} \rightarrow e^- + {}^3_2\text{He}$. This reaction has no energy threshold since tritium has enough energy by itself to decay to helium-3, electron and antineutrino.

where c_V^f and c_A^f are vector and axial coupling constants which depend on the fermion species and their charge:

$$c_V = T^3 - 2Q \sin^2 \theta_W \quad (2.8a)$$

$$c_A = T^3, \quad (2.8b)$$

where T^3 is an eigenvalue of the third component of the weak isospin (+1/2 for upper fermions and -1/2 for lower fermions), and Q is an electric charge of the fermion f .

The Z propagator is given by the formula similar to the one for the W^\pm field:

$$-i \frac{g_{\mu\nu} - q_\mu q_\nu / M_Z^2}{q^2 - M_Z^2}. \quad (2.9)$$

2.1.2 Interactions of neutrinos with electrons

The cleanest processes in which neutrinos interact with matter are interactions between neutrinos and electrons, since both of them are elementary particles and the relevant interaction cross-sections can be calculated directly from the electroweak theory. The simplest example would be scattering of muon neutrinos on orbital electrons, i.e.:

$$\nu_\mu + e^- \rightarrow \nu_e + \mu^- \quad (\text{CC}) \quad (2.10a)$$

$$\nu_\mu + e^- \rightarrow \nu_\mu + e^- \quad (\text{NC}), \quad (2.10b)$$

where CC reaction proceeds via virtual W boson coupling and NC reaction via virtual Z boson exchange. The interaction of ν_e with orbital electrons is slightly more complicated because CC and NC processes in that case produce the same reaction, so there is interference between them.

Assuming the center-of-mass energy is high enough that all particle masses can be neglected and low enough that it is well below W and Z masses, one obtains the following

cross sections in the tree-level Feynman approximation:

$$\sigma_{\text{CC}} = \frac{G_F^2 2m_e E_\nu}{\pi} \quad (2.11a)$$

$$\sigma_{\text{NC}} = \frac{G_F^2 2m_e E_\nu}{4\pi} \left((1 - 2\sin^2 \theta_W)^2 + \frac{4}{3} \sin^4 \theta_W \right), \quad (2.11b)$$

where

$$G_F = \frac{g^2}{4\sqrt{2}M_W^2} \approx 1.17 \cdot 10^{-5} \text{GeV}^{-2} \quad (2.12)$$

is the Fermi constant. The cross section in this energy region rises linearly with neutrino energy, which is a general feature of processes in which neutrinos interact with point-like particles.

Also, note that the cross section has linear dependence on m_e , i.e. the target mass. This is why, in the high energy region $E_\nu > \sim 1 \text{ GeV}$, neutrino scattering cross section on nuclei is a few orders of magnitude larger than the one for scattering on electrons.

2.1.3 Interactions of neutrinos with nuclei

The theoretical calculation of neutrino cross sections on nuclei are significantly more difficult to perform, since nuclei are composite structures consisting of multiple nucleons, which are themselves composed of quarks and gluons. Depending on their energy, neutrinos may interact with nucleus as a whole, a nucleon as a whole, or with quarks as point particles.

As a useful rule of thumb, one may use the Planck wavelength of neutrinos to estimate which of these interaction types will be dominant for a given neutrino energy. The rule says that the spatial scale on which neutrino interacts is comparable to its wavelength. Nuclei have a diameter of an order of 10 fm and nucleons have a diameter of roughly 1 fm. The Planck wavelength is given by the formula

$$\lambda_\nu = \frac{2\pi\hbar c}{E_\nu} \approx \frac{1}{E_\nu} \cdot 1237 \text{ MeV fm}. \quad (2.13)$$

It follows that neutrinos of laboratory frame energies of the order 100 MeV or less will interact with a nucleus as a whole, those with energies around 1 GeV will interact with

nucleons and those with energies larger than 20 GeV will interact with quarks as point-like particles in deep-inelastic scatterings.

Interactions in the low energy region (1 - 100) MeV

In this energy region, CC interactions of muon and tau neutrinos are not possible due to charged lepton production energy threshold. This leaves electron flavoured neutrinos as the only ones interacting via CC, mainly through various inverse beta decay reactions.

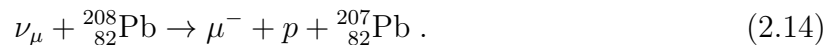
In the neutrino case, inverse beta decay transforms a bound neutron into a proton, increasing the atomic number of a nucleus. An antineutrino interaction transforms a bound proton into neutron, reducing the atomic number of a nucleus. The former of these reactions are important for the detection of Solar neutrinos, while the latter is important for detection of reactor neutrinos.

NC reactions in this energy region produce only a small nuclear rebound which is very difficult to detect.

Interactions in the intermediate energy region (0.1 - 20) GeV

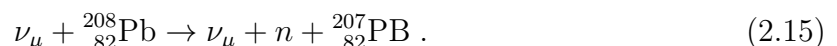
This energy region is dominated by neutrino interactions with individual nuclei. Quasielastic (QE) and resonant (RES) interactions are dominant at the low range of the energy spectrum, while the deep inelastic (DIS) reactions are dominating the high energy end. At the intermediate energies of (1 - 10) GeV, all three reaction types are possible.

The quasi-elastic (QE) CC interactions eject a nucleon from a nucleus and transform it from a proton to a neutron or vice versa. An example of such reaction in the OPERA experiment would be



Note that incoming neutrinos interact only with neutrons via QE interactions, while antineutrinos interact only with protons via QE interactions.

The elastic NC scattering is similar to QE, apart from the fact that the ejected nucleon is not transformed. An example would be:



The resonant CC interaction (RES) is interaction of an neutrino with a nucleon, which excites a nucleon to a resonant state. The resonant state quickly decays through strong interactions, producing a nucleon and a pion. On a nucleon level, this reaction proceeds as:

$$\nu_{\mu} + N \rightarrow \mu^{-} + N^{*} \rightarrow \mu^{-} + \pi + N', \quad (2.16)$$

where N is either proton or a neutron, N^{*} is an excited baryon state, and N' is a proton if N is a neutron and vice-versa.

In deep-inelastic interactions (DIS), neutrinos interact directly with quarks which constitute a nucleon, and can proceed via NC and CC interactions. The quark is effectively ejected from a nucleon, producing a hadronic shower and destroying the original nucleon. Energy dependence of DIS interaction cross-sections scales as the one for point-like target, i.e. linearly with the neutrino energy.

Neutrinos in the OPERA experiment fall roughly in this energy region.

The theoretical prediction and available experimental data for CC interaction cross sections as a function of energy are shown in Figure 2.3.

Interactions in the high energy region (20 - 500) GeV

Neutrino interactions in this energy region are dominated by the pure deep inelastic scattering, with interaction cross-sections scaling linearly with E_{ν} . This energy region is relevant for the high energy part of the atmospheric neutrino flux.

2.2 Neutrino oscillations

2.2.1 The mechanism of neutrino oscillations

The main assumptions of the neutrino oscillation theory are that *(i)* neutrinos are massive particles and that *(ii)* flavour fields which enter into the leptonic charged-currents do not have definite mass.

Instead, flavour neutrino fields are a mixture of mass neutrino fields connected by a unitary mixing matrix:

$$\nu_{\alpha} = U_{\alpha i} \nu_i, \quad (2.17)$$

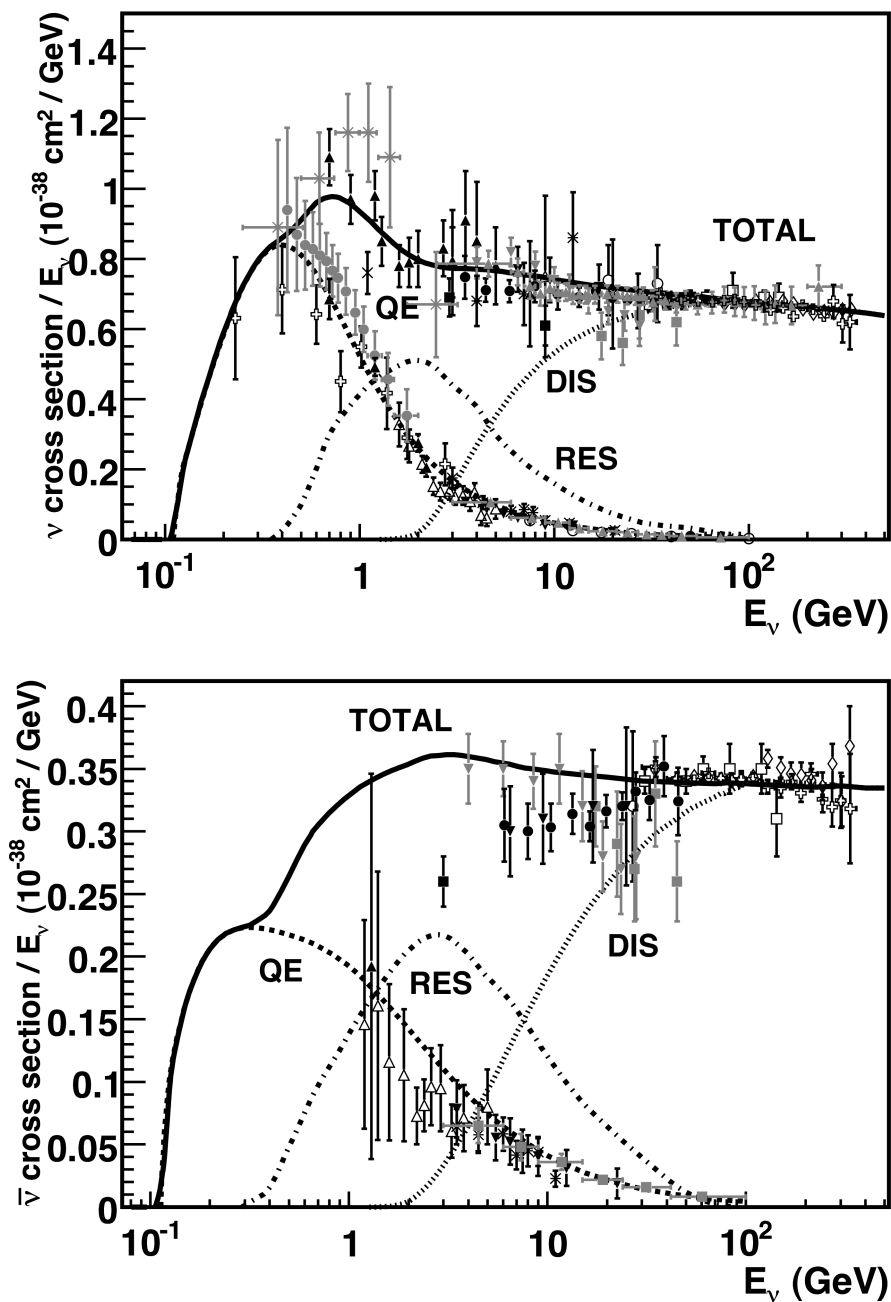


Figure 2.3: A cross section per nucleon for CC interactions of muon neutrinos (upper plot) and antineutrinos (lower plot) on an isoscalar target as a function of neutrino energy in the laboratory frame. An isoscalar target is a target which is composed of the same number of protons and neutrons. Contributions from QE, RES and DIS interaction are shown separately. The available experimental data is superimposed to the theoretical predictions. For the detailed description of neutrino experiments which measured the data, see Ref. [17]. Figure taken from [17].

where the index $\alpha = 1, \dots, n$ denotes flavour neutrino fields, and the index $i = 1, \dots, n$ denotes mass neutrino fields.

Flavour neutrino states are created by charged current (CC) weak interactions of the sort:

$$P_I \rightarrow P_F + l_\alpha^+ + \nu_\alpha \quad (2.18a)$$

$$l_\alpha^- + P_I \rightarrow P_F + \nu_\alpha \quad (2.18b)$$

, where P_I and P_F are initial and final particle states independent of flavour α , while l_α^+ and ν_α are a charged lepton and a neutrino created in CC process. The quantum state of the outgoing neutrino can be written in general as:

$$|\nu_\alpha^P\rangle = A_{\alpha k}^P |\nu_k\rangle, \quad (2.19)$$

where P is a label of the process in which neutrino is created, index k is a label of mass neutrino states, and $A_{\alpha k}^P$ is a normalized amplitude of production of a mass state k in the process P .

The mixing matrix U can be factorized out of the production amplitude, yielding:

$$A_{\alpha k}^P = M_{\alpha k}^P U_{\alpha k}^* \quad (\text{neutrino}), \quad (2.20a)$$

$$A_{\alpha k}^P = M_{\alpha k}^P U_{\alpha k} \quad (\text{antineutrino}), \quad (2.20b)$$

where $M_{\alpha k}^P$ are interaction matrix elements specific to the creation process, with the normalization such that the flavour states remain orthogonal. The reason that $U_{\alpha k}^*$ enters equation (2.20a) while $U_{\alpha k}$ enters (2.20b) is that neutrinos are, by definition, produced together with a charged antilepton in a process (2.18a), which is described by charged current Lagrangian component

$$2 \sum_{\alpha=1}^n \bar{\nu}_{\alpha L} \gamma^\mu l_{\alpha L} = 2 \sum_{\alpha=1}^n \sum_{k=1}^n U^*_{\alpha k} \bar{\nu}_{k L} \gamma^\mu l_{\alpha L}, \quad (2.21)$$

while the antineutrino production is described by its complex conjugate (for more details see chapters 7.1 and 7.2 of Ref. [19]).

Similarly, neutrino flavour is measured in the detector through a scattering process such as:

$$\nu_\alpha + D_I \rightarrow l^- + D_F , \quad (2.22)$$

where D_I is a target particle in the detector and D_F are interaction products other than the resulting charged lepton. As in the production case, detected neutrino flavour state can be written as

$$|\nu_\alpha^D\rangle = A_{\alpha k}^D |\nu_k\rangle , \quad (2.23)$$

where D is a label of the detection process and $A_{\alpha k}^D$ is the production amplitude for the mass state $|\nu_k\rangle$. Again, the detection amplitude can be factorized as

$$A_{\alpha k}^D = M_{\alpha k}^D U_{\alpha k}^* \quad (\text{neutrino}) , \quad (2.24a)$$

$$A_{\alpha k}^D = M_{\alpha k}^D U_{\alpha k} \quad (\text{antineutrino}) . \quad (2.24b)$$

To keep track of both neutrino and antineutrino cases, $|\tilde{\nu}\rangle$ shall denote either neutrino or antineutrino, and the mixing matrix shall be written as

$$\mathcal{U}_{\alpha k} \equiv \begin{cases} U_{\alpha k} & \text{for neutrino} , \\ U_{\alpha k}^* & \text{for antineutrino} . \end{cases} \quad (2.25)$$

Putting it all together, production and detection flavour states can be written as:

$$|\tilde{\nu}_\alpha^P\rangle = M_{\alpha k}^P \mathcal{U}_{\alpha k}^* |\tilde{\nu}_k\rangle , \quad (2.26a)$$

$$|\tilde{\nu}_\alpha^D\rangle = M_{\alpha k}^D \mathcal{U}_{\alpha k} |\tilde{\nu}_k\rangle . \quad (2.26b)$$

Suppose a neutrino state of a flavour α has been created by a process P at the origin of a relativistic 4-dimensional coordinate system⁵. Suppose this neutrino is then detected at a point $x = (T, \vec{L})$, with \vec{L} pointing in the direction of neutrino's 3-momentum \vec{p} .

The probability that the neutrino is detected in a flavour state β is then:

$$P_{\alpha \rightarrow \beta} = |\langle \tilde{\nu}_\beta^D | \tilde{\nu}_\alpha^P; x \rangle|^2 , \quad (2.27)$$

⁵Space coordinates $\vec{x} = \vec{0}$ and time $t = 0$

where $|\tilde{\nu}_\alpha^P; x\rangle$ is the initial state (2.26a), translated from the origin of the coordinate system to the point (T, \vec{L}) . This state is obtained by applying the 4-dimensional translation operator to the initial state:

$$|\tilde{\nu}_\alpha^P; x\rangle = e^{-i\mathbf{p}^\mu x_\mu} |\tilde{\nu}_\alpha^P\rangle , \quad (2.28)$$

where $\mathbf{p} = (\mathbf{E}, \vec{\mathbf{p}})$ is a quantum operator of a 4-dimensional momentum of a free particle. By substitution, one obtains

$$|\tilde{\nu}_\alpha^P; x\rangle = e^{-i(\mathbf{E}T - |\vec{\mathbf{p}}|L)} |\tilde{\nu}_\alpha^P\rangle = e^{-i(\mathbf{E}T - |\vec{\mathbf{p}}|L)} M_{\alpha k}^P \mathcal{U}_{\alpha k}^* |\tilde{\nu}_k\rangle . \quad (2.29)$$

Since $|\tilde{\nu}_k\rangle$ is a free particle eigenstate and operators \mathbf{E} and $|\vec{\mathbf{p}}|$ commute, the following identity holds:

$$e^{-i(\mathbf{E}T - |\vec{\mathbf{p}}|L)} |\tilde{\nu}_k\rangle = e^{-i(E_k T - |\vec{p}_k|L)} |\tilde{\nu}_k\rangle , \quad (2.30)$$

where E_k and \vec{p}_k are energy and momentum of the k -th neutrino mass eigenstate. Since all detectable neutrinos are ultra-relativistic, it's safe to assume $T = L$, so the phase in the above equation can be rewritten as:

$$E_k T - |\vec{p}_k|L = (E_k - |\vec{p}_k|)L = \frac{E_k^2 - |\vec{p}_k|^2}{E_k + |\vec{p}_k|} L = \frac{m_k^2}{E_k + |\vec{p}_k|} L . \quad (2.31)$$

Since neutrinos are ultra-relativistic, one may approximate

$$E_k + |\vec{p}_k| \approx 2E , \quad (2.32)$$

where E is the average energy of mass states. Putting it all together, the translated state can be written as:

$$|\tilde{\nu}_\alpha^P; x\rangle = M_{\alpha k}^P \mathcal{U}_{\alpha k}^* e^{-i\frac{m_k^2}{2E}L} |\tilde{\nu}_k\rangle . \quad (2.33)$$

Substituting the equation (2.33) into (2.27), using the equation (2.26b) to expand the detected neutrino state, and using the fact that mass states are orthogonal, one obtains

the neutrino oscillation formula

$$P_{\alpha \rightarrow \beta} = \left| (M_{\beta k}^D)^* M_{\alpha k}^P \mathcal{U}_{\beta k} \mathcal{U}_{\alpha k}^* e^{-i \frac{m_k^2}{2E} L} \right|^2. \quad (2.34)$$

The normalized production and detection matrix elements $M_{\alpha k}^P$ and $M_{\beta k}^D$ depend on the neutrino masses m_k through the kinematic effects of production and detection processes. It is reasonable to assume that the experiments are not at all sensitive to the difference in kinematic effects between light neutrinos, so one can approximate these matrix elements as equal for all masses m_k :

$$M_{\alpha k}^P \approx M_{\alpha}^P, \quad (2.35a)$$

$$M_{\alpha k}^D \approx M_{\alpha}^D, \quad (2.35b)$$

where M_{α}^P and M_{α}^D are an average of matrix elements for all neutrino masses. Under this assumption, they can be factored out of the sum in equation (2.34):

$$P_{\alpha \rightarrow \beta} = |(M_{\beta}^D)^* M_{\alpha}^P|^2 \left| \mathcal{U}_{\beta k} \mathcal{U}_{\alpha k}^* e^{-i \frac{m_k^2}{2E} L} \right|^2, \quad (2.36)$$

and since they are normalized by construction, their absolute value must be unity, so the oscillation probability equation becomes:

$$P_{\alpha \rightarrow \beta} = \left| \mathcal{U}_{\beta k} \mathcal{U}_{\alpha k}^* e^{-i \frac{m_k^2}{2E} L} \right|^2. \quad (2.37)$$

It is important to note that even if approximations (2.35) are not applicable, it is effectively a correction on the mixing coefficients $\mathcal{U}_{\alpha k}$ and has no effect on the oscillation phase which contains the information on neutrino masses.

Using the definition (2.25), the oscillation probability can be written separately for neutrinos and antineutrinos:

$$P_{\alpha \rightarrow \beta} = \left| U_{\beta k} U_{\alpha k}^* e^{-i \frac{m_k^2}{2E} L} \right|^2, \quad (2.38a)$$

$$P_{\bar{\alpha} \rightarrow \bar{\beta}} = \left| U_{\beta k}^* U_{\alpha k} e^{-i \frac{m_k^2}{2E} L} \right|^2 = \left| U_{\beta k} U_{\alpha k}^* e^{+i \frac{m_k^2}{2E} L} \right|^2, \quad (2.38b)$$

which can be combined in a single equation as:

$$P_{\alpha \rightarrow \beta} = \left| U_{\beta k} U_{\alpha k}^* e^{\mp i \frac{m_k^2}{2E} L} \right|^2, \quad (2.39)$$

keeping in mind that the upper sign (-) corresponds to neutrinos and the lower (+) for antineutrinos. Expanding the equation (2.39), one obtains the standard oscillation formula

$$P_{\alpha \rightarrow \beta} = U_{\alpha i}^* U_{\alpha j} U_{\beta i} U_{\beta j}^* e^{\mp i (m_i^2 - m_j^2) \frac{L}{2E}}, \quad (2.40)$$

where the upper sign is valid for neutrinos and the lower one for antineutrinos.

By defining the shorthand notations

$$\Delta m_{ij}^2 \equiv m_i^2 - m_j^2, \quad (2.41a)$$

$$A_{ij}^{\alpha\beta} \equiv U_{\alpha i}^* U_{\alpha j} U_{\beta i} U_{\beta j}^*, \quad (2.41b)$$

$$\phi_{ij} \equiv \frac{\Delta m_{ij}^2 L}{2E}, \quad (2.41c)$$

and doing some algebra, equation (2.40) can be written in the commonly used form:

$$P_{\alpha \rightarrow \beta} = \delta_{\alpha\beta} - 4 \sum_{i>j} \operatorname{Re} \left(A_{ij}^{\alpha\beta} \right) \sin^2 \frac{\phi_{ij}}{2} \pm 2 \sum_{i>j} \operatorname{Im} \left(A_{ij}^{\alpha\beta} \right) \sin \phi_{ij}. \quad (2.42)$$

2.2.2 Parametrization of the 3-generation mixing matrix

General $n \times n$ unitary matrix

A general $n \times n$ complex matrix consists of n^2 complex numbers, i.e. $2n^2$ real parameters. It can be parametrized as:

$$U_{ij} = a_{ij} e^{i\phi_{ij}}, \quad (2.43)$$

where $i = 1, \dots, n$ and $j = 1, \dots, n$ are indices of rows and columns, respectively. $a_{ij} \in \mathbb{R}^+$ are positive moduli of complex numbers and $\phi_{ij} \in \langle -\pi, \pi \rangle$ are their phases.

The unitary condition⁶

$$UU^\dagger = \mathbb{1} \quad (2.44)$$

can be written as

$$a_{ij}a_{kj}e^{i(\phi_{ij}-\phi_{kj})} = \delta_{ik} . \quad (2.45)$$

These complex equations can be rewritten as a set of n^2 independent real equations:

$$\sum_{j=1}^n a_{ij}^2 = 1 \quad n \text{ equations}, \quad (2.46a)$$

$$a_{ij}a_{kj} \cos(\phi_{ij} - \phi_{kj}) = 0, \quad i \neq k \quad n(n-1)/2 \text{ equations}, \quad (2.46b)$$

$$a_{ij}a_{kj} \sin(\phi_{ij} - \phi_{kj}) = 0, \quad i \neq k \quad n(n-1)/2 \text{ equations}. \quad (2.46c)$$

Therefore, a general unitary matrix has $2n^2 - n^2 = n^2$ independent real parameters.

Sets of equations (2.46b) and (2.46c) contain both amplitudes and phases, reducing the number of independent phases by $n(n-1)/2$ and the number of amplitudes by $n(n-1)/2$. Equations (2.46a) further reduce the number of independent amplitudes by n .

Putting it all together, a general unitary matrix is composed of

- $n^2 - n(n-1)/2 - n = n(n-1)/2$ amplitudes
- $n^2 - n(n-1)/2 = n(n+1)/2$ phases

Additionally, equations (2.46a) impose the condition $|a_{ij}| \leq 1$, which allows to reparametrize the amplitudes as cosines of euler⁷ angles. The amplitudes can thus be written as:

$$a_{ij} = \cos \theta_{ij} , \quad (2.47)$$

where θ_{ij} is an euler angle. Since $a_{ij} \geq 0$, euler angles may be defined to be in the range $\theta_{ij} \in [0, \pi/2]$.

⁶Note that for finite square matrices, if $AB = \mathbb{1}$ then also $BA = \mathbb{1}$, so the additional condition $U^\dagger U = \mathbb{1}$ is superfluous

⁷An analogy to euler angles in the theory of spatial rotations - unitary matrices can be thought of as rotations in complex vector space

The shorthand notation

$$s_{ij} \equiv \sin \theta_{ij} , \quad (2.48a)$$

$$c_{ij} \equiv \cos \theta_{ij} \quad (2.48b)$$

shall be used throughout the text.

General $n \times n$ neutrino mixing matrix

When a unitary matrix is used to describe neutrino mixing as in equation (2.17), not all of the $n(n+1)/2$ unitary phases have a physical meaning, i.e. are not observable in any physical process described by the extended SM Lagrangian⁸. The reason behind this is that a number of phases in the mixing matrix can be cancelled out by re-phasing the lepton fields. There are two distinct cases, depending whether neutrinos are Dirac or Majorana fields⁹.

The mixing matrix U is defined as the mixing between flavour and mass neutrino fields (2.17), and it enters the Lagrangian only through the leptonic charged-current term

$$j_{W,L}^\mu = 2 \sum_{\alpha=1}^n \bar{\nu}_{\alpha L} \gamma^\mu l_{\alpha L} + \text{h.c.} = 2 \sum_{\alpha=1}^n \sum_{i=1}^n \bar{\nu}_{iL} \gamma^\mu U_{\alpha i}^* l_{\alpha L} + \text{h.c.} . \quad (2.49)$$

Suppose that charged lepton fields are re-phased with a transformation

$$l_\alpha \rightarrow e^{i\eta_\alpha} l_\alpha , \quad (2.50)$$

and neutrino fields with a transformation

$$\nu_i \rightarrow e^{i\xi_i} \nu_i . \quad (2.51)$$

Substituting the equations (2.50) and (2.51) into (2.49), one obtains:

$$j_{W,L}^\mu = 2 \sum_{\alpha=1}^n \sum_{i=1}^n \bar{\nu}_{iL} \gamma^\mu e^{-i\xi_i} U_{\alpha i}^* e^{i\eta_\alpha} l_{\alpha L} . \quad (2.52)$$

⁸Extended SM Lagrangian here means the SM Lagrangian with addition of neutrino masses

⁹As of yet, no experiment has discriminated between these two options, so one needs to keep both in the theory

Apart from this term, the rest of Lagrangian is invariant to global changes of phase for each of the Dirac lepton fields. Charged leptons are known to be Dirac particles, so the phases η_α may be arbitrarily chosen to cancel out some of the phases in the mixing matrix. Similarly, if neutrinos are Dirac fields, phases ξ_i may be chosen arbitrary as well.

If neutrinos are Majorana fields, the situation is different. The Majorana mass term

$$\mathcal{L}_M^{\text{Majorana}} = -\frac{1}{2}m \overline{\nu_L^C} \nu_L \quad (2.53)$$

is not invariant to global phase shift of the fields because of the charge conjugation operator. The effect of such transformation on the Majorana mass term is

$$\nu_i \rightarrow e^{i\xi_i} \nu_i \implies \mathcal{L}_M^{\text{Majorana}} \rightarrow e^{i2\xi_i} \mathcal{L}_M^{\text{Majorana}} . \quad (2.54)$$

This means that Majorana particles have an internal phase which is a physically observable quantity. Therefore, they can not be arbitrarily re-phased, which in this formalism means that $\xi_i = 0$. So, in Majorana case only charged lepton phases η_α can be arbitrarily chosen to cancel out additional n phases in the mixing matrix U .

In the Dirac case, both ξ_i and η_α can be arbitrarily chosen. The number of phases which can be cancelled in the mixing matrix is $2n - 1$, and not $2n$ as one might expect. The reason is that these phases enter the equation (2.52) as $e^{i(\eta_\alpha - \xi_i)}$, and there are only $2n - 1$ independent combinations $\eta_\alpha - \xi_i$.

This means that the mixing matrix in the case of Majorana neutrinos has $n - 1$ more phases than in the Dirac case. These additional phases are called Majorana mixing phases.

The total number of physical parameters in the $n \times n$ neutrino mixing matrix U is shown in the Table 2.1.

Table 2.1: The number of physical parameters in the $n \times n$ neutrino mixing matrix

	Euler angles	Phases
Majorana	$n(n - 1)/2$	$n(n - 1)/2$
Dirac	$n(n - 1)/2$	$(n - 1)(n - 2)/2$

The three generation mixing matrix

From the measurement of the width of Z boson, it is known that there are three active¹⁰ light¹¹ neutrino generations [20]. The mixing of three generations of neutrinos is described by a 3×3 mixing matrix. It is usually parametrized in analogy with the parametrization of 3-dimensional spatial rotations using euler angles, i.e as a product of three unitary matrices each keeping a different mass state invariant, with addition of a fourth matrix containing the Majorana phases.

The most widely used convention advocated by the PDG [21] and by the textbook [19] is:

$$U = U_{23}U_{13}U_{12}U_M , \quad (2.55)$$

where the factors are:

- $U_{23} = \begin{pmatrix} 1 & 0 & 0 \\ 0 & c_{23} & s_{23} \\ 0 & -s_{23} & c_{23} \end{pmatrix}$ - known as the *atmospheric* mixing matrix.
- $U_{13} = \begin{pmatrix} c_{13} & 0 & s_{13}e^{-i\delta_{\text{CP}}} \\ 0 & 1 & 0 \\ -s_{13}e^{i\delta_{\text{CP}}} & 0 & c_{13} \end{pmatrix}$ - known as the *reactor* mixing matrix.
- $U_{12} = \begin{pmatrix} c_{12} & s_{12} & 0 \\ -s_{12} & c_{12} & 0 \\ 0 & 0 & 1 \end{pmatrix}$ - known as the *solar* mixing matrix.
- $U_M = \begin{pmatrix} 1 & 0 & 0 \\ 0 & e^{i\alpha/2} & 0 \\ 0 & 0 & e^{i\beta/2} \end{pmatrix}$ - the additional two Majorana phases.

The Majorana phases do not enter the neutrino oscillation formulae because they drop out of the term $A_{ij}^{\alpha\beta}$ defined by the equation (2.41b). This can be seen by writing the mixing matrix as $U = V \cdot \text{diag}(1, e^{i\alpha/2}, e^{i\beta/2})$ and substituting into equation (2.41b), after which only the components of V will remain in the equation. Therefore, neutrino

¹⁰As in not sterile.

¹¹Having mass smaller than Z boson

oscillation experiments can not discriminate between Majorana and Dirac neutrinos, so the Majorana phases will be omitted in the rest of the text.

The CP violating phase δ_{CP} enters via U_{13} matrix because of the ordering of the terms in equation (2.55). If one would use another ordering, the CP violating phase would always enter through the second term.

The full mixing matrix is therefore:

$$U = \begin{pmatrix} 1 & 0 & 0 \\ 0 & c_{23} & s_{23} \\ 0 & -s_{23} & c_{23} \end{pmatrix} \begin{pmatrix} c_{13} & 0 & s_{13}e^{-i\delta_{\text{CP}}} \\ 0 & 1 & 0 \\ -s_{13}e^{i\delta_{\text{CP}}} & 0 & c_{13} \end{pmatrix} \begin{pmatrix} c_{12} & s_{12} & 0 \\ -s_{12} & c_{12} & 0 \\ 0 & 0 & 1 \end{pmatrix}. \quad (2.56)$$

Expanding the equation (2.56) one obtains:

$$U = \begin{pmatrix} c_{12}c_{13} & s_{12}c_{13} & s_{13}e^{-i\delta_{\text{CP}}} \\ -s_{12}c_{23} - c_{12}s_{23}s_{13}e^{i\delta_{\text{CP}}} & c_{12}c_{23} - s_{12}s_{23}s_{13}e^{i\delta_{\text{CP}}} & s_{23}c_{13} \\ s_{12}s_{23} - c_{12}c_{23}s_{13}e^{i\delta_{\text{CP}}} & -c_{12}s_{23} - s_{12}c_{23}s_{13}e^{i\delta_{\text{CP}}} & c_{23}c_{13} \end{pmatrix}. \quad (2.57)$$

2.2.3 CP violation and neutrino mass hierarchy

CPT invariance of neutrino oscillations in vacuum

It is interesting to look at properties of the oscillation probability equation (2.42) under CP and T transformations. The CP operator simply interchanges particles and antiparticles:

$$P_{\alpha \rightarrow \beta} \xrightarrow{\text{CP}} P_{\bar{\alpha} \rightarrow \bar{\beta}}, \quad (2.58)$$

which can be described¹² by applying complex conjugation on all of the $A_{ij}^{\alpha\beta}$ coefficients:

$$A_{ij}^{\alpha\beta} \xrightarrow{\text{CP}} \left(A_{ij}^{\alpha\beta} \right)^*. \quad (2.59)$$

Time reversal simply interchanges initial and detected neutrino flavours:

$$P_{\alpha \rightarrow \beta} \xrightarrow{\text{T}} P_{\beta \rightarrow \alpha}, \quad (2.60)$$

¹²According to the construction of the equation (2.42) one should flip the sign of the third term to go from particles to antiparticles and vice-versa, and conjugation of $A_{ij}^{\alpha\beta}$ does exactly that.

which has the effect of swapping α and β indices in $A_{ij}^{\alpha\beta}$. It is easy to see from the definition (2.41b) that

$$A_{ij}^{\beta\alpha} = \left(A_{ij}^{\alpha\beta} \right)^* , \quad (2.61)$$

so the effect of T transformation on these coefficients is, again, complex conjugation:

$$A_{ij}^{\alpha\beta} \xrightarrow{\text{T}} A_{ij}^{\beta\alpha} = \left(A_{ij}^{\alpha\beta} \right)^* . \quad (2.62)$$

The immediate result is that the oscillation formula is invariant under CPT transformations, as it should be since it is a fundamental symmetry of the underlying field theory. It should be noted that only the third term in the equation (2.42) may induce CP and T violation.

By applying the CPT transformation on the oscillation probability formula, one can obtain the connection between neutrino and antineutrino oscillation probabilities:

$$P_{\alpha \rightarrow \beta} = P_{\bar{\beta} \rightarrow \bar{\alpha}} . \quad (2.63)$$

The other interesting fact is that the probabilities for disappearance channels¹³ are CP invariant and are consequently the same for neutrinos and antineutrinos:

$$P_{\alpha \rightarrow \alpha} = P_{\bar{\alpha} \rightarrow \bar{\alpha}} . \quad (2.64)$$

This can also be seen by noting that the disappearance probability is manifestly invariant under T transformation

$$P_{\alpha \rightarrow \alpha} \xrightarrow{\text{T}} P_{\alpha \rightarrow \alpha} . \quad (2.65)$$

and therefore must be invariant under CP transformation as well.

Another way to see this is from equation (2.61), which implies that

$$A_{ij}^{\alpha\alpha} = \left(A_{ij}^{\alpha\alpha} \right)^* , \quad (2.66)$$

meaning all the coefficients are real, and therefore the third term on the right side of the

¹³Probabilities where initial and detected neutrino are of the same flavour

equation (2.42) vanishes.

Neutrino mass hierarchy

The neutrino oscillation probability equation (2.42) depends on differences of squares of physical neutrino masses, rather than the masses themselves. Additionally, apart from the CP violating term, the oscillation probability is invariant to absolute value of these differences since they enter the equation as $\sin^2 \frac{\Delta m_{ij}^2 L}{2E}$. Therefore, the ordering of neutrino masses cannot be deduced from vacuum neutrino oscillation experiments insensitive to CP violating effects. However, the relative sign between two independent Δm_{ij}^2 can be measured by such experiments, as described below.

Only two out of three mass differences are independent parameters since the definition (2.41a) trivially yields the following identity:

$$\Delta m_{21}^2 + \Delta m_{32}^2 = \Delta m_{31}^2 . \quad (2.67)$$

The choice of the two independent parameters is arbitrary, with Δm_{21}^2 and Δm_{32}^2 being commonly used as independent parameters in literature.

Suppose an experiment measures the absolute values of Δm_{21}^2 , Δm_{32}^2 and Δm_{31}^2 independently. It follows from the equation (2.67) that these absolute values are connected as:

$$|\Delta m_{31}^2| = \begin{cases} |\Delta m_{21}^2| + |\Delta m_{32}^2|, & \text{if } \text{sgn}(\Delta m_{21}^2) = \text{sgn}(\Delta m_{32}^2) \\ |\Delta m_{21}^2| - |\Delta m_{32}^2|, & \text{if } \text{sgn}(\Delta m_{21}^2) \neq \text{sgn}(\Delta m_{32}^2) \end{cases} , \quad (2.68)$$

from which it is easy to obtain the relative sign between Δm_{21}^2 and Δm_{32}^2 by comparing the measured absolute values. Additionally, if the sign of one of those two parameters is known¹⁴, one can determine the sign of the other, therefore solving the neutrino mass hierarchy problem.

¹⁴At the time of writing, the sign of Δm_{21}^2 is known to be positive, i.e. $m_2 > m_1$. The sign of Δm_{32}^2 is still unknown since no experiment is sensitive enough to all three mass differences

2.2.4 Neutrino oscillations in matter

When passing through matter, neutrinos feel an external potential through coherent forward scattering on electrons and nuclei. If all neutrino flavours would feel the same potential when passing through matter, i.e. their passage through matter would induce only flavour-invariant effects, neutrino oscillation theory in matter would be equivalent to the one in vacuum¹⁵. However, this is not the case because electron neutrinos interact with electrons differently than muon and tau neutrinos. The elastic scattering of electron neutrinos on electrons

$$\nu_e + e^- \rightarrow \nu_e + e^- \quad (2.69)$$

may proceed through both W and Z boson exchange, while the scattering of other flavours

$$\nu_x + e^- \rightarrow \nu_x + e^- , \quad (2.70)$$

where $x = \mu, \tau$ may proceed only through Z exchange. This induces an effective potential which is seen only by electron neutrinos, and depends on the concentration of electrons in the medium neutrino is travelling through.

A more detailed description of these effects may be found in [18, 21] and references therein.

2.2.5 Neglecting the solar mass splitting

The solar mass splitting Δm_{21}^2 has been measured by independent experiments, with the latest state-of-the-art value provided by KamLAND [1], with the current best fit value is $\Delta m_{21}^2 = (7.53 \pm 0.18) \cdot 10^{-5} \text{eV}$.

To estimate the contribution of the Δm_{21}^2 term to the total oscillation probability, one needs to evaluate the $i = 2; j = 1$ term in the first sum in the oscillation formula (2.42):

$$4\text{Re} \left(A_{21}^{\alpha\beta} \right) \sin^2 \frac{\Delta m_{21}^2 L}{2 E} . \quad (2.71)$$

To get an upper limit on the possible contribution by the solar mass splitting, one may set $A_{21}^{\alpha\beta} = 1$. The energies of incoming neutrinos in the OPERA experiment is roughly in

¹⁵Except for effects on the boundary between matter and vacuum.

the range 1 GeV to 40 GeV (see Figure 3.2), and the distance between CERN and LNGS is about 732 km. The contribution of this term as a function of energy is plotted in the Figure 2.4.

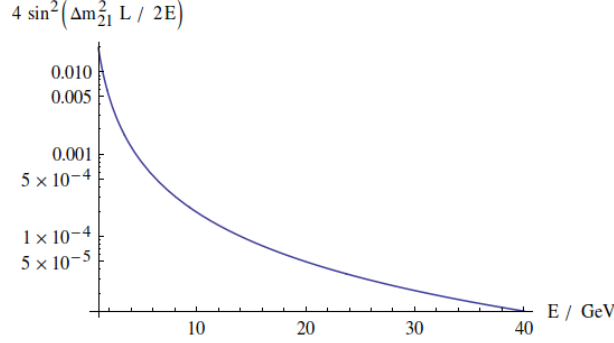


Figure 2.4: Value of the $\sin^2 \frac{\phi_{21}}{2}$ vs. neutrino energy E at the OPERA distance

Since the contribution of this factor is much less than 1% in the region of interest, the OPERA experiment is not sensitive to neutrino oscillations driven by the solar mass splitting. Therefore, any measurable effect of neutrino oscillations must depend on the atmospheric mass splitting Δm_{32}^2 , so one can neglect Δm_{12}^2 in the analysis. In that case, the oscillation formulae become simpler and some parameters vanish from the theory.

By setting $\Delta m_{12}^2 = 0$ the oscillation phases (2.41c) become:

$$\phi_{12} = 0, \quad (2.72a)$$

$$\phi_{13} = \phi_{23}. \quad (2.72b)$$

Substituting this in the equation (2.42), and using the unitarity of the mixing matrix, one obtains:

$$P_{\alpha \rightarrow \alpha} = 1 - 4 |U_{\alpha 3}|^2 (1 - |U_{\alpha 3}|^2) \sin^2 \frac{\phi_{23}}{2}, \quad (2.73a)$$

$$P_{\alpha \rightarrow \beta; \alpha \neq \beta} = 4 |U_{\alpha 3}^* U_{\beta 3}|^2 \sin^2 \frac{\phi_{23}}{2}. \quad (2.73b)$$

The CP violating term has vanished from the oscillation probability equations. By assuming that two out of three neutrino masses are equal, the three-generation oscillation theory effectively becomes a two-generation theory, and the 2×2 generation mixing matrix has no physical phases (see Table 2.1). Since the presence of phases introduces the

imaginary component to the mixing matrix, which in turn induces the CP violation, the two generation neutrino oscillation theory can not have effects due to CP violation.

The oscillation probabilities now depend only on the third column of the PMNS mixing matrix (2.57). This means that there are only two independent mixing parameters left in the theory¹⁶. By inspection one finds that the free parameters remaining in the used parametrization are θ_{13} and θ_{23} .

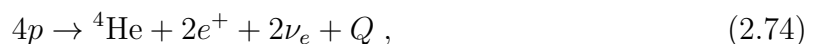
The total number of parameters in this approximation of neutrino oscillation theory is therefore 3 - two mixing angles and one mass splitting.

2.3 Neutrino sources

2.3.1 Natural sources

Solar neutrinos

The Sun is an intense source of neutrinos, produced in the fusion reactions which happen in the core of the Sun. At its current stage in the stellar evolution, the Sun is burning hydrogen to produce helium-4. This fusion process is simultaneously happening through a number of different branches, but the total effect is always the same:



where Q is total thermal energy released through the process. The two positrons quickly annihilate with the surrounding electrons, which provides an additional $4m_e$ of thermal energy to the Sun.

Each branch through which the fusion reaction (2.74) is taking place produces a different neutrino energy spectrum, the total neutrino energy spectrum of the Sun being the sum of spectra of all the branches. There are two main chains through which the proton-proton fusion takes place:

- The pp chain - the dominant process in the Sun, through which the majority of Sun's thermal energy and neutrinos is produced. This process starts with two protons

¹⁶ $U_{\alpha 1}$, $U_{\alpha 2}$ and $U_{\alpha 3}$ are not independent because of the unitarity condition $\sum_{i=1}^3 |U_{\alpha i}|^2 = 1$.

fusing and producing deuterium via a reaction:



This reaction is responsible for the vast majority of the Solar neutrino flux.

The alternative to this reaction is *pep* reaction, which includes electron capture on one of the protons in initial state:



Unlike the reaction (2.75), *pep* reaction produces monoenergetic neutrinos since there are only two particles in the final state (as opposed to three in the *pp* reaction).

The deuterium then fuses with a proton to produce helium-3:



After helium-3 production there are multiple paths this reaction can proceed, the most probable one is a direct fusion of ${}^3\text{He}$ to ${}^4\text{He}$:



- The CNO cycle - in this chain carbon, nitrogen and oxygen present in the Sun's core act as a catalyst for the reaction (2.74). This cycle is sub-dominant process in the stars with a relatively low core temperature such as the Sun. In more massive stars which have a hotter core, CNO cycle can overtake the *pp* chain in terms of energy production.

Nuclear reactions which produce neutrinos in the core of the Sun are shown in Table 2.2. Additional monoenergetic neutrinos are produced by electron capture on ${}^{13}\text{N}$, ${}^{15}\text{O}$ and ${}^{17}\text{F}$ which are called ecCNO neutrinos.

Solar neutrino fluxes are predicted by calculations based on the Standard Solar Model (SSM) [22]. The state-of-the-art fluxes are shown in Figure 2.5.

Table 2.2: A table of reactions inside the Sun core which produce neutrinos, both in the pp chain and in the CNO cycle. To see in which steps of the chain/cycle these reactions occur, one may consult Chapter 10.1 of [19]. Table taken from [21].

Reaction	Abbr.	Flux ($\text{cm}^{-2} \text{s}^{-1}$)
$pp \rightarrow d e^+ \nu$	pp	$5.98(1 \pm 0.006) \times 10^{10}$
$pe^- p \rightarrow d \nu$	pep	$1.44(1 \pm 0.01) \times 10^8$
${}^3\text{He } p \rightarrow {}^4\text{He } e^+ \nu$	hep	$7.98(1 \pm 0.30) \times 10^3$
${}^7\text{Be } e^- \rightarrow {}^7\text{Li } \nu + (\gamma)$	${}^7\text{Be}$	$4.93(1 \pm 0.06) \times 10^9$
${}^8\text{B} \rightarrow {}^8\text{Be}^* e^+ \nu$	${}^8\text{B}$	$5.46(1 \pm 0.12) \times 10^6$
${}^{13}\text{N} \rightarrow {}^{13}\text{C } e^+ \nu$	${}^{13}\text{N}$	$2.78(1 \pm 0.15) \times 10^8$
${}^{15}\text{O} \rightarrow {}^{15}\text{N } e^+ \nu$	${}^{15}\text{O}$	$2.05(1 \pm 0.17) \times 10^8$
${}^{17}\text{F} \rightarrow {}^{17}\text{O } e^+ \nu$	${}^{17}\text{F}$	$5.29(1 \pm 0.20) \times 10^6$

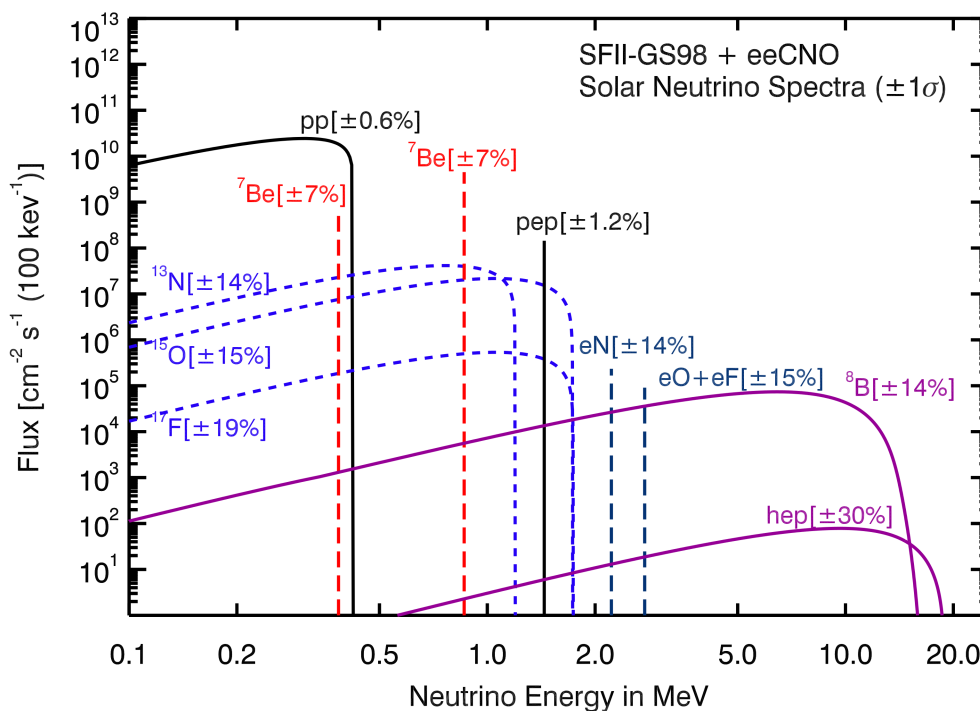


Figure 2.5: Various components of the Solar neutrino flux. Abbreviations of flux names are given in Table 2.2. Lines eN, eO and eF are neutrino fluxes produced in electron capture on ${}^{13}\text{N}$, ${}^{15}\text{O}$ and ${}^{17}\text{F}$, respectively. The numbers in square brackets are theoretical systematic uncertainties. This figure is taken from [21].

The flavour content of neutrinos exiting the Sun depend strongly on matter oscillation effects. The observed deficit of ν_e measured in the Solar flux was actually a first

experimental indication of neutrino oscillations¹⁷.

Atmospheric neutrinos

Atmospheric neutrinos are created in decays of secondary particles produced by interaction of the energetic cosmic rays with the Earth's atmosphere.

Cosmic rays with energies above 2 GeV per nucleon are composed mostly of protons ($\sim 95\%$) and helium nuclei ($\sim 4.5\%$). Their interactions with the upper layers of the atmosphere produce mesons, mostly pions and kaons. These mesons then decay producing neutrinos and corresponding charged leptons, mostly muons. Muon decays produce additional electron and muon neutrinos. Table 2.3 shows processes relevant for the atmospheric neutrino production.

Table 2.3: Processes relevant for atmospheric neutrino production. Process (A) describes the primary reaction of cosmic rays with the atmosphere with the most common reaction products. Processes (B1)-(D2) are the most common decay channels of mesons produced in reaction (A). Process (E) describes the (anti)muon decay. This table is taken from [21].

	Reaction/Decay	Branching ratio (%)
(A)	$p(n) + A \rightarrow \pi^\pm X, K^\pm X, K_L X$	
(B1)	$\pi^\pm \rightarrow \mu^\pm + \nu_\mu (\bar{\nu}_\mu)$	99.9877
(B2)	$\rightarrow e^\pm + \nu_e (\bar{\nu}_e)$	0.0123
(C1)	$K^\pm \rightarrow \mu^\pm + \nu_\mu (\bar{\nu}_\mu)$	63.56
(C2)	$\rightarrow \pi^0 + \mu^\pm + \nu_\mu (\bar{\nu}_\mu)$	3.352
(C3)	$\rightarrow \pi^0 + e^\pm + \nu_e (\bar{\nu}_e)$	5.07
(D1)	$K_L \rightarrow \pi^\pm + \mu^\mp + \bar{\nu}_\mu (\nu_\mu)$	27.04
(D2)	$\rightarrow \pi^\pm + e^\mp + \bar{\nu}_e (\nu_e)$	40.55
(E)	$\mu^\pm \rightarrow e^\pm + \bar{\nu}_\mu (\nu_\mu) + \nu_e (\bar{\nu}_e)$	100

Computing the atmospheric neutrino flux is quite a challenging task, since knowledge of many input phenomena is required - the composition of cosmic rays, earth's magnetic

¹⁷It is interesting that Bruno Pontecorvo started developing neutrino oscillation theory before the Solar neutrino deficit was measured. His first theories were about neutrino-antineutrino oscillations (absent from the modern theory) in analogy with K^0 - \bar{K}^0 oscillations. Only after Solar deficit measurement and discovery of the fact that there are more than one flavour of neutrino he developed his first version of flavour oscillation theory.

field model, model of the atmosphere, and hadronic interaction models (production rates of pions and kaons), to name a few. For instance, the low energy component of cosmic rays is deflected by the earth's magnetic field, so a knowledge of space weather is required to precisely compute the flux of atmospheric neutrinos with energies less than 1 GeV.

Detailed atmospheric flux calculations may be found, for instance in [23]. A set of calculated neutrino fluxes for different sites is shown in Figure 2.6.

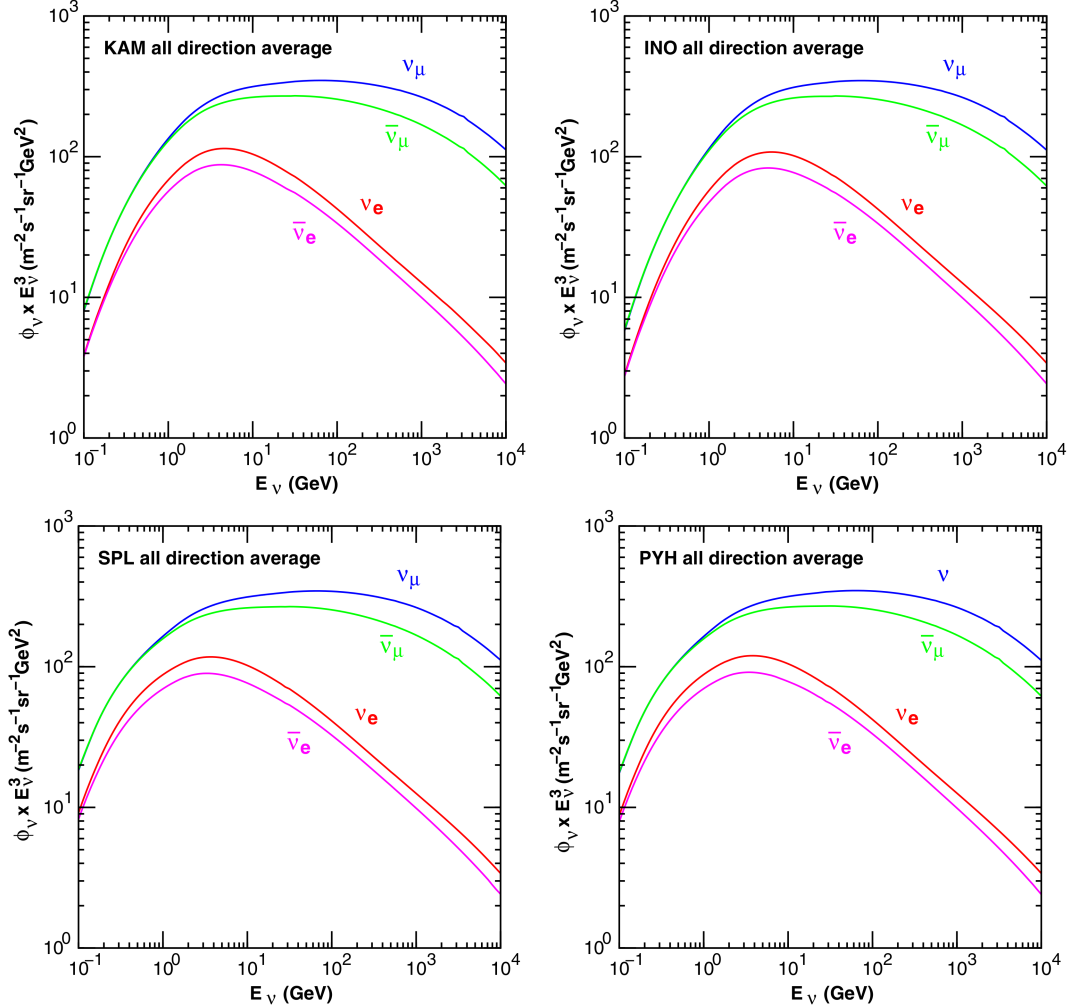


Figure 2.6: Time and direction averaged atmospheric neutrino fluxes in four different sites on Earth: KAM - Super Kamiokande site [24], INO - Indian Neutrino Observatory site [25], SPL - South pole, PYH - Pyhäsalmi mine. These fluxes are very similar because they are averaged over time and neutrino direction. They actually exhibit annual modulation and dependence on zenith and azimuthal angle of neutrino trajectories, which differ from site to site on the order of 10% [23]. Figure taken from [23].

Geoneutrinos

Geoneutrinos are neutrinos produced in the radioactive decay of naturally occurring radioactive isotopes in Earth. They are electron antineutrinos produced mainly from beta decay of primordial ^{40}K and beta decays of fissile products of primordial ^{238}U and ^{232}Th . Their energies are below 3.4 MeV. Apart from neutrino physics, measuring these neutrino sources is interesting in geo-sciences, as it adds additional information of the interior of the Earth which is currently unattainable by traditional methods. These neutrinos have been observed by Borexino [26] and KamLAND [1] experiments. More information can be found in [27, 28].

2.3.2 Artificial sources

Accelerator neutrino beams (superbeams)

Superbeam is a neutrino beam produced by colliding an accelerated proton beam on a target. The resulting long lived particles are mostly pions and kaons¹⁸, which then decay primarily into muons and muon neutrinos. The physical processes are the same as the ones involved in the creation of atmospheric neutrinos, shown in Table 2.3.

High energy proton beam is guided onto a target whose length is usually 1 - 2 interaction lengths¹⁹. The resulting secondary hadron beam is aligned in the same direction as the incoming proton beam due to Lorentz boost effects, and is additionally focused using a magnetic horn. Magnetic horn is a high-current, pulsed focusing device which selects the electric charge of particles coming from a point source by focusing them into a parallel beam; particles of the opposite charge are deflected to high angles to remove them from the beam. This allows for a selection between a neutrino and antineutrino beam, since positive hadrons decay into neutrinos and the negative ones into antineutrinos²⁰.

The focused beam of secondary particles is then lead to an evacuated²¹ decay tunnel

¹⁸These secondaries consist mostly of pions ($\sim 90\%$), the abundance of heavier hadrons like kaons and charmed particles increases with the proton energy.

¹⁹Interaction length is a mean free path of a particle between two nuclear interactions in a given material.

²⁰It is a matter of conservation of charge and lepton flavour - positive pions will decay into (positive) antimuon and a neutrino, while negative ones will decay into muon and antineutrino. Analogue argument is valid for all weak decaying hadrons, perhaps with a different flavour of charged lepton-neutrino pair.

²¹In some designs the decay tunnel is filled with helium gas instead.

in which they are allowed to decay in flight. The most common decay reaction is reaction (B1) in the Table 2.3, i.e. $\pi^\pm \rightarrow \mu^\pm + \nu_\mu(\bar{\nu}_\mu)$. These muon neutrinos are the primary component of a neutrino superbeam. The decays of muons are usually not desirable in the decay tunnel since they produce electron neutrinos, which is especially problematic in the $\nu_\mu \rightarrow \nu_e$ appearance experiments. Because of this, a length of decay tunnel is tuned to simultaneously maximize the number of secondary hadron decays and minimize the number of muon decays. A muon absorber is placed downstream of the decay tunnel in order to stop the muons before they decay. Muons at rest decay isotropically and the resulting neutrinos are not boosted, so their contribution to the highly directed and high energy primary neutrino beam is completely negligible.

Expected neutrino fluxes for a given beam line configuration are usually calculated using MC simulation software. Since the nuclear effects involved in the creation of superbeam are quite dirty (e.g. both primary proton and secondary hadron reinteractions in the target, kaon production, etc.), the error on the calculated fluxes is quite high (15% to 20% for the CNGS beam).

The resulting neutrino beam has a wide energy neutrino spectrum. A way to narrow down the energy spectrum is to place the far neutrino detector off of the main axis of the beam, the effect of which can be seen in Figure 2.7.

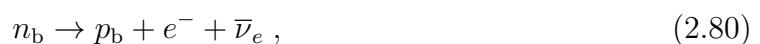
Reactor neutrinos

Reactor neutrinos are produced in β decays of fission products in nuclear reactors. These are dominantly β^- decays producing electron antineutrinos since fission products are neutron-rich nuclei. The production rate of ν_e is less than 10^{-5} times the production rate of $\bar{\nu}_e$.

The basic reaction in which reactor neutrinos are produced is



where X is a beta decaying nucleus and Y is its a decay product. The elementary reaction is a decay of a bound neutron



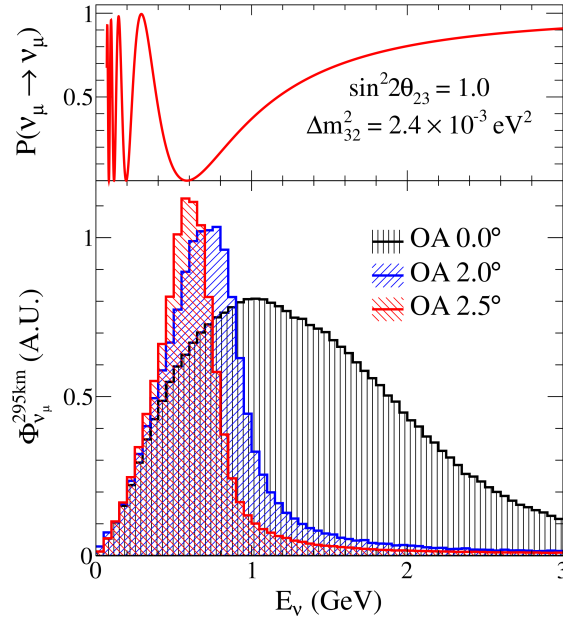


Figure 2.7: The ν_μ survival probability and neutrino flux as a function of neutrino energy at the 295 km baseline of the T2K beam. The expected neutrino fluxes for the three angles (0.0° , 2.0° , and 2.5°) between the detector position and beam axis are shown. Survival probability is shown for the angle 2.5° . Figure taken from [21].

where the subscript b indicates that the original neutron and the resulting proton are bound in the nucleus.

A similar method is used in virtually all reactor neutrino experiments, including the first ever experimental observation of a neutrino²² [29]. A hydrogen-rich scintillating target, instrumented by photomultiplier tubes, is exposed to a reactor $\bar{\nu}_e$ flux. Neutrino interacts with a hydrogen nucleus (a proton) via inverse beta decay reaction

$$p + \bar{\nu}_e \rightarrow n + e^+, \quad (2.81)$$

producing a neutron and a positron. The energy threshold for this reaction is 1.806 MeV, which implies that reactor neutrino experiments using this reaction to detect antineutrinos are insensitive to antineutrinos with energies $E_\nu \lesssim 1.81$ MeV.

Positron travels a short distance before stopping and annihilating with an environmental electron, producing a characteristic signal of two gamma photons. In addition to the γ pair, modern experiments are able to reconstruct a short positron track via scintillation

²²It was $\bar{\nu}_e$ from a reactor.

light it produces.

Neutron thermalizes after about $200 \mu\text{s}$ and is then captured in one of surrounding heavier nuclei. The de-excitation of a resulting nucleus produces a number of gamma rays which are again detected by surrounding photomultipliers.

The delayed coincidence between these two signals is a signature of $\bar{\nu}_e$ interaction, and it allows for a very strong background rejection. This is the reason why reactor neutrino detectors do not have to be located as deep underground as detectors of other neutrino sources.

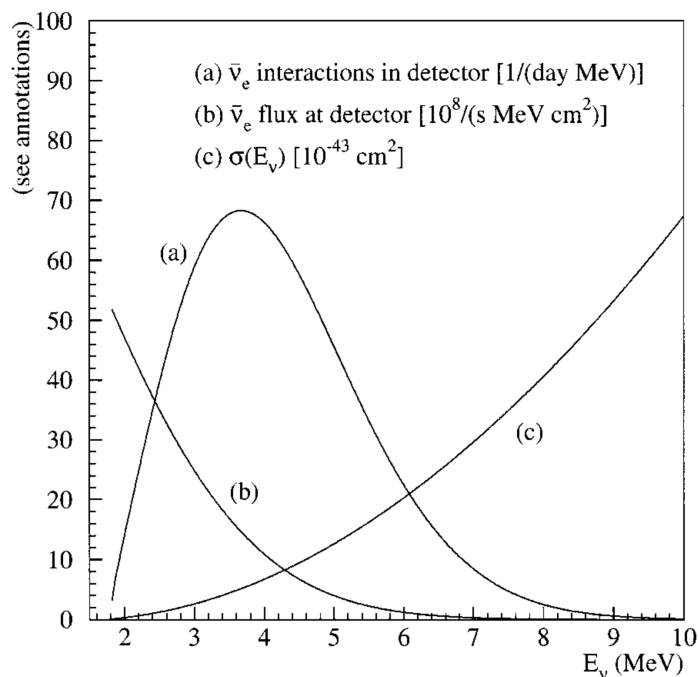


Figure 2.8: A plot as a function of neutrino energy of (a) A predicted $\bar{\nu}_e$ interaction rate in a 12 t fiducial mass of a detector located 0.8 km away from a $12 \text{ GW}_{\text{th}}$ nuclear reactor, (b) $\bar{\nu}_e$ flux predicted at the detector site, (c) inverse β -decay cross section. Figure taken from [30].

Bulk of the power in nuclear reactors is generated by fission of four fissile isotopes, ^{235}U , ^{238}U , ^{239}Pu , and ^{241}Pu . Daughter nuclei of these fission products undergo 6 β -decays on average, meaning that 6 $\bar{\nu}_e$ are emitted per fission reaction. Knowing that the effective thermal energy released per fission is about 200 MeV, one can deduce that about $2 \cdot 10^{20}$ $\bar{\nu}_e$ are emitted per 1 GW of nuclear reactor's thermal output. Power plant companies provide the thermal output of the reactor and amount of fissile isotope present in the fuel, which allows for a more detailed semi-empirical calculation of reactor neutrino fluxes and

their energy spectra [30].

An example of a calculated reactor neutrino flux is shown in Figure 2.8. Note that the energy²³ of reactor neutrinos is well below the mass of muon and tau leptons, making these flavours unobservable via CC interactions on a fixed target. Therefore, reactor neutrino experiments can observe neutrino oscillation only in disappearance mode.

2.4 Current experimental values of neutrino oscillation parameters

At the time of writing, all parameters of the 3-generation neutrino model except the CP violating phase δ_{CP} have been measured with sufficient accuracy to exclude the possible degeneracies²⁴ in the three neutrino generation oscillation theory. The current state-of-the-art experimental values are shown in Table 2.4.

Table 2.4: Current experimental values of known neutrino oscillation parameters. The quoted uncertainties are 1σ (i.e. 68%) confidence intervals. NH and IH stand for normal and inverted mass hierarchy, respectively. A name commonly used in the neutrino community is indicated for each parameter. Data is taken from [21].

Parameter	Experimental value	Name
Δm_{21}^2	$(7.53 \pm 0.18) \cdot 10^{-5} \text{eV}^2$	Solar mass splitting
Δm_{32}^2	$\begin{cases} (2.45 \pm 0.05) \cdot 10^{-3} \text{eV}^2 & \text{(NH)} \\ (-2.52 \pm 0.05) \cdot 10^{-3} \text{eV}^2 & \text{(IH)} \end{cases}$	Atmospheric mass splitting
$\sin^2 \theta_{12}$	$0.307^{+0.013}_{-0.012}$	Solar mixing angle
$\sin^2 \theta_{32}$	$\begin{cases} 0.51 \pm 0.04 & \text{(NH)} \\ 0.50 \pm 0.04 & \text{(IH)} \end{cases}$	Atmospheric mixing angle
$\sin^2 \theta_{13}$	$(2.10 \pm 0.11) \cdot 10^{-2}$	Reactor mixing angle

All experiments designed so far to measure neutrino oscillation parameters are sensitive to a single mass splitting and a single mixing angle, with other oscillation parameters contributing to the observed data as a second order effect. The parameter pair to which an experiment is most sensitive is determined by the initial flavour and energy of neutrinos

²³The reactor neutrinos have higher energy than geoneutrinos because nuclear fuel undergoes fission under intense neutron flux, unlike fission reactions produce geoneutrinos. Because of this ^{238}U and ^{232}Th have different fission chains in reactor than in the ground, producing antineutrinos with different energies.

²⁴A degeneracy would be if any of $\Delta m_{ij}^2 = 0$, or any of euler angles satisfy the conditions $\sin \theta_{ij} = 0$ or $\cos \theta_{ij} = 0$.

it is observing, and the distance of the detector from the point of neutrino creation (i.e. its baseline).

Reactor neutrino experiments are observing antineutrinos which are initially in pure electron flavour state with energies of the order of 5 MeV. They are sensitive only to electron neutrino disappearance since the energy of neutrinos is not high enough to produce charged leptons other than electrons. Since the disappearance channel is CP invariant (see Chapter 2.2.3), reactor neutrinos are completely insensitive to the CP violating phase δ_{CP} . Depending on their baseline, they are most sensitive to either $\Delta m_{21}^2 - \sin^2 \theta_{12}$ pair with long baseline or $\Delta m_{32}^2 - \sin^2 \theta_{13}$ pair with short baseline (see Figure 2.9).

Neutrinos produced in the Sun, observed by the Solar neutrino experiments, are initially in a distorted flavour state due to the high concentration of electrons in the core of the Sun. During the transit from the core to the surface of the Sun, their oscillation probabilities are dominated by matter effects and cannot be described by the formula for neutrino oscillations in vacuum (2.42). Due to large distance between the Sun and Earth compared to oscillation wavelength, vacuum oscillations are averaged out at terrestrial detection sites. As in reactor experiments, energies of Solar neutrinos do not allow production of muons or tau leptons via CC interactions. Therefore, Solar neutrino experiments are sensitive only to the ν_e component of the Solar neutrino flux on Earth²⁵, which is predicted by the SSM and the theory of neutrino oscillations in matter. They are most sensitive to $\Delta m_{21}^2 - \sin^2 \theta_{12}$ pair. Since neutrino oscillations in matter depend on sign of the mass splitting, the sign of Δm_{21}^2 is determined by Solar neutrino experiments to be positive.

Atmospheric and superbeam experiments are observing neutrinos and antineutrinos created in pure muon flavour. These experiments can measure oscillations in both disappearance and appearance mode since neutrino energies are sufficient to produce muons and electrons via CC interactions. For the $\nu_\mu \rightarrow \nu_\tau$ appearance channel, NuMI and CNGS beams are energetic enough to produce tau leptons via CC interactions (as is the atmospheric neutrino flux), while T2K beam is not energetic enough to produce tau leptons in any detectable quantities. These experiments are most sensitive to $\Delta m_{32}^2 - \sin^2 \theta_{23}$

²⁵With the exception of SNO experiment [31, 32] which was sensitive to the total Solar neutrino flux via NC interactions.

pair (often called the *atmospheric*²⁶ sector), through measuring $\nu_\mu(\bar{\nu}_\mu)$ disappearance or $\nu_\tau(\bar{\nu}_\tau)$ appearance (see Figure 2.10).

The global fit value of Δm_{32}^2 , quoted in Table 2.4, is obtained by the joint fit of short baseline reactor experiments data and atmospheric sector data in disappearance mode.

2.4.1 Measurement of Δm_{21}^2 and $\sin^2 \theta_{12}$

The current experimental values of Δm_{21}^2 and $\sin^2 \theta_{12}$, quoted in Table 2.4, are determined by measurements of KamLAND experiment and the Solar neutrino data.

KamLAND[1] experiment is a long-baseline reactor neutrino experiment²⁷, located under Mount Ikenoyama in Japan. It observed electron antineutrinos from more than 50 nuclear power plants in Japan. Its neutrino target is 1 kt liquid scintillator instrumented by 1325 photomultiplier tubes. Neutrino interactions are identified by method of delayed coincidence described in Chapter 2.3.2. The effective flux-weighted baseline of the experiment is 180 km and the neutrino energy acceptance about $(1.8 - 9.3)$ MeV, which corresponds to L/E coverage of roughly $(20 - 100) \cdot 10^3$ GeV/km. This design makes it sensitive to electron neutrino disappearance driven by $\sin^2 \theta_{12}$ and Δm_{12}^2 (see Figure 2.9). The experiment is much more sensitive to the mass splitting than the mixing angle because mass-splitting determines energy dependence of $\bar{\nu}_e$ disappearance, making it possible measure it by using the shape analysis of disappearance data. Mixing angle determines the amplitude of disappearance, measurement of which is dominated by the uncertainty of initial reactor neutrino fluxes. The combined fit of KamLAND and Solar data is shown in Figure 2.11.

2.4.2 Measurements of Δm_{32}^2 and $\sin^2 \theta_{13}$

The modern experiments most sensitive to $\sin^2 \theta_{13}$ and Δm_{32}^2 are the short baseline reactor experiments measuring the disappearance of $\bar{\nu}_e$ reactor neutrinos around the first Δm_{32}^2 -driven disappearance maximum (see Figure 2.9), and the atmospheric and long baseline superbeam experiments which can measure the $\nu_e(\bar{\nu}_e)$ appearance in $\nu_\mu(\bar{\nu}_\mu)$ neutrino fluxes around the first Δm_{32}^2 driven appearance maximum (see Figure 2.10).

²⁶Because this sector was first probed by atmospheric neutrino experiments

²⁷It is the only long-baseline reactor neutrino experiment in the world.

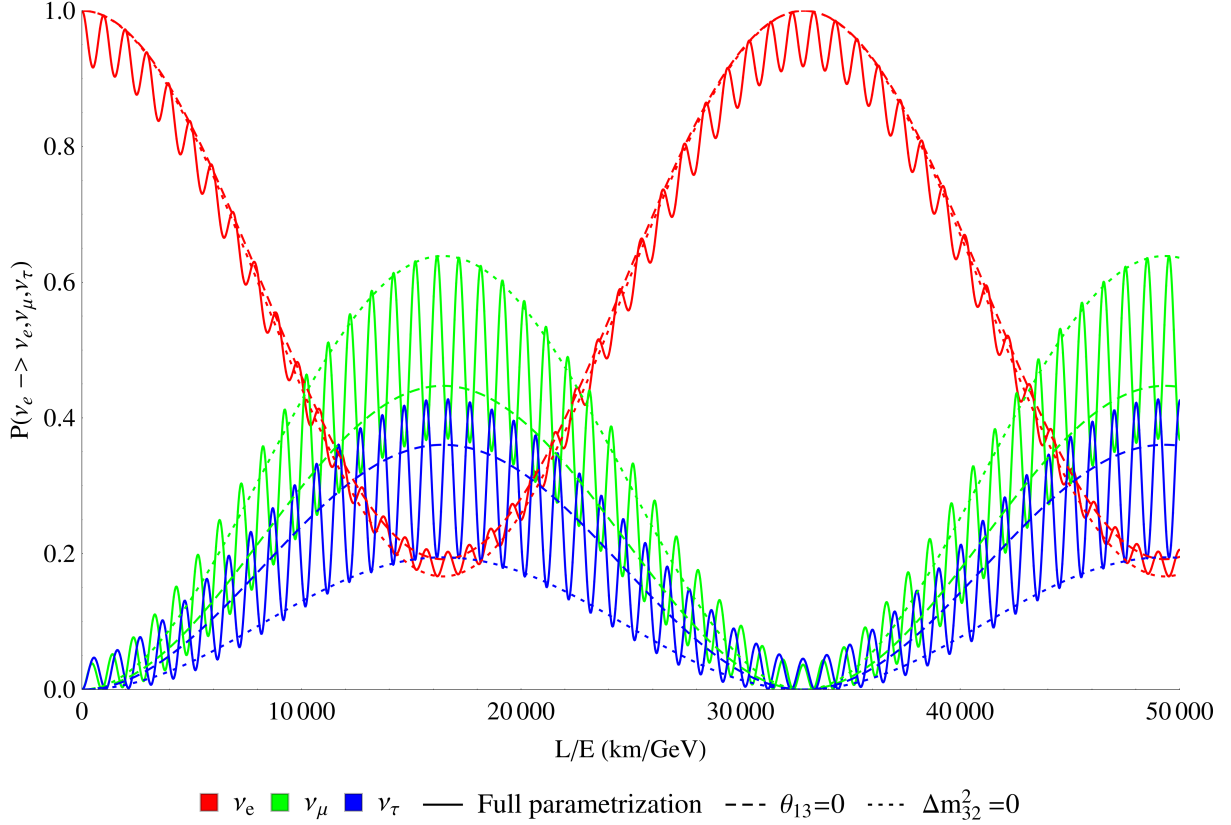


Figure 2.9: Neutrino oscillation probabilities for 3-generation mixing as a function of L/E with initial neutrino in pure ν_e or $\bar{\nu}_e$ state. The oscillation parameters used for the plot are central values (NH) quoted in Table 2.4 and $\delta_{\text{CP}} = 0$. (i) solid lines show full 3-generation oscillation probabilities, (ii) dashed lines show oscillation probabilities in case $\sin \theta_{13} = 0$ with all other parameters intact, (iii) dotted lines show probabilities in case $\Delta m_{32}^2 = 0$ and all other parameters intact. The full mixing oscillation probabilities in this region of L/E may be described by short-wavelength quasi-periodic oscillations enveloped by a longer wavelength quasi-periodic oscillation. The short-wavelength oscillations are driven by Δm_{32} and $\sin^2 \theta_{13}$, demonstrated by the fact that they are not present when either of the two parameters is set to zero. The longer wavelength corresponding to the envelope is driven by Δm_{12}^2 and $\sin^2 \theta_{12}$.

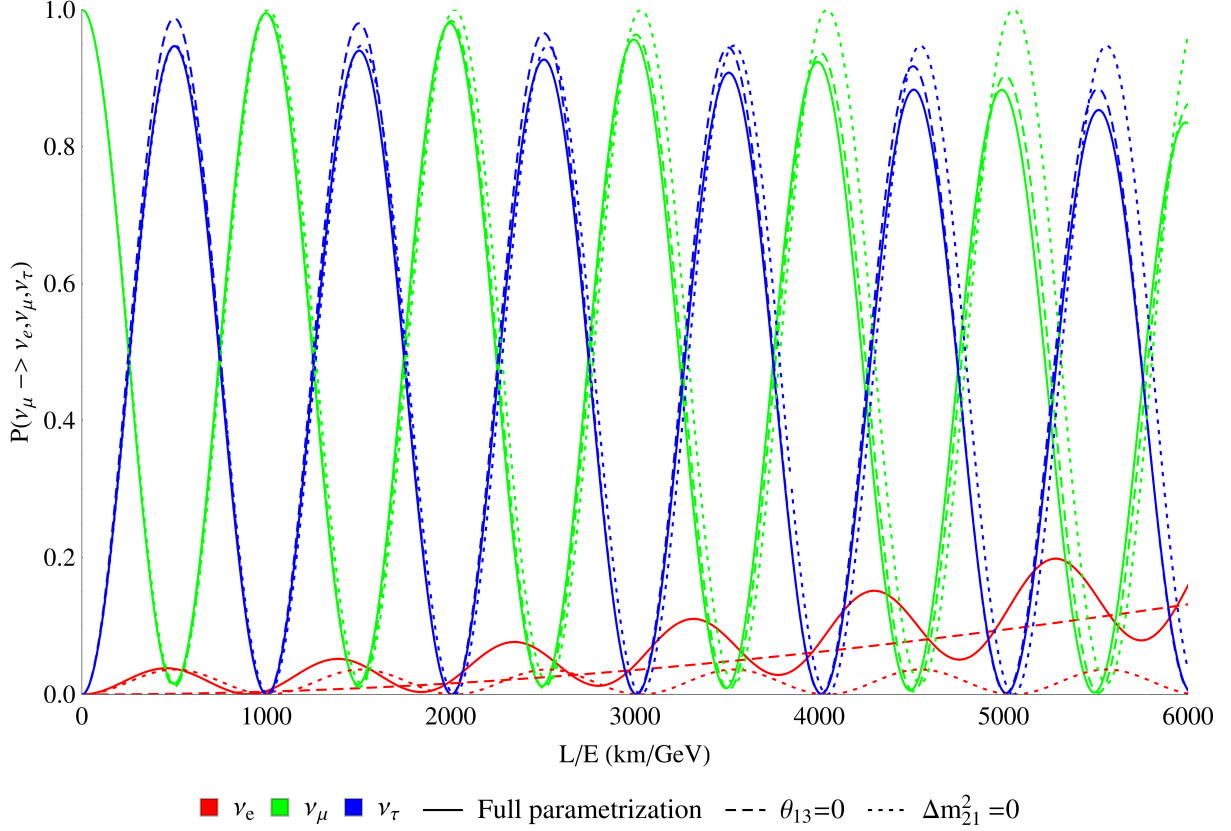
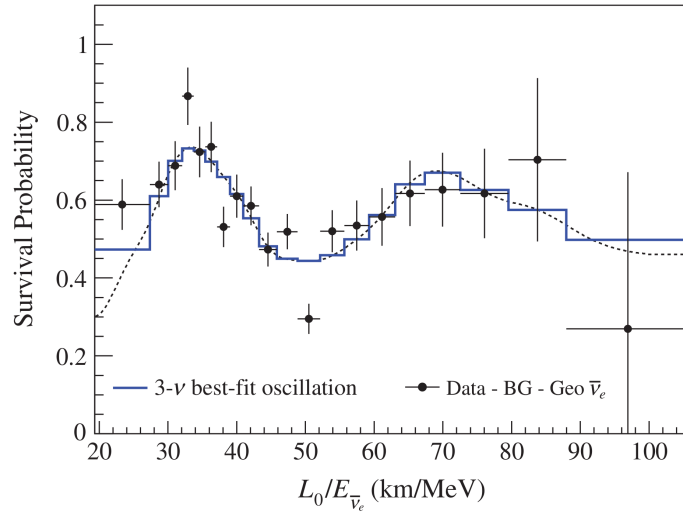
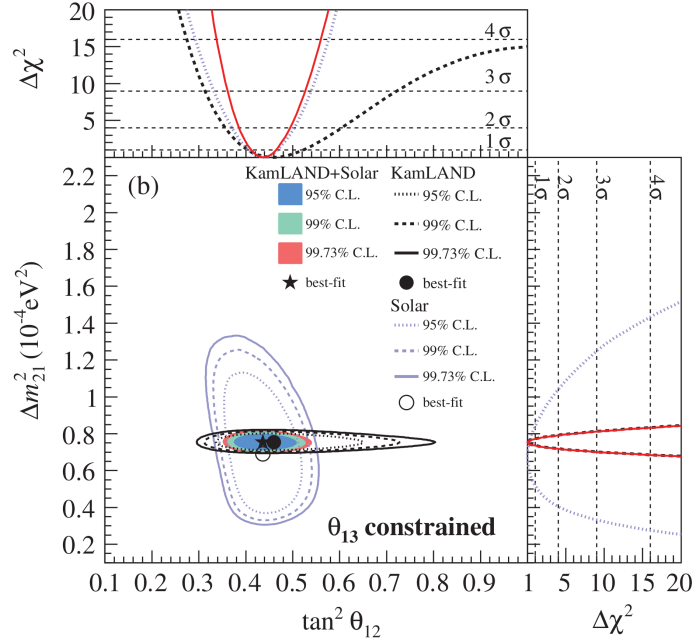


Figure 2.10: Neutrino oscillation probabilities for 3-generation mixing as a function of L/E with initial neutrino in pure ν_μ or $\bar{\nu}_\mu$ state. The oscillation parameters used for the plot are central values (NH) quoted in Table 2.4 and $\delta_{\text{CP}} = 0$. (i) solid lines show full 3-generation oscillation probabilities, (ii) dashed lines show oscillation probabilities in case $\theta_{13} = 0$ with all other parameters intact, (iii) dotted lines show probabilities in case $\Delta m_{21}^2 = 0$ and all other parameters intact. In this region of L/E , the full mixing oscillations may be described by near maximal conversion $\nu_\mu \leftrightarrow \nu_\tau$ driven by Δm_{32}^2 , with the small $\nu_\mu \rightarrow \nu_e$ appearance probability which rises with L/E . In the case of $\theta_{13} = 0$, there are no ν_e appearance oscillations driven by Δm_{32}^2 , making this channel negligible at the first Δm_{32}^2 oscillation maximum (there is still $\nu_\mu \rightarrow \nu_e$ appearance driven by Δm_{21}^2 relevant only at larger values of L/E).



(a) Survival probability of electron antineutrinos vs. L/E measured by the KamLAND experiment. To be compared with Figure 2.9.



(b) Fit results and confidence intervals in the $(\Delta m_{32}^2, \tan^2 \theta_{12})$ plane with θ_{13} constrained for (i) joint KamLAND and Solar data (colored contours), (ii) KamLAND data (filled black contours), (iii) Solar data (blue contours).

Figure 2.11: KamLAND experiment and Solar neutrino joint neutrino oscillation analysis. Figures taken from [1].

Currently, measurements of θ_{13} in the appearance mode have an uncertainty by an order of magnitude larger than the short baseline reactor experiments because of lower statistics, which is mostly due to lower intensity of neutrino flux and larger background. Therefore, their results are not included by a global fit performed by the Particle Data

Group [21]. The measurements of θ_{13} in the appearance mode have been reported by T2K [6] and MINOS [7], while the upper limits have been reported by Super-Kamiokande [33] and OPERA [8, 9].

The experimental value of $\sin^2 \theta_{13}$ quoted in the Table 2.4 is a result of a joint fit of measurements done by three short baseline reactor experiments: Daya Bay [2, 3], RENO [4] and Double-Chooz [5].

Table 2.5: Reactor power, neutrino energies and baselines for the three reactor neutrino experiments. W_{th} is a total thermal power of the nuclear plant, shown by multiplying the number of reactor cores with their power. E_ν is roughly the neutrino energy acceptance region of an experiment, it should be taken as illustrative values as it depends on energy cuts used in the analysis. L_N and L_F are the distances of near and far detectors, respectively; Double Chooz and RENO report flux-normalized distances, while Daya Bay reports absolute distances. L_N/E and L_F/E are L/E sensitivity ranges for near and far detector, respectively.

Experiment	W_{th}/GW	E_ν/MeV	L_N/m	L_F/km	$\frac{L_N}{E} / \frac{\text{km}}{\text{GeV}}$	$\frac{L_F}{E} / \frac{\text{km}}{\text{GeV}}$
Double Chooz	2×4.25	$1.8 - 8?$	400	1.05	$50 - 220$	$131 - 583$
Daya Bay	6×2.9	$2.3 - 12.8$	$360 - 470$	$1.52 - 1.93$	$28 - 204$	$118 - 843$
RENO	6×2.8	$2.0 - 8.8$	410	1.445	$46 - 205$	$164 - 516$

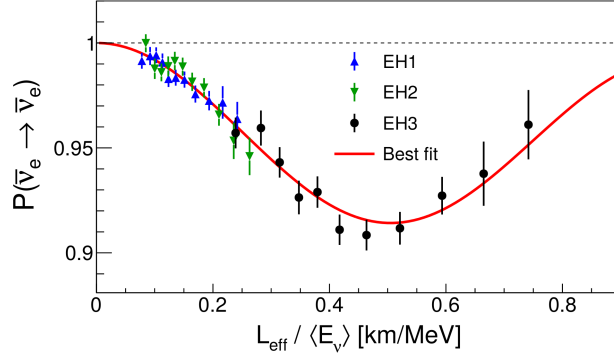
The baseline parameters of the three experiments are shown in Table 2.5. By comparing their L/E parameters with Figure 2.9, one can see that all three experiments are sensitive to the first $\bar{\nu}_e$ disappearance maximum driven by Δm_{32}^2 .

As an example, experimental results of the Daya Bay reactor neutrino experiment are shown in Figure 2.12.

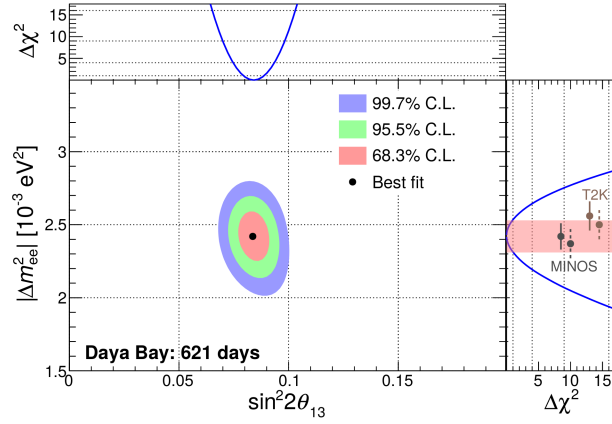
2.4.3 Measurements of Δm_{32}^2 and $\sin^2 \theta_{23}$

The experiments most sensitive to the $\Delta m_{32}^2 - \sin^2 \theta_{23}$ pair are the ones measuring neutrinos coming from initial ν_μ or $\bar{\nu}_\mu$ flux, i.e. atmospheric neutrino and superbeam experiments. The parameters are extracted through measurement of disappearance of the original $\nu_\mu(\bar{\nu}_\mu)$ flux around the first oscillation maximum (see Figure 2.10). The value of $\sin^2 \theta_{23}$ quoted in Table 2.4 is obtained by fitting the results of three long baseline superbeam experiments NO ν A [10], T2K [11] and MINOS²⁸ [12], combined with atmospheric neutrino data measured by Ice Cube [13].

²⁸MINOS analysis includes measurement of both accelerator neutrinos and atmospheric neutrinos in the MINOS detector.



(a) Survival probability of electron antineutrinos vs. L/E measured by the Daya Bay experiment. To be compared with Figure 2.9.



(b) Fit result and confidence interval in the $(|\Delta m_{ee}^2|, \sin^2 2\theta_{12})$ plane obtained by Daya Bay experiment data. The connection between $|\Delta m_{ee}^2|$ and Δm_{32}^2 is given by the formula $|\Delta m_{ee}^2| = |\Delta m_{32}^2| \pm \Delta m_{\phi}^2/2$, where $\Delta m_{\phi}^2/2$ is a term originating from solar mass splitting and the sign is dependant on the neutrino mass ordering (NH or IH). More details can be found in [2].

Figure 2.12: Daya Bay experimental results. Figures taken from [2].

Table 2.6: Neutrino energies and baselines for the three long-baseline superbeam experiments. E_ν is approximate FWHM range of neutrino energy spectrum; NO ν A reports FWHM of their beam energy spectrum, values for T2K and MINOS have been approximated by the author from published neutrino spectrum plots. L is a distance from the neutrino source to the far detector (all three experiments also feature a near detector). By comparison of L/E ranges with Figure 2.10, one can see that they are all sensitive to the first maximum of oscillations driven by Δm_{32}^2 .

Experiment	E_ν/GeV	L/km	$L/E/(\text{km/GeV})$
NO ν A	1 – 3	810	270 – 810
T2K	0.4 – 0.8	295	368 – 737
MINOS	2 – 4	735	183 – 376

A comparison of allowed regions in the $\Delta m_{32}^2 - \sin^2 \theta_{23}$ for the three long-baseline experiments is shown in Figure 2.13.

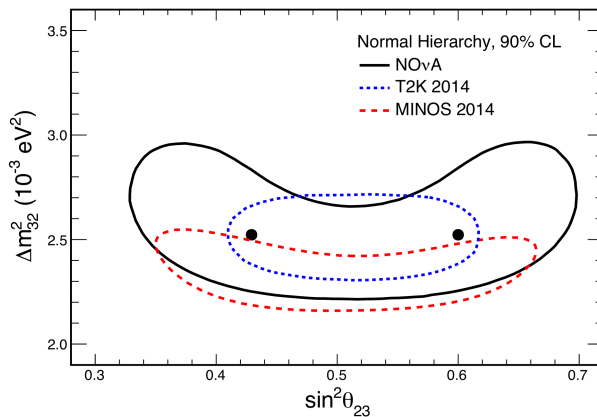


Figure 2.13: Results from the $\text{NO}\nu\text{A}$ experiment superimposed with the results of T2K and MINOS. The contours are allowed regions of oscillation parameters at 68% C.L. Figure taken from [12].

Measurement of these parameters is also possible via $\nu_\mu \rightarrow \nu_\tau$ appearance, but is much less sensitive due to (i) production threshold of τ lepton due to its large mass, resulting in decreased statistics²⁹, and (ii) difficulty in discriminating ν_τ CC interactions from background due to short flight length of τ lepton. At the time of this writing, only OPERA experiment has published a measurement of oscillation parameters in appearance mode [14].

²⁹If the beam energy is too low, there are no ν_τ interactions at all.

Chapter 3

The OPERA experiment

The OPERA experiment has been designed to detect the $\nu_\mu \rightarrow \nu_\tau$ neutrino oscillation channel in the appearance mode, i.e. by observing the tau neutrino. The source of neutrinos is the predominantly ν_μ CNGS beam produced at CERN, which has a negligible tau neutrino contamination (~ 1 ppm).

3.1 CNGS beam

The CERN neutrino to Gran Sasso (CNGS) beam is a neutrino superbeam (see Chapter 2.3.2) produced at the Super Proton Synchrotron¹ (SPS) located at CERN. The 400 GeV proton beam is directed onto a carbon target, producing pions and kaons.

The Secondary Emission Monitor is placed immediately downstream of the target to measure the efficiency with which protons are converted into secondaries². This was used to calibrate the positioning of the proton beam relative to the target to achieve the maximum efficiency of production of secondary particles.

Next downstream is the two-lens³ focusing system which selects the particles with positive charge and directs them towards the *decay tunnel* - a 1000 m long vacuum pipe called in which pions and kaons are allowed to decay, producing CNGS neutrinos and muons. The hadrons that did not decay in the tunnel are stopped in the *hadron stop*, composed of 18 m long block of graphite and iron located downstream of the decay tunnel.

¹CNGS actually shares the SPS extraction channel with one of the two LHC proton beams.

²Mostly pions, kaons and muons.

³Both lenses are magnetic horns.

Stopped pions and kaons decay isotropically and the resulting neutrinos are not boosted⁴, making their contribution to the CNGS beam completely negligible. Only muons and neutrinos are present in the beam downstream of the hadron stop.

To control the aim of the neutrino beam, muon beam component⁵ is monitored in the two muon detector stations located downstream of the hadron stop. Muons stop in the rock downstream of muon detectors, leaving neutrinos as the only remaining beam component.

The CNGS facility is schematically shown in Figure 3.1.

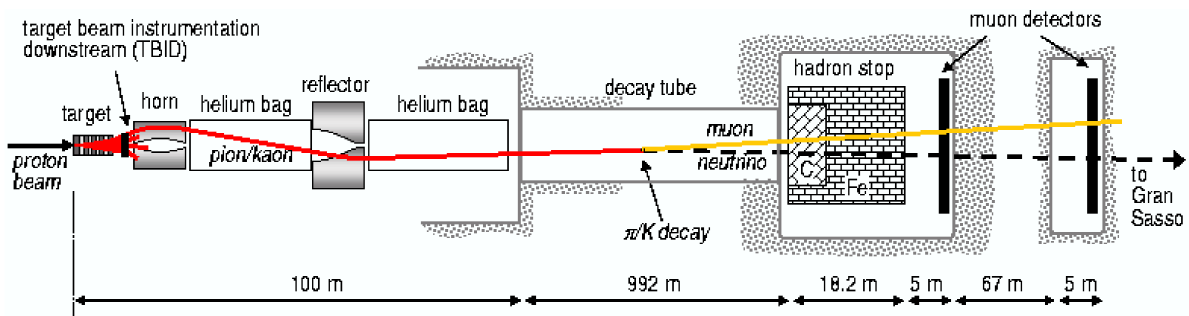


Figure 3.1: Schematic view of the CNGS facility.

The CNGS neutrino flux at the site of the OPERA detector is calculated using FLUKA MC software. Energy spectra of four flavour components of the CNGS beam are shown in Figure 3.2. The beam is dominated by the ν_μ , with the rest of the neutrino flavours contributing by about 4% to the total flux.

During the nominal CNGS cycle, there are two proton beam extractions every 6 s, separated by 50 ms and lasting $10.5 \mu\text{s}$ each. This allows for a very strong background rejection technique employed in the OPERA experiment, wherein only neutrino events which happened as a result of the short extraction durations are retained.

3.2 OPERA baseline

The baseline of the OPERA experiment is 732 km, which corresponds to the peak value of $L/E \approx 35 \text{ km/GeV}$ for the ν_μ component of the CNGS beam (see Figure 3.3).

⁴Neutrinos produced by pions at rest have energies of the order of 10 MeV, while those produced by kaons have about 100 MeV. This is to be compared with 15 GeV neutrinos produced by mesons decaying in the decay tunnel.

⁵The muon angular distribution is effectively identical to that of neutrinos.

CNGS beam spectra

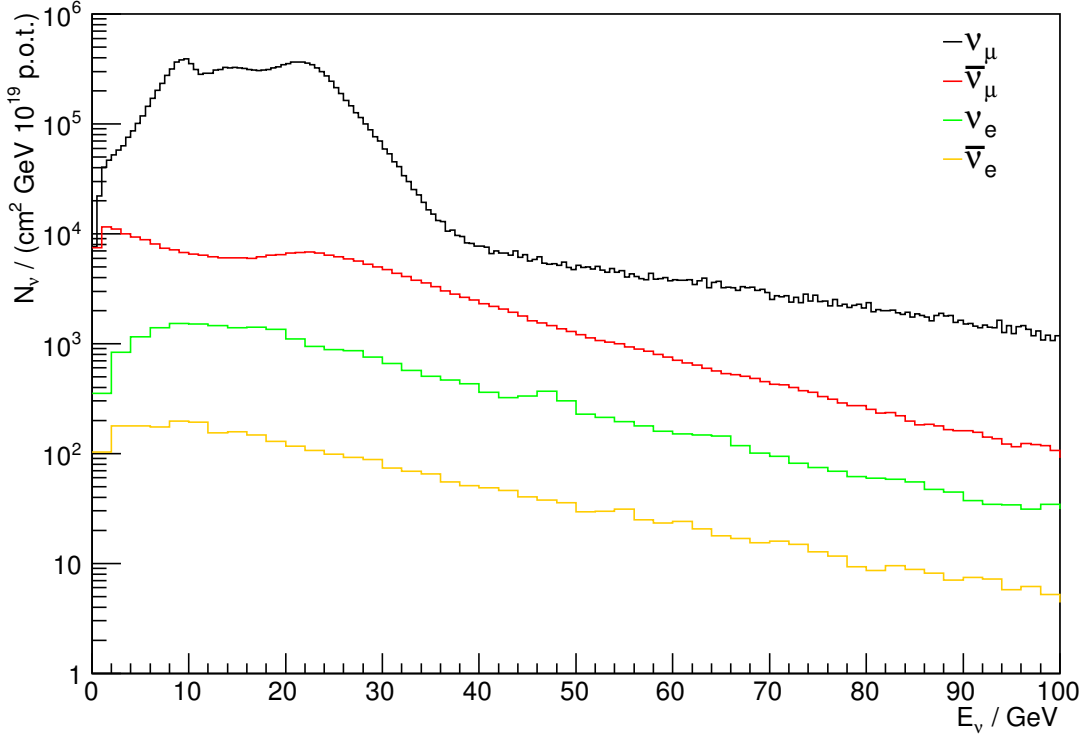


Figure 3.2: CNGS neutrino energy spectra for different neutrino flavours.

Table 3.1: Oscillation probabilities at $L/E = 35$ km/GeV using full three-generation mixing with parameters quoted in Table 2.4.

Channel	Oscillation probability (%)
$\nu_\mu \rightarrow \nu_e$	0.05
$\nu_\mu \rightarrow \nu_\mu$	98.8
$\nu_\mu \rightarrow \nu_\tau$	1.15

The oscillation probabilities at this value of L/E are quoted in Table 3.1.

As one can see, the oscillation probabilities at OPERA baseline and neutrino energy are far from the oscillation maximum.

Decreasing the neutrino energy in order to increase L/E , and therefore the oscillation probabilities, was not possible due to the τ production threshold.

Increasing the baseline, apart from being an obvious technical challenge, would actually not increase the number of observed tau neutrinos. This is because the $\nu_\mu \rightarrow \nu_\tau$ oscillation probability increases roughly with square of the baseline L^2 , and the intensity of the beam decreases as $1/L^2$ due to inevitable angular spread of the neutrino beam. These two terms cancel out, meaning that the effective ν_τ flux at the detector site does

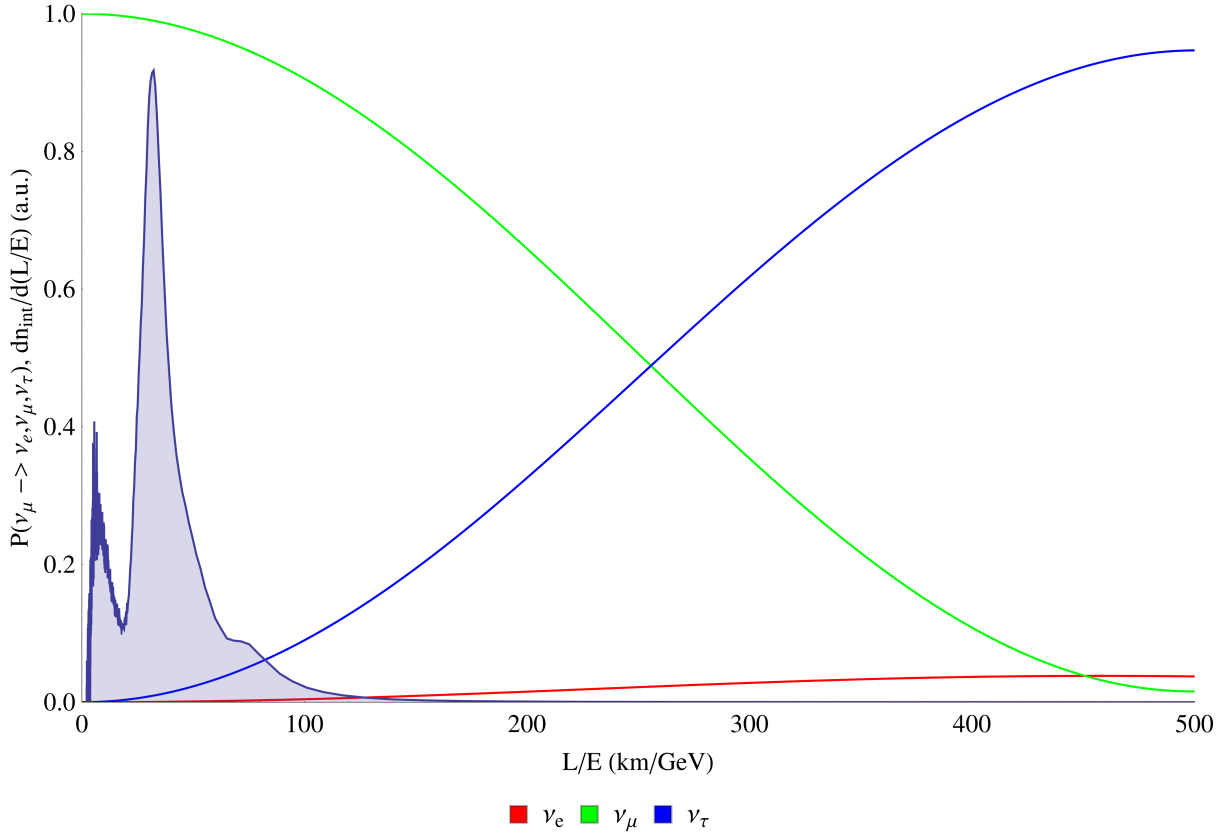


Figure 3.3: Muon neutrino oscillation probabilities in the full 3-generation mixing (colored lines) superimposed with CNGS ν_μ unoscillated interaction spectrum (shaded plot). Interaction spectrum is given in arbitrary units, the number of expected ν_μ interactions in any L/E interval is proportional to the integral of this curve in that interval.

not depend on the distance between the source and the detector below the first oscillation maximum. Decreasing the baseline would increase the number of observed ν_μ CC events because the beam would be less dispersed, while the number of observed ν_τ events would be constant. Thus, placing the detector too close to the beam source would make ν_τ events harder to find among the increased number of ν_μ interactions.

To see that the appearance probability is proportional to L^2 , one may use oscillation equations (2.73), which in the case of $\nu_\mu \rightarrow \nu_\tau$ appearance yield:

$$P_{\nu_\mu \rightarrow \nu_\tau} = 4s_{23}^2 c_{23}^2 c_{13}^4 \sin^2 \frac{\Delta m_{32}^2 L}{4E} \approx 4s_{23}^2 c_{23}^2 c_{13}^4 \left(\frac{L}{4E} \right)^2 (\Delta m_{32}^2)^2. \quad (3.1)$$

Since $(\sin^2 kL)/L^2$ actually decreases with L , positioning the OPERA detector on the first oscillation maximum would result in the measurement of less τ events than in the

current position. Also, it would drastically decrease the number of ν_μ events⁶.

3.3 The OPERA detector

The flavour of a neutrino is determined by measuring the flavour of the outgoing lepton in a charge-current (CC) neutrino interaction. Since the *tau* lepton produced by the ν_τ CC interaction decays after having travelled for about 1 mm, the detector needs to have a very high spatial resolution. On the other hand, since the neutrino interaction cross section is extremely small, the target mass must be sufficiently high to allow for a reasonable event rate. To meet both of these requirements, the OPERA detector is a *hybrid* detector - it is composed of very high spatial resolution nuclear emulsion detectors used for precision particle tracking, complemented by an assortment of electronic particle detectors used to estimate the position of the neutrino interaction vertex, and to provide charged particle spectroscopy, calorimetry and timing.

3.3.1 Emulsion cloud chamber - ECC

OPERA emulsion cloud chamber (ECC) detector, also known as a *brick*, is composed of 57 emulsion sheets interleaved with 56 lead plates (see Figure 3.4). These lead plates are the primary target mass of the experiment. Two additional emulsion plates called *Changeable Sheet* (CS) are located immediately downstream of the ECC, and are used as a trigger for further brick processing, i.e. as an interface between the ECC and the electronic detectors. There are total of about 150 thousand ECC bricks in the OPERA detector, making up a total of 1.25 kt target mass and more than 0.1 km² of active emulsion sheets.

OPERA nuclear emulsion is made of small silver bromide crystals (AgBr) suspended in gelatin. It is exactly the same technology used for every photographic film, one can actually make photographs using OPERA emulsion⁷. However, compared to a photographic film, the OPERA emulsion has larger density of crystals, which are smaller and

⁶One would have a situation in which OPERA sees only a few neutrino interactions of any flavour during the entire 5-year run.

⁷For a photograph of the OPERA detector using the OPERA emulsion as a photographic film, see the Appendix C.

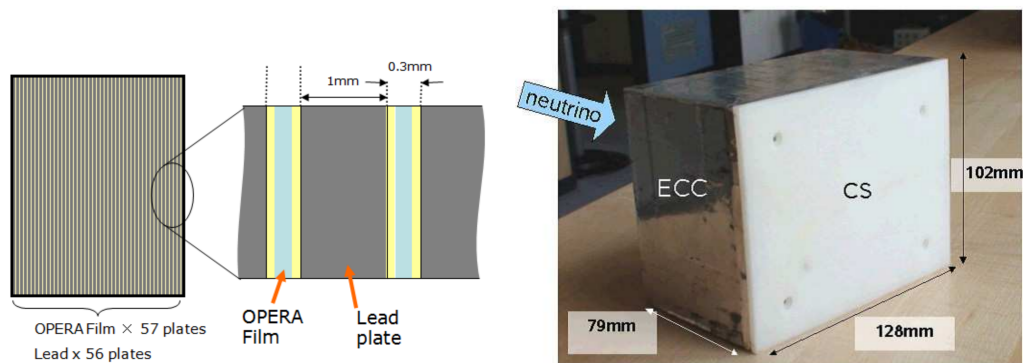


Figure 3.4: Schematic view of the OPERA ECC.

very uniform in size and sensitivity, and lower number of developed non-activated crystals.

The size of the AgBr crystal is about $0.2\ \mu\text{m}$, which defines the spatial resolution of the emulsion detector. When an ionizing particle passes through an AgBr crystal it becomes *activated*. After applying the emulsion development procedure, only the activated crystals remain in the emulsion in the form of pure silver. Thus, after development, tracks of electromagnetic particles are visible as tracks of silver grains in the emulsion. More information can be found in [34].

The OPERA emulsion sheet consists of a plastic base coated on both sides by an OPERA emulsion film developed by the FUJI Corporation, Japan. Its dimensions and grain sizes are shown in Table 3.2.

Table 3.2: OPERA emulsion sheet dimensions and grain sizes

Lateral dimensions	125 mm \times 100 mm
Plastic base thickness (average)	100 μm
Emulsion thickness (average)	44 μm
AgBr grain radius (undeveloped)	0.2 μm
AgBr grain radius (developed)	0.6 μm

A single emulsion layer in the emulsion sheet provides a 3-D segment of a particle track⁸, since the passing particle activates the grains at multiple depths in the emulsion layer. This information is used to construct an object called a *microtrack* which contains an information on the position and angle of the passing particle track. A microtrack is a basic building block of all tracks reconstructed in the ECC. Microtracks are found and reconstructed by the automated scanning system [35].

⁸As opposed to just a point position.

about 20 % if track passes through the entire ECC brick and gets worse as particle passes through less lead plates. More information can be found in Ref. [37].

3.3.2 OPERA apparatus

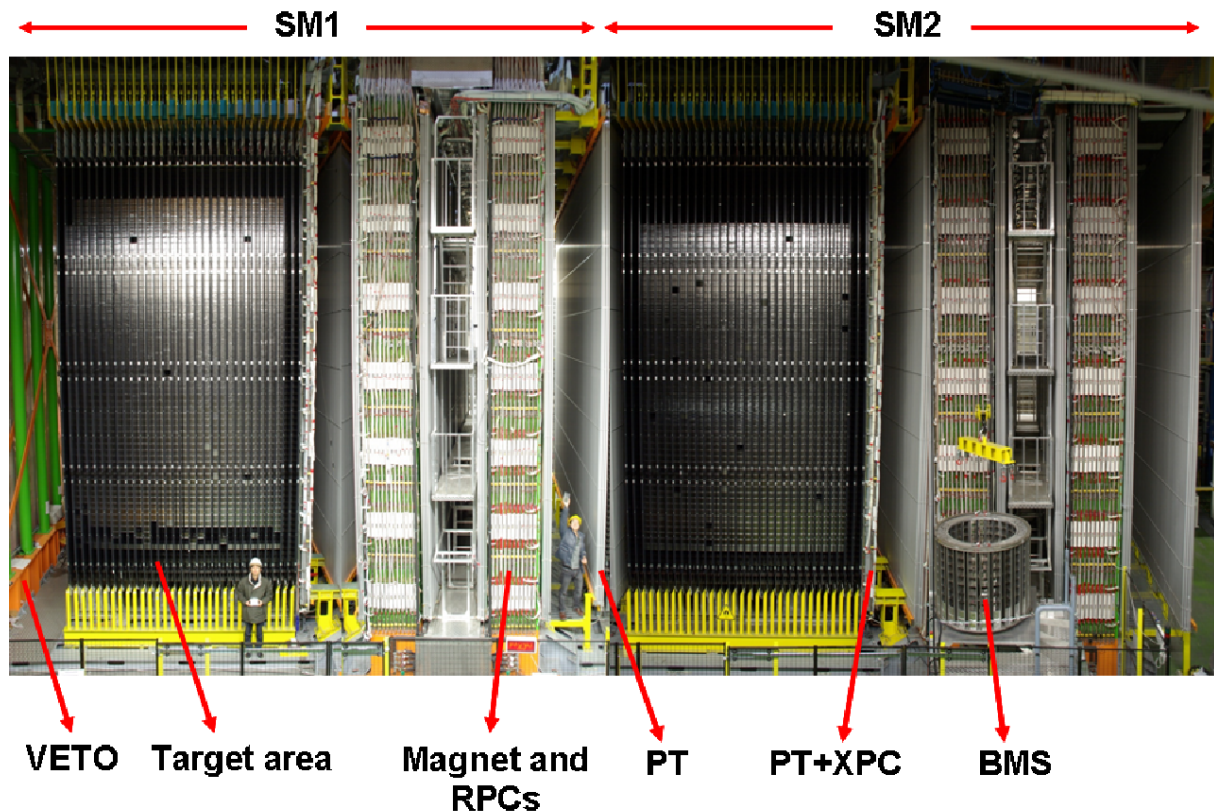


Figure 3.6: A photograph of the OPERA detector showing the main components. The beam is entering the detector on the left side of the photograph.

The OPERA apparatus is made up of two identical *supermodules*, each consisting of the target area and the magnetic spectrometer (see Figure 3.6). A *VETO* plane is located upstream of the two supermodules - a glass RPC detector used to veto the external muons¹⁰ entering the detector from the beam direction.

A target area consists of ECC brick walls interleaved with *target tracker* (TT) walls. Bricks can be extracted and inserted into the target using an automated Brick Manipulator System (BMS)¹¹.

Each TT plane consists of 256 vertical and 256 horizontal plastic scintillator strips.

¹⁰Muons produced by the CNGS neutrino interactions in the material upstream of the OPERA detector.

¹¹BMS was also used at the construction phase to insert all 150000 bricks, one by one, into the target.

Each strip is 6.86 m long, 10.8 mm wide and is read out on both sides using wavelength shifting fibres connected to multi-anode photomultipliers (see Figure 3.7). The primary purpose of target trackers is to predict in which ECC brick neutrino interaction took place by measuring tracks of the resulting muon and/or hadrons. They also allow for the limited calorimetry of neutrino events by measuring the energy deposition of charged particles in scintillator strips.

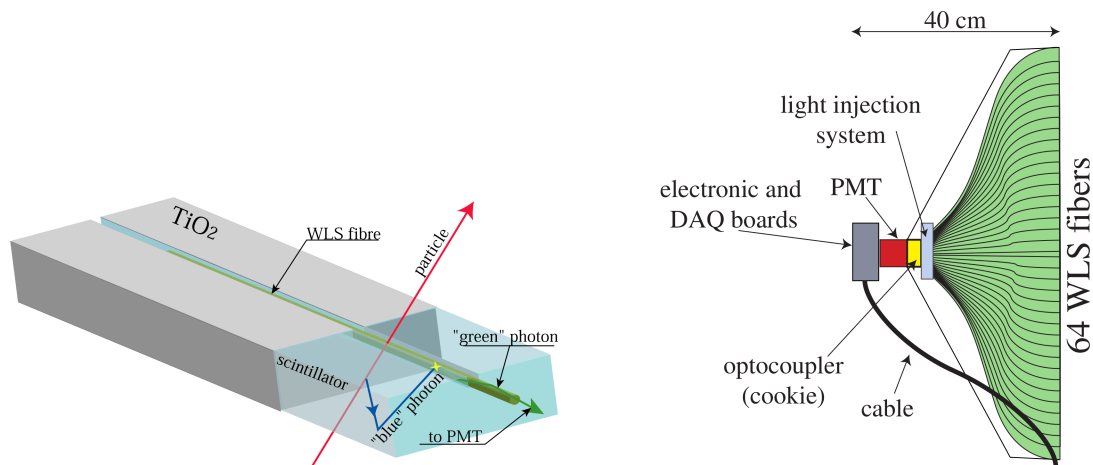


Figure 3.7: Left - schematic view of the Target Tracker scintillator strip with a wavelength-shifting fibre. Right - schematic view of the readout system using 64 channel photomultiplier module. Figure taken from [38].

A magnetic spectrometer [39, 40], shown in Figure 3.8, consists of a normal-conducting magnet, resistive plate chamber (RPC) trackers and drift tube precision trackers (PT). The average magnetic field in the iron of the magnet is 1.53 T, with non-uniformities along its height not exceeding 3%. Charged particles are bent in the horizontal plane. Each of the two arms of the magnet consists of 22 RPC planes interleaved with 24 iron slabs. RPC planes are used to reconstruct ionizing particle tracks¹² inside the magnet and to provide the trigger to PT drift tubes. Additionally, there are two RPC planes placed upstream of the magnet with tilted readout strips, called the XPC, which are used to remove ambiguities in multi-particle events.

Each one of RPC planes consists of 21 resistive plate chambers arranged in 7 rows and 3 columns. Readout is done on conducting strips which are arranged horizontally on one side and vertically on the other side of the RPC plane¹³ (see Figure 3.9). The vertical

¹²Especially those that stop in the magnet and are therefore out of reach of PT detectors.

¹³Readout strips run through the whole height/width of the RPC plane.

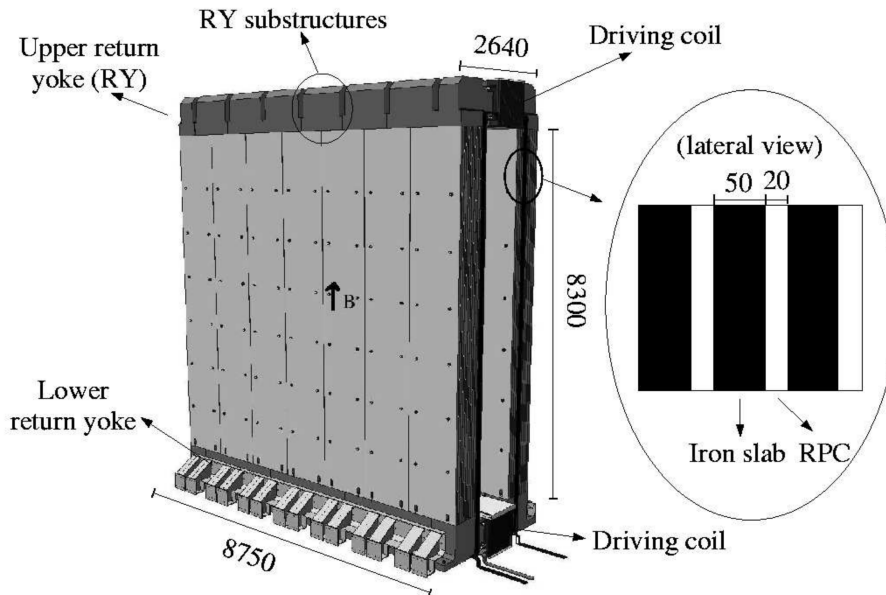


Figure 3.8: A 3-D view of the OPERA spectrometer. Figure taken from [38].

strips are 8 m long with a pitch of 2.6 cm, and the horizontal strips are 8.7 m long with a pitch of 3.5 cm.

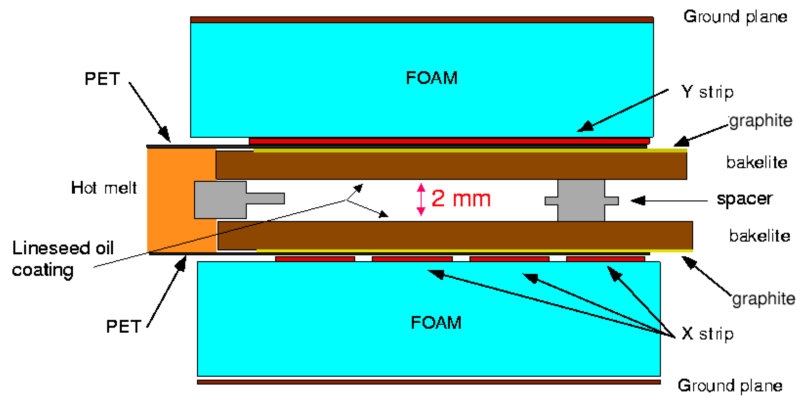


Figure 3.9: A horizontal cross section of a part of the OPERA RPC plane. Figure taken from [38].

The precision tracker drift tubes are designed to accurately measure the position of charged particles in the bending plane of the magnet. They are arranged in 6 planes per spectrometer, two planes upstream of the magnet, two planes between arms of the magnet and two planes downstream of the magnet (see Figure 3.10). A single tube is 8 m long

vertical cylinder, with an outer radius of 38 mm and a wall thickness of 0.85 mm. A sense wire of 45 μm diameter is suspended along the centre of the cylinder. A spatial resolution of a single PT tube is measured to be less than 300 μm . There are a total of 10000 PT tubes in the OPERA apparatus.

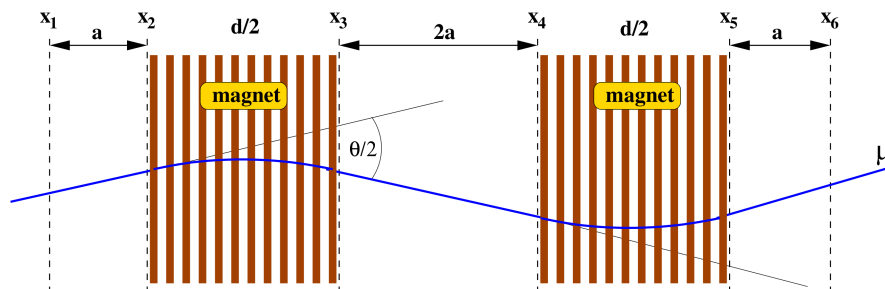


Figure 3.10: A schematic horizontal plane cross section view of PT plane positions (dashed lines) wrt. the two magnet arms in the spectrometer. The blue line depicts a particle trajectory through the spectrometer and $\theta/2$ is the bending angle of the track as it passes the magnetic field. Figure taken from [38].

The sensitive parts of the OPERA detector other than ECC bricks (i.e. VETO, TTs, RPCs and PTs) are together called the OPERA Electronic Detectors (ED).

3.3.3 Event reconstruction

The OPERA event reconstruction starts with the event trigger by the electronic detector system (see Figure 3.11). Each triggered event is analysed semi-offline¹⁴ by the Brick Finding algorithm which outputs a ranked¹⁵ list of three bricks in which neutrino interaction was most likely to occur. The most probable brick, i.e. the one which is ranked first by the interaction probability, is then extracted from the target using the BMS.

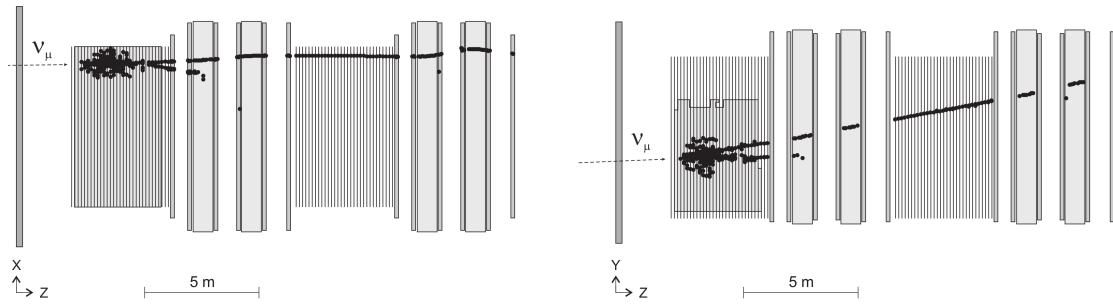
The CS of the extracted brick are marked by x-ray for alignment purposes¹⁶ and developed in the underground laboratory¹⁷. The ECC brick is placed in the shielded underground storage area to await for the results of the CS analysis. The developed CS is scanned using automatic scanning microscopes in a dedicated laboratory located in the surface part of the LNGS.

¹⁴Usually once per day.

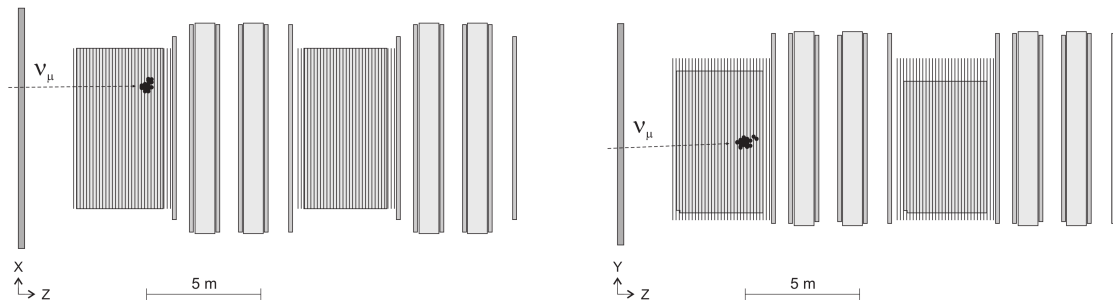
¹⁵Ranked by the probability that neutrino interaction occurred in the brick, given ED data.

¹⁶The x-ray mark aligns the two Changeable Sheet and the adjacent emulsion sheet in the brick.

¹⁷It is not taken undeveloped to the surface to avoid contamination by cosmic muon tracks and environmental surface radioactivity.



(a) Event display of a CC event



(b) Event display of a NC event

Figure 3.11: OPERA electronic detectors event display of a beam CC interaction of ν_μ and a NC neutrino interaction. These events were confirmed to be CC and NC in the subsequent analysis of the corresponding ECC brick (see Figure 3.13). Figures on the left are a top view of the detector, while the ones on the right are a side view. Neutrino beam is incoming from the left. Each dot represents a single sensor response to passage of a charged particle (a *digit*) - scintillator strips in the target area, RPC readout strips inside the magnet arms and PT tubes around the magnet arms. There are no PT digits visible in the side view since those sensors are sensitive only to the particle positions in the horizontal plane. A slight tilt upwards visible in the side view is a result of a neutrino beam tilt. Figures are taken from [41].

If particle tracks compatible to the ones predicted by the ED are found in two CS emulsion plates, the corresponding ECC brick is scheduled for development. Otherwise, new CS doublet is attached to the brick and the brick is inserted back into the target, and the procedure is repeated for the second brick in the ranking of the Brick Finder.

The brick scheduled for development is then tagged by x-ray¹⁸ and taken to the surface laboratory for further processing.

First, the brick is exposed to cosmic muon flux to obtain straight tracks for the inter-emulsion alignment. This is done in the dedicated area called the *cosmic pit*, a 3 m diameter cylinder at depth of 8.25 m underground, accessible from a basement of a building in the surface part of LNGS laboratory. A brick is placed in a special shielded area within the cosmic pit, called a *cosmic bench*, shielded by 40 cm thick iron slab from above and with iron and plastic slabs on the sides. The shielding filters low energy cosmic muons and soft radiation due to electron and neutron scattering. The brick is left in the cosmic bench for about 12 h which in these conditions results in about 1 muon track per mm² of the emulsion.

After the cosmic exposure, bricks are disassembled and the emulsion sheets are developed in the dedicated laboratory. They are then packaged and sent to the scanning laboratories in Europe and Japan.

ECC event reconstruction

The reconstruction procedure in the scanning laboratories starts by following the tracks found in the CS doublet upstream through the brick until they stop¹⁹. This procedure is called *scanback*.

Then a *volume scan* is performed around the stopping point. This is a procedure in which a 1 cm² area is scanned in 5 emulsion plates upstream and 5 emulsion plates downstream of a track stopping point. The volume is skewed to account for the vertical CNGS beam tilt.

Microtracks found in the volume scan are then combined into particle tracks, in a

¹⁸The ECC brick, unlike the CS doublet, cannot be aligned by x-ray marking because lead plates are opaque for x-rays. Nevertheless, a lateral mark is made by x-ray on the side of the brick which is used to keep track of the original ordering of emulsion plates within the brick.

¹⁹If none of these tracks have a stopping point inside the brick, the analysis of the ECC stops here. The interaction has most likely occurred in the adjacent brick upstream.

procedure called *tracking*. The inter-emulsion alignment using cosmic muon tracks is performed in this phase.

Particle tracks are then combined into vertices - a procedure called *vertexing* - and all tracks passing through the volume are discarded (see Figure 3.12).

In the end, all tracks connected to the vertex are followed downstream in the brick to search for re-interactions and decays in a procedure called *decay search*.

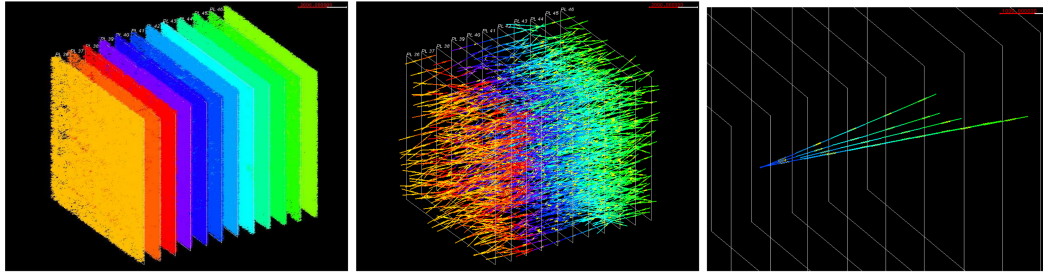
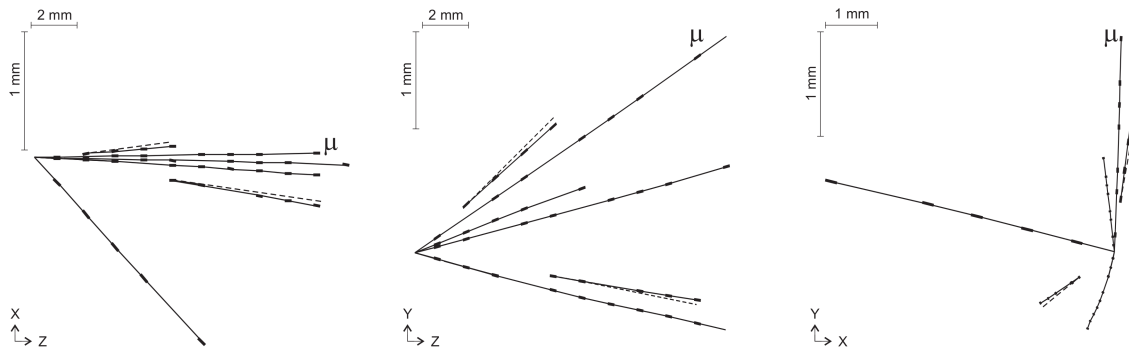


Figure 3.12: Different steps in the emulsion event reconstruction procedure. Left-most figure shows a result of a volume scan around the stopping point of a scanback track. Central figure shows a result of tracking applied to the volume scan. Only microtracks which are parts of reconstructed tracks are retained. Rightmost figure shows a result of the vertexing procedure applied to reconstructed tracks. All passing-through tracks are discarded and only tracks attached to a vertex remain. In all figures, the beam is incident from the left side. Figure is taken from [38].

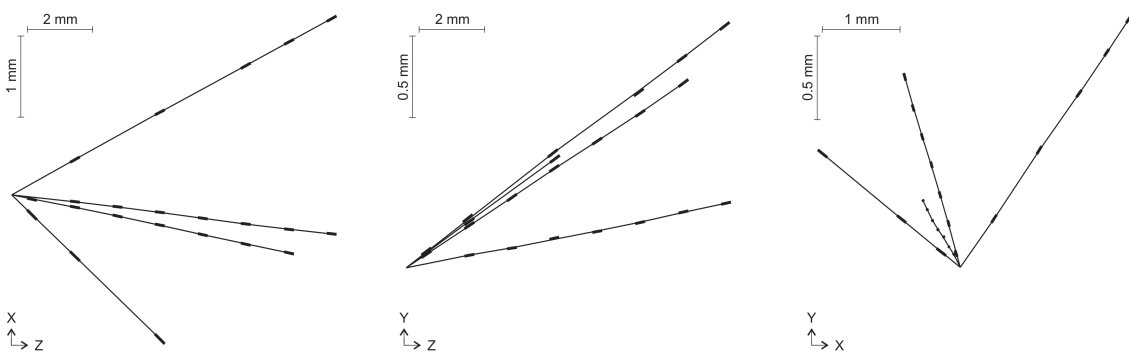
If a scanned event has an interesting topology²⁰, i.e. is a candidate for a tau decay event, additional analysis is performed. Bricks located downstream of the interaction brick are extracted from the OPERA target in order to follow all particle tracks through the emulsion until they either stop or exit the target areas. This allows for an improved particle identification and measurement of its energy and momentum.

Selection cuts are then performed on a fully reconstructed event, and if it passes all of the cuts, it is deemed a tau candidate event - an interaction of tau neutrino inside the OPERA target. See the Appendix A for description of selection cuts.

²⁰And is then called an *interesting event*.



(a) ECC reconstruction of a CC event. The identified muon track is compatible with the one reconstructed by the electronic detectors.



(b) ECC reconstruction of a NC event.

Figure 3.13: Emulsion reconstruction of events which triggered the detector in Figure 3.11. Leftmost figures show a top view, central ones a side view, and rightmost ones a front view of the reconstructed event. Figures are taken from [41].

3.4 Physics results

3.4.1 Discovery of $\nu_\mu \rightarrow \nu_\tau$ appearance

The OPERA experiment has successfully reached its physics goal of observing the $\nu_\mu \rightarrow \nu_\tau$ neutrino oscillations in the appearance mode. After a full data sample obtained in the 2008 - 2012 run has been analysed, five tau neutrino candidate events have been found. A detailed description of each candidate event can be found in Refs. [14, 36, 42–44].

To obtain the significance of tau neutrino appearance measurement, one must evaluate the expected number of background events, i.e. events which are not a result of tau neutrino interactions but are nevertheless reconstructed as tau candidates in OPERA.

Main source of background in OPERA are decays of charmed particles (D^+ , D^0 , D_s^+

Table 3.3: Distribution of fully reconstructed OPERA neutrino events over the years in which the interaction occurred. A total number of protons-on-target achieved at the CNGS facility in each year is shown for comparison with the OPERA event rate. 0μ events are those in which no muon has been identified while 1μ events are those in which one μ has been found. A cut on muon momentum reconstructed in the spectrometer has been applied to 1μ events to reduce background - high momentum muons are less likely to be a product of tau decay due to the energy carried away by two neutrinos in tau decay process $\nu_\tau^- \rightarrow \mu^- + \bar{\nu}_\mu + \nu_\tau$. Table is taken from [14].

	2008	2009	2010	2011	2012	Total
POT (10^{19})	1.74	3.53	4.09	4.75	3.86	17.97
0μ events	149	253	268	270	204	1144
1μ events ($p_\mu < 15 \text{ GeV}/c$)	542	1020	968	966	768	4264
Total events	691	1273	1236	1236	972	5408
Detected ν_τ candidates		1		1	3	5

and Λ_c), produced as a part of resulting hadronic system in ν_μ CC interactions²¹. Masses and lifetimes of these particles, and hence their flight length, is similar to that of tau lepton. Therefore, they can mimic the characteristic kink topology of the tau decay. This background is strongly rejected by identification of primary muon produced in ν_μ CC interactions. For detailed description of charmed particle observation in the OPERA experiment see Ref. [45].

Another source of background are reinteractions of secondary hadrons in the lead plate downstream of an interaction vertex. This can cause a kink topology and result in misidentification of a reinteracting hadron track as tau lepton decaying into hadron. This background is suppressed (*i*) by using the fact that lepton and hadron momenta should be back-to-back in beam-transverse plane in CC neutrino interactions and (*ii*) searching for nuclear fragments characteristic of hadronic interactions around the tau decay point. This background is relevant only for hadronic tau decay modes.

Large angle muon scattering is a source of background in which a primary muon scatters by a large angle in a lead plate downstream of neutrino interaction vertex, mimicking $\tau^- \rightarrow \mu^- + \bar{\nu}_\mu + \nu_\tau$ decay topology. A contribution of this background source has been re-evaluated since the experiment proposal and has been found to be negligible [46]. It is nevertheless kept in the analysis for historical reasons.

²¹NC interactions can produce these charmed particles as well, but at a much lower rate and only in particle-antiparticle pairs.

The detailed description of OPERA background sources and methods to reject them can be found in [43, 47]. The expected number of background events together with the expected number of signal events and observed events is shown in Table 3.4.

Table 3.4: Number of expected background events, expected signal events and observed events in each of the four tau decay channels. Table is taken from [14].

Channel	Expected background			Total	Expected signal	Observed
	Charm	Had. reinterac.	Large μ scat.			
$\tau \rightarrow 1h$	0.017 ± 0.003	0.022 ± 0.006		0.04 ± 0.01	0.52 ± 0.10	3
$\tau \rightarrow 3h$	0.17 ± 0.03	0.003 ± 0.001		0.17 ± 0.03	0.73 ± 0.14	1
$\tau \rightarrow \mu$	0.004 ± 0.001		0.0002 ± 0.0001	0.004 ± 0.001	0.61 ± 0.12	1
$\tau \rightarrow e$	0.03 ± 0.01			0.03 ± 0.01	0.78 ± 0.16	0
Total	0.22 ± 0.04	0.02 ± 0.01	0.0002 ± 0.0001	0.25 ± 0.05	2.64 ± 0.53	5

Given the number of expected background events and the number of observed tau candidate events, the significance of the OPERA ν_τ observation is 5.1σ , i.e. the probability to observe the five tau candidate events from background effects alone is $3.4 \cdot 10^{-7}$. In particle physics community, any observation with significance of more than 5σ is considered a *discovery*.

3.4.2 Constraints on neutrino oscillation parameters

Constraints on $|\Delta m_{32}^2|$

Given the fact that OPERA has observed 5 tau neutrino parameters with the expected background of (0.25 ± 0.05) , it is possible to estimate neutrino oscillation parameters in $(|\Delta m_{32}^2| - \sin^2 \theta_{23})$ plane²². This has been done using profile likelihood, Feldman-Cousins and Bayesian statistical methods. Assuming the full mixing, i.e. $\sin^2 \theta_{23} = 0.5$, all three methods yield $[2.0, 5.0] \cdot 10^{-3} \text{eV}^2$ 90% confidence interval for $|\Delta m_{32}^2|$ [14].

At the very end of writing this text, a further analysis of the tau appearance channel has been published by OPERA [15], in which the number of tau candidate events in the analysed sample was increased by improving the selection using multivariate analysis methods. This additionally tightened the $|\Delta m_{32}^2|$ confidence interval and increased the significance of the observation.

²²The expected number of observed τ events is roughly proportional to $(\Delta m_{32}^2)^2$, see the equation (3.1).

An additional constraint on $|\Delta m_{32}^2|$ has been made by the analysis performed in this work, which is dominated by the $\nu_\mu \rightarrow \nu_\mu$ disappearance channel.

Constraints on $\sin^2 \theta_{13}$

Additionally, an analysis was performed on the $\nu_\mu \rightarrow \nu_e$ appearance in the OPERA experiment [8, 9], a channel which is sensitive to oscillation parameters in the $(\sin^2 \theta_{13} - \Delta m_{32}^2)$ plane. The electron neutrino appearance signal in OPERA is heavily eclipsed by large background coming from prompt ν_e and $\bar{\nu}_e$ CNGS flux components. The no-oscillation hypothesis predicts $33.1 \pm 0.7(\text{stat}) \pm 3.1(\text{syst})$ fully reconstructed $\nu_e + \bar{\nu}_e$ candidate events, while in the standard oscillation hypothesis predicts $34.3 \pm 0.5(\text{stat}) \pm 3.4(\text{syst})$ fully reconstructed $\nu_e + \bar{\nu}_e$ candidate events. The number of observed candidate events in the total OPERA data sample is 35, consistent with both predictions. A shape analysis of the oscillation probability wrt. neutrino energy has been performed (see Figure 3.14), constraining the value of $\sin^2 \theta_{13} < 0.12$ at 90% C.L. upper limit with all other oscillation parameters fixed.

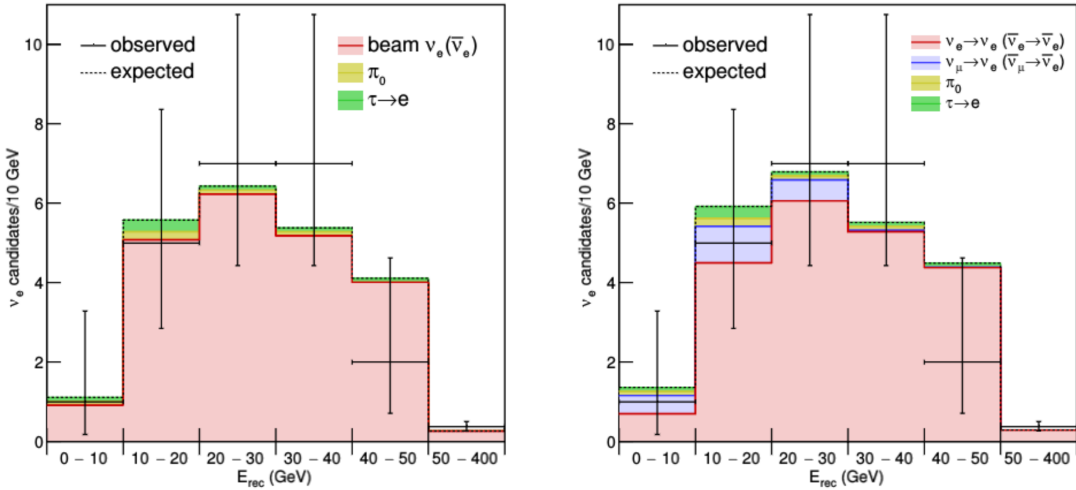


Figure 3.14: Expected and observed number of $\nu_e + \bar{\nu}_e$ fully reconstructed events vs. the reconstructed neutrino energy for: (left) no oscillation hypothesis, (right) standard 3 generation neutrino oscillations. Figure taken from [9].

Chapter 4

Monte Carlo simulation of the OPERA experiment

This chapter describes the methods used to obtain the Monte Carlo event sample used to in the analysis performed in the Chapter 5. It starts with the formalism used to calculate the expected interaction rates in OPERA, and the way neutrino oscillation effects are included in the analysis. It continues with the description of the OPERA geometry and the materials in which neutrino interactions are simulated. Then the OPERA Monte Carlo software chain is described, and the contributions and modifications made by the author are highlighted. This software is used to make a dedicated MC simulation for the purpose of this work, which is described in the last section of this chapter.

4.1 Interaction rates

An interaction rate of a neutrino flux on a target object is defined as the number of neutrino interactions per unit time inside the target, formally:

$$R_{\text{int}}(t) \equiv \frac{dN_{\text{int}}(t)}{dt} , \quad (4.1)$$

where R_{int} is the interaction rate and N_{int} is a number of interactions as a function of time.

Neutrino flux is defined as the number of neutrinos passing through a unit area in unit

time, defined by the equation:

$$\frac{dL(t)}{dE} = \frac{1}{A} \frac{d^2 N_\nu(t)}{dt dE} , \quad (4.2)$$

where $N_\nu(t)$ is a number of neutrinos passing perpendicularly through arbitrary flat surface of area A . This simplified definition of a flux can be used because the CNGS beam is spatially homogeneous with constant direction within the LNGS experimental hall, due to the distance between LNGS and CERN.

The interaction rate is connected to the flux via the neutrino cross-section σ , using the formula:

$$R(t) = \int_0^\infty \frac{dL}{dE} \sigma(E) dE , \quad (4.3)$$

where $\sigma(E)$ is a total neutrino cross section of the target, as a function of neutrino energy E .

The flux of CNGS neutrinos at the OPERA detector site is given as a function of protons-on-target (p.o.t). This implicitly assumes that the energy spectrum of the beam is the same in every proton extraction¹. The quantity provided by the CNGS team is therefore:

$$L_{\text{CNGS}} = \frac{d^3 N_\nu}{dE dA C_{\text{pot}} dN_{\text{pot}}} , \quad (4.4)$$

where N_{pot} is the number of protons-on-target and $C_{\text{pot}} = 10^{-19}$ is just a numerical constant.

One may define p.o.t interaction rate as:

$$R_{\text{pot}} \equiv \frac{dN_\nu}{dN_{\text{pot}}} , \quad (4.5)$$

which is easily connected to the proper interaction rate:

$$R_{\text{pot}} \equiv \frac{dN_\nu}{dN_{\text{pot}}} = \frac{dN_\nu}{N'_{\text{pot}}(t) dt} = \frac{1}{N'_{\text{pot}}(t)} R_{\text{int}} , \quad (4.6)$$

where $N'_{\text{pot}}(t)$ is a time derivative of the number of p.o.t. and is always positive since number of p.o.t. can only grow in time.

¹Or can be possibly thought of as the average spectrum of a large number of extractions.

Combining the above equations, one obtains the formula for the p.o.t. interaction rate:

$$R_{\text{pot}} = C_{\text{pot}} \int_0^{\infty} L_{\text{CNGS}}(E) \sigma(E) dE \quad (4.7)$$

and the expected number of interactions produced by ΔN_{pot} is then

$$N_{\text{int}} = \Delta N_{\text{pot}} R_{\text{pot}} . \quad (4.8)$$

Neutrino interaction cross-section of a composite material

Neutrino cross-sections provided by theory are defined for a single isotope of a single element. In principle, one could calculate the total cross-section of a bulk of material by summing up total cross-sections of every single atom present in the material:

$$\sigma_{\text{TOT}}(E) = \sum_{i=1}^N \sigma_A(E; Z_i, A_i) , \quad (4.9)$$

where $\sigma_A(E; Z, A)$ is the neutrino cross-section of a single atom of an isotope with atomic number Z and mass number A , and the sum goes over all the N atoms present in the bulk material.

In practice, this is not very useful, since parts of the detector are defined by their chemical composition and macroscopic quantities.

For a target composed of different isotopes of the same element, one may define an average atomic cross section as:

$$\bar{\sigma}_A(E; Z) = \sum_{i=1}^M \sigma_N(E; Z, A_i) \eta(Z, A_i) , \quad (4.10)$$

where $\eta(Z, A_i)$ is a molar fraction of an isotope i . The total cross-section of the target is then

$$\sigma_{\text{TOT}}(E) = N_N \cdot \bar{\sigma}_A(E; Z) = n N_A \cdot \bar{\sigma}_A(E; Z) , \quad (4.11)$$

where N_N is a number of atoms present in the target, n is the amount of substance (number of moles) of the target and N_A is Avogadro constant.

If target is composed of a natural mixture of isotopes, one can find the amount of sub-

stance using the standard atomic weight A_r obtained from the periodic table of elements:

$$n = \frac{m}{A_r M_c} , \quad (4.12)$$

where m is a mass of the target and $M_c = 1 \text{ g/mol}$ is a unit constant. Putting it all together, one finally obtains a formula for the total neutrino cross-section of a target of mass m composed of a single chemical element:

$$\sigma_{\text{TOT}}(E) = m \frac{N_A}{A_r M_c} \bar{\sigma}_E(Z) . \quad (4.13)$$

This cross-section can then be plugged into equation (4.7) to obtain the number of expected interactions per p.o.t in the target of mass m composed of a single chemical element²

$$R_{\text{pot}}^{\text{TOT}}(Z) = m \frac{N_A C_{\text{pot}}}{A_r M_c} \int_0^\infty L_{\text{CNGS}}(E) \bar{\sigma}_E(E; Z) dE . \quad (4.14)$$

4.2 Simulating the effects of neutrino oscillations

When producing the MC simulation, no assumptions are made on the neutrino oscillation parameters³. Instead, a set of *unoscillated* events is produced, which is then re-weighted in the analysis phase according to the oscillation probability.

The flavour composition of the CNGS beam at its origin is dominated by ν_μ , with a small addition of $\bar{\nu}_\mu$, ν_e and $\bar{\nu}_e$ (see Chapter 3.1). The total neutrino flux remains unchanged in its propagation through the earth to the OPERA detector, while its flavour composition changes due to neutrino oscillations. To account for the flavour change, the total flux is divided into flux components. Flux components are divided into two classes - prompt flux components and appearance flux components.

Prompt flux components are the ones reported by the CNGS, shown in Figure 3.2. These components are used to generate both NC and CC neutrino interactions. Neutrino events produced by CC interactions are re-weighted in the analysis according to the survival probability for the respective neutrino flavour, while those produced by NC

²Similar formula can be obtained for an arbitrary mixture of materials.

³Except for the rough estimate of the number of events that need to be produced for each channel.

interactions are not re-weighted for the oscillation effects.

Appearance flux components are used to simulate appearance effects for each of the four prompt flux components. Two appearance components are required for each prompt component, since a neutrino of a definite flavour may oscillate to other two flavours⁴. An appearance flux component is constructed by taking the energy spectrum of the corresponding prompt component and changing the flavour of neutrino. Appearance flux components are used to produce only CC interactions, to avoid double counting of NC events. These CC interactions are then re-weighted by oscillation probability in the analysis.

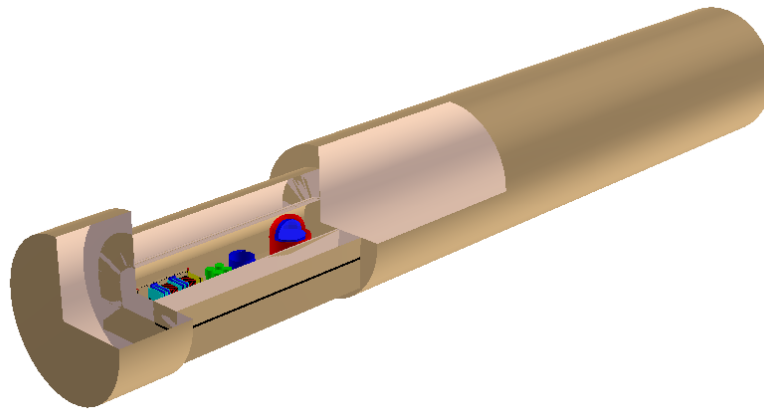
4.3 OPERA detector geometry

4.3.1 Implementation in *ROOT*

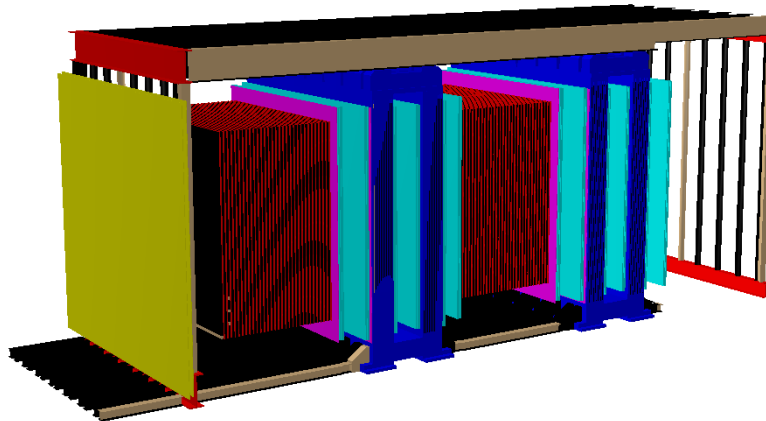
OPERA detector geometry is implemented using ROOT's *TGeometry* class as a base class to OPERA-specific *OpGeom* class. Three different modes are available when building OPERA geometry - FULL, OPERA, and BRICK (see Figure 4.1). The OPERA geometry mode consists of the OPERA detector and the supporting structure, the BRICK geometry is just a single ECC brick and the FULL mode consists of the entire Hall C at LNGS, including a simple model of Borexino detector and its infrastructure, complete OPERA apparatus and the rock surrounding the hall.

Dedicated MC sample created for this work uses the FULL geometry. This allows not only simulation of the recorded OPERA events coming from neutrino interactions inside the apparatus, but also includes *external* events - neutrino interactions occurring outside of the detector, but whose products reach and are recorded by the detector. Even though most of the external events are filtered out by the *OpRec* classification, some remain in the data set and should be simulated.

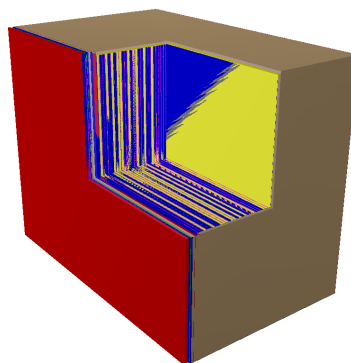
⁴For example, prompt ν_μ may oscillate to ν_e and ν_τ .



(a) FULL geometry (clipped)



(b) OPERA geometry



(c) BRICK geometry (clipped)

Figure 4.1: Geometry modes of OPERA

4.3.2 Classification of materials

The probability of neutrino interacting and the composition of interaction products depends on the material neutrino is interacting with. In the first order approximation, total neutrino cross-section depends only on the mass of the target, so the probability of it interacting in a certain point is proportional to density of the material at that point. The most significant correction to this simple proportionality rule is due to non-isoscalarity of the target nucleus, which is important only for heavy nuclei. The composition of interaction products, i.e. the particles outgoing from the interaction vertex, depends on the nuclear species as well.

Because of these considerations, the materials in the dedicated MC simulation has been divided in three categories - LEAD, IRON and ISO (isoscalar material).

Iron and lead are assumed to have a natural isotope composition. All the other materials are members of the ISO category, which means that they are isoscalar enough that non-isoscalar effects are negligible. The isoscalar matter is modelled as matter composed of nuclei which have an atomic number $Z_{\text{ISO}} = 1/2$ and a mass number $A_{\text{ISO}} = 1$. Atomic neutrino cross section is taken as $1/12$ of a cross-section of ^{12}C :

$$\sigma_{\text{ISO}} = \frac{\sigma_{^{12}\text{C}}}{12} . \quad (4.15)$$

Natural isotope compositions of lead and iron are shown in table (4.1). These compositions are used throughout the simulation.

Table 4.1: Natural isotope compositions of lead and iron

Lead $A_r = 207.2$		Iron $A_r = 55.485$	
^{204}Pb	1.4%	^{54}Fe	5.845%
^{206}Pb	24.1%	^{56}Fe	91.754%
^{207}Pb	22.1%	^{57}Fe	2.119%
^{208}Pb	52.4%	^{58}Fe	0.282%

4.4 OPERA MC chain

The OPERA Monte Carlo production chain is a set of programs within the *OpRelease* software framework which perform different steps of the simulation. The overview of the chain is shown in Figure 4.2.

The chain starts with the simulation of neutrino interactions with atoms, which are then stored into files called *beamfiles*. Beamfiles are then used as an input to *OpSim* package which simulates the propagation of particles through the detector. *Genie* generator was used to generate the beamfiles and the neutrino interaction cross-sections. Cross-sections are an input to *OpSim*, which uses them to calculate the positions of interaction vertices according to interaction probabilities of different materials present in OPERA.

Next in the chain is *OpDigit*, which simulates the response of sensors within OPERA, using the output of *OpSim* to obtain the points at which particles cross the sensors. The output of this package is in the same data format as the recorded data.

OpRec reconstructs the events using the data obtained from OPERA electronic detectors. It can be run both on the simulation or on the real data, and the results can be directly compared.

OpEmuRec package simulates the reconstruction of neutrino interactions in the OPERA ECC brick, and its output can be compared with the real reconstructed events.

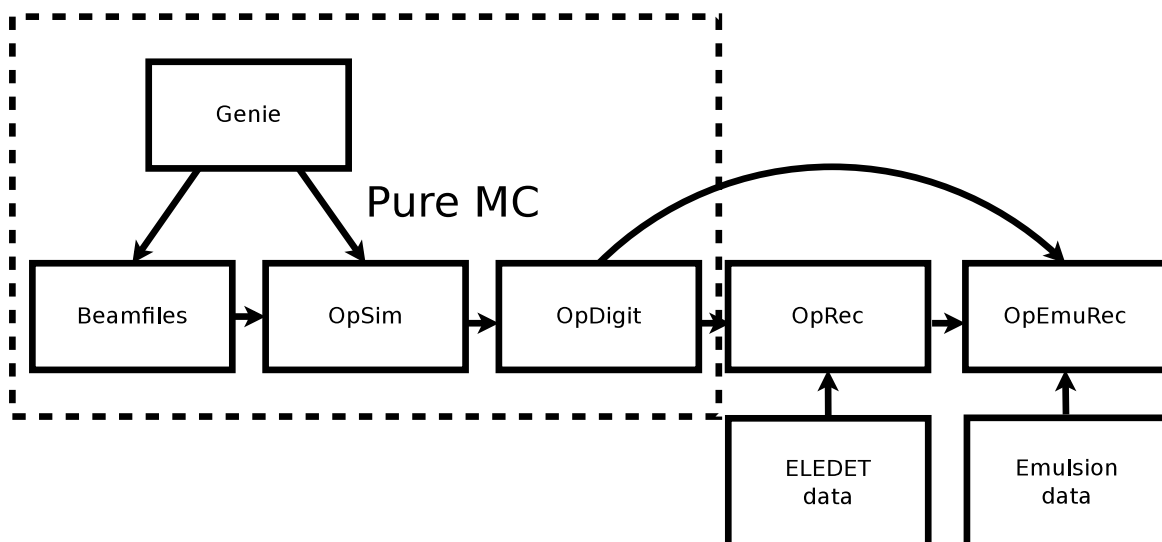


Figure 4.2: OPERA MC chain.

4.4.1 Beamfiles

Beamfiles are a set of simulated primary interaction vertices, containing all the information on incoming and outgoing particles and momenta. For the purpose of this work, a dedicated set of beamfiles using Genie 2.8.6 [48] has been produced to achieve a better accuracy of the simulation.

Beamfiles have been produced for all four flavour components of the CNGS neutrino beam, using the energy spectrum provided by the CNGS team [16]. All the particle momenta have been rotated to account for the tilt of the CNGS beam.

Rotation of the beam

Due to the curvature of the Earth, CNGS neutrino beam is tilted downwards at the source and tilted upwards at the detector site by the angle γ . Using geometry of the Earth, one can calculate the expected beam tilt.

There is also a horizontal tilt β , which is an artefact of the choice of the OPERA coordinate system. Since the coordinate system was designed in such a way that $y - z$ plane contains both LNGS and CERN, angle β is expected to be small.

Formally, beam unit vector is defined as:

$$\hat{r}_b = \frac{\hat{x} \tan \beta + \hat{y} \tan \gamma + \hat{z}}{\sqrt{1 + \tan^2 \beta + \tan^2 \gamma}} . \quad (4.16)$$

Knowing the OPERA baseline and the radius of the Earth, one can find the vertical tilt angle γ to be:

$$\gamma = \arcsin \frac{d}{2R} , \quad (4.17)$$

where d is the baseline and R is the radius of the Earth. At the OPERA baseline of 732 km this yields:

$$\gamma_{\text{calc}} = 57.4 \text{ mrad} = 3.3^\circ . \quad (4.18)$$

The value measured using the average tilt of muons produced by CC interactions in the OPERA detector is:

$$\gamma_{\text{meas}} = 58.06 \text{ mrad} . \quad (4.19)$$

This value is used in the remainder of the analysis.

Horizontal angle is measured to be

$$\beta_{\text{meas}} = -6.78 \text{ mrad} , \quad (4.20)$$

small as expected.

The default beam direction of the *Genie* generator is in the positive z axis, i.e

$$\hat{r}_G = \hat{z} . \quad (4.21)$$

In order to take into account the beam rotation, one must rotate all the particle momenta in such a way that the z axis unit vector in the *Genie* output transforms into the beam unit vector (4.16). This condition can be written as:

$$\hat{r}_b = G \hat{r}_G = G \hat{z} , \quad (4.22)$$

where G is a proper⁵ rotation operator. Rotation satisfying the equation (4.22) is not unique, because one can always add an additional rotation around the z axis to the right side while keeping the equation valid. Since the CNGS beam is homogeneous⁶ at the OPERA site, we can consider this as an extra free parameter and choose it arbitrarily.

In this MC production the 3-dimensional space rotation is parametrized using the rotational axis (represented by a vector) and the rotational angle around that axis. The vector defining the rotational axis is chosen to be:

$$\vec{r}_r = \hat{r}_G \times \hat{r}_b , \quad (4.23)$$

and the angle of rotation⁷

$$\theta_r = \arcsin |\vec{r}_r| . \quad (4.24)$$

This vector and angle pair is then used to construct the rotation matrix G using *ROOT*'s

⁵When dealing with weak interactions, one must always be careful not to include reflections, due to the P violation. In this case, though, it doesn't really matter.

⁶This is due to the 732 km distance between CERN and LNGS.

⁷This formula works only if the angle between \hat{r}_b and \hat{r}_G is less than $\pi/2$, which we know it is.

TRotation class, which is then applied to all particle momenta in *Genie*'s output.

4.4.2 OpSim

OpSim package takes the beamfiles as an input, selects the coordinates of a primary neutrino vertex, propagates all the particles of the final state of neutrino interaction through the detector and calculates the positions of *hits*. *Hits* are points at which particles enter and exit sensitive areas of the detector, i.e. TT's, RPC's, PT's and emulsions, which are then used to simulate the sensor response in *OpDigit* step.

Propagation of particles and calculation of hits is done using *ROOT VMC* [49] as a frontend and *Geant3* [50] as a backend.

OpSim was modified by the author for the purposes of this work, primarily to add the ability to randomly select the neutrino vertex position according to the interaction probability in different materials.

Selecting the primary vertex position

Atomic neutrino cross-sections as a function of energy for all relevant isotopes and for all four beam components as a function of energy are calculated using *Genie*.

Using the formula (4.14), isotope compositions in Table 4.1 and using *Genie* cross-sections, one obtains the unoscillated p.o.t. interaction rate per unit mass for the three materials for each of the four beam components, see Table 4.2.

Table 4.2: Mass interaction rates for simulated materials, no neutrino oscillations applied.

Material	A_r	$\frac{R_{\text{pot}}^{\text{TOT}}}{m} / (\text{ton} \cdot 10^{19} \text{pot})$			
		ν_μ	$\bar{\nu}_\mu$	ν_e	$\bar{\nu}_e$
Lead	207.2	$8.04 \cdot 10^{-1}$	$1.67 \cdot 10^{-2}$	$7.24 \cdot 10^{-3}$	$4.22 \cdot 10^{-4}$
Iron	55.485	$7.78 \cdot 10^{-1}$	$1.73 \cdot 10^{-2}$	$7.00 \cdot 10^{-3}$	$4.36 \cdot 10^{-4}$
ISO	1.0	$7.65 \cdot 10^{-1}$	$1.76 \cdot 10^{-2}$	$6.89 \cdot 10^{-3}$	$4.43 \cdot 10^{-4}$

Table 4.2 illustrates how many neutrino interactions one might expect per tonne of target in the CNGS beam for 10^{19} protons of target (which corresponds to about 1.5 months of run time). As expected, the interaction rate of neutrinos increases with non-isoscalarity of the target, while the one of antineutrinos decreases. This is due to the fact

that neutrinos have larger interaction cross-section on neutrons than protons, while for the antineutrinos it is the other way around.

According to vertex position and material, the geometry has been divided into six sub-volumes:

- opdy_lead - lead contained in the OPERA detector,
- opdy_iron - iron contained in the OPERA detector,
- opdy_iso - all other materials contained in the OPERA detector,
- borexino - Borexino experiment and its infrastructure,
- front_rock - rock upstream of the Hall C,
- below_hallc - rock below Hall C, and
- side_and_above_hallc - concrete shield and rock around hall Hall C, except the rock below.

A separate MC production has been made for each of the volumes and each of the beamfiles described in the Table 4.3.

A probability density of neutrino interactions has been calculated for every material in all of the six sub-volumes. Suppose that there are N different materials present in the sub-volume of interest, the probability density that a neutrino interacts in the material i is then:

$$P_i = \frac{1}{V_i} \frac{R_i}{\sum_{j=1}^N R_j}, \quad (4.25)$$

where V_i is a total volume occupied by the material and R_i is a shorthand for the $R_{\text{pot}}^{\text{TOT}}$ from the equation (4.14).

To improve the selection performance, the *optimized probability* is defined:

$$P_i^{\text{opt}} = \frac{P_i}{\max\{P_j\}_{j=1}^N}. \quad (4.26)$$

It is value for the material with the largest probability density is 1, which helps accelerate the algorithm described below.

The algorithm to select the neutrino interaction vertex is as follows:

1. Generate a random coordinate \vec{r} in a box surrounding the volume of interest.
2. If the coordinate is not in the volume of interest, go back to step 1.
3. Generate a random number s in the interval $[0, 1]$.
4. If s is less than the optimized probability P_i^{opt} for the material at the coordinate \vec{r} , accept the coordinate as an interaction vertex, otherwise go back to step 1.

The distribution of ν_μ interaction vertices in the OPERA detector obtained by this algorithm is shown in Figure 4.3.

4.4.3 OpDigit

OpDigit package converts the hits calculated by *OpSim* to *digits*, i.e. detector response. It is at this level that the simulation can be directly compared with the experiment.

The information contained in digits produced by *OpDigit* is available both in MC simulation and in real data, with the exception of emulsion digits which need to pass through additional *OpEmuIO* step to be directly comparable with data.

The available information for each OPERA sensor is summarized below:

- **Scintillator digit**

- Hardware identification information
- Position of the scintillator bar center in the OPERA reference frame. X and Z coordinates are available for vertical bars, and Y and Z coordinates for horizontal bars
- Analogue to digital converter (ADC) count (ADC is connected at the output of the PMT), at each end of the bar
- Number of photoelectrons recorded by PMT's on each end of the scintillator bar (reconstructed from ADC)
- Time when signal was recorded at each end of the bar

- **RPC, XPC and VETO digit**

- Position of the readout strip

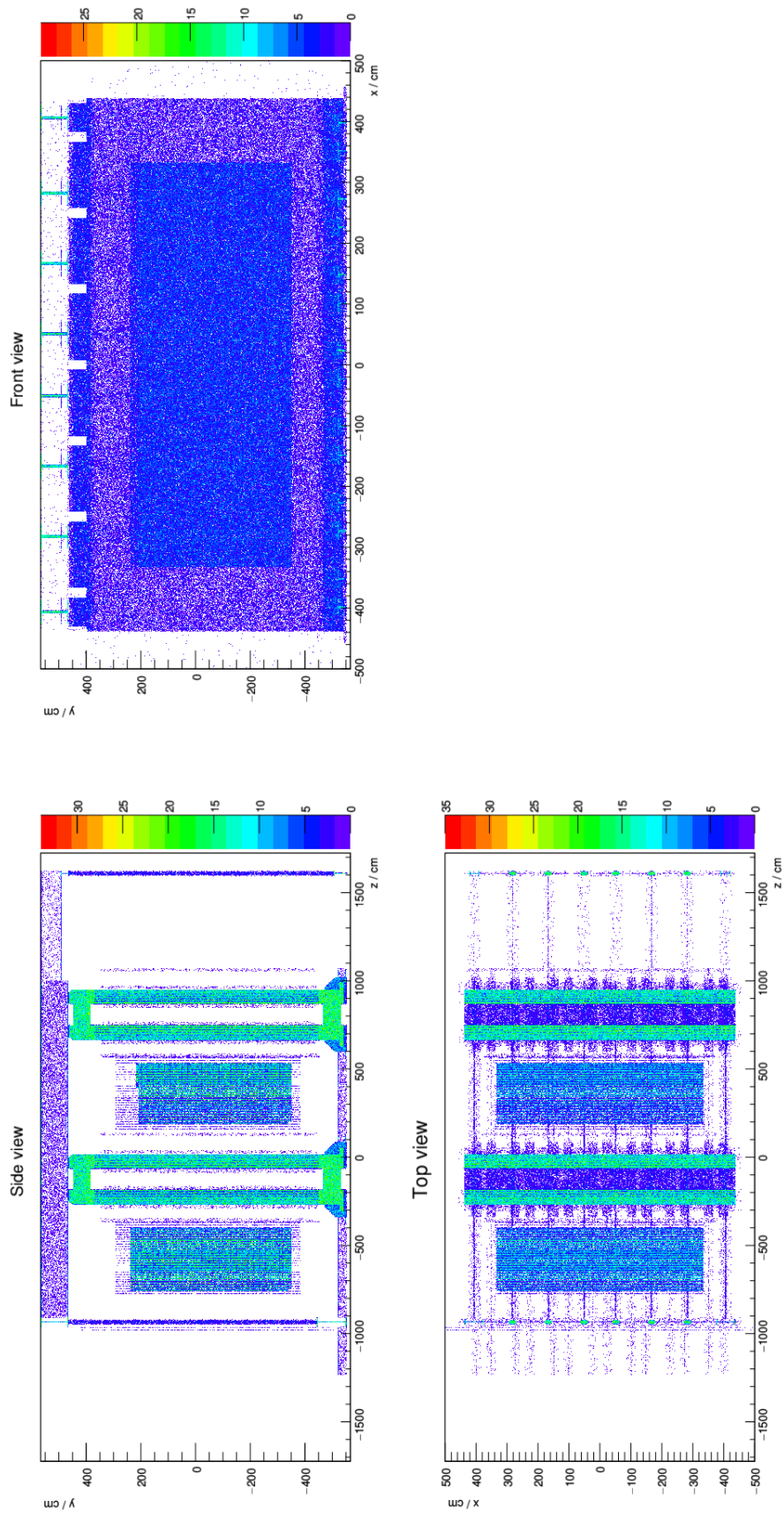


Figure 4.3: Spatial distribution of simulated ν_μ interaction vertices in the OPERA volume. In side and top views the beam is coming from the left, while in the front view the beam is incident to view plane.

- * For RPC and VETO - center of the strip in the OPERA reference frame. X and Z coordinates are available for vertical strips and Y and Z coordinates for horizontal strips.
- * For XPC - center of the strip in XPC specific tilted coordinate system. Must be manually converted to OPERA reference frame.
- RPC, XPC or VETO plane ID
- Number of fired strips in the RPC plane and the ID of the strip which fired first
- Time when signal was recorded
- **PT drift tube digit**
 - Hardware identification of the tube
 - Horizontal position of the drift tube wire in the horizontal plane (X and Z coordinate)
 - Recorded drift time - time between the trigger provided by RPCs and the time signal on the wire was recorded)
 - Corrected drift time - recorded drift time corrected for the various delays in the acquisition system
 - Width of a signal recorded on the wire
 - Drift distance reconstructed from the corrected drift time and signal width
 - Time when digit was recorded
- **Emulsion digit (microtrack)**
 - Position of the microtrack in the OPERA reference frame. The position of a microtrack is defined as a point where it touches the boundary between emulsion and plastic base in the emulsion sheet.
 - Projection of the microtrack length along the Z axis (effectively the emulsion layer thickness)
 - Slopes of the microtrack in XZ and YZ plane

- Identification of emulsion layer containing the microtrack within the ECC brick
- Identification of area within emulsion in which microtrack was recorded (automatic scanning system specific information)
- Coordinates of the brick containing the microtrack

Trigger

At this point in the simulation chain it is possible to simulate the global detector trigger, i.e. conditions under which the detector will record a neutrino interaction. Over the course of the data-taking run, the real trigger has been changing over time to tune for the maximum acceptance of ν_τ events. Because of this, the simulated trigger is deliberately stricter than the real one, to improve consistency between MC simulation and data. When doing the analysis, this simulated trigger is applied to both MC and data.

The trigger is composed of three logical parts: the TT trigger, the RPC (spectrometer) trigger and the cut on minimal number of TT+RPC digits recorded. These logical parts are true if:

- TT trigger (T_{TT}) - Two consecutive TT planes exist with digits containing at least 1 photoelectron in each plane **or** a single TT plane exists with digits containing more than 500 ADC in total.
- RPC trigger (T_{RPC}) - At least 3 RPC planes in a single spectrometer contain at least one digit each.
- Digit number cut (T_{digit}) - More than 10 digits recorded cumulatively by TT and RPC sensors.

The total trigger T_{tot} is then defined as

$$T_{\text{tot}} = (T_{\text{TT}} \text{ or } T_{\text{RPC}}) \text{ and } T_{\text{digit}} .$$

An event is selected if T_{tot} is true.

The distribution of simulated interaction positions which triggered the detector is shown in Figure 4.4.

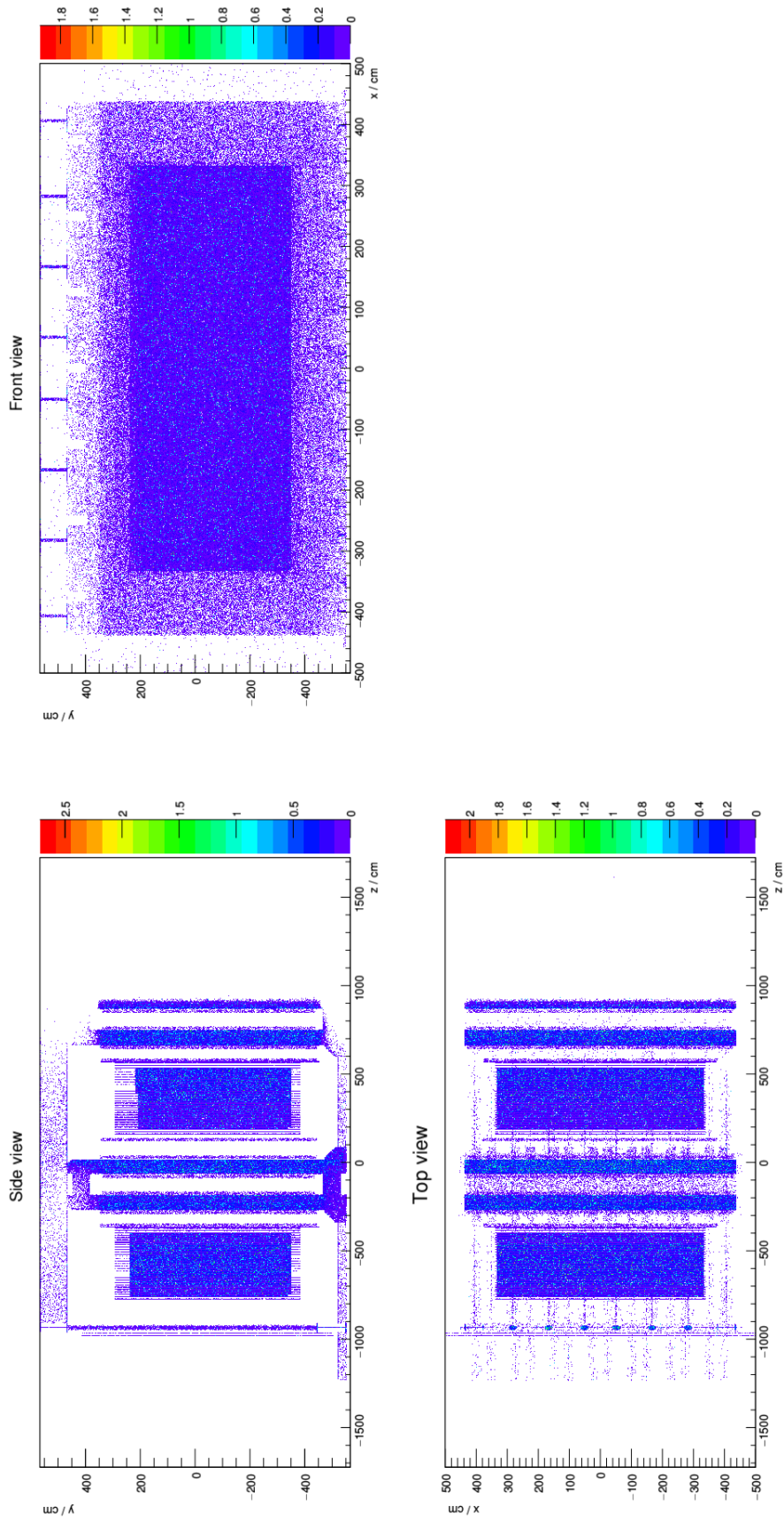


Figure 4.4: Spatial distribution of ν_μ interaction vertices which triggered the detector. In side and top views the beam is coming from the left, while in the front view the beam is incident to view plane. To be compared with all interaction vertices shown in Figure 4.3.

4.4.4 OpRec

The *OpRec* package reconstructs and classifies neutrino interaction events using electronic sensor responses, i.e. digits. No emulsion data is used at this step. The digits can come from MC simulation, i.e. *OpDigit* package, or they can come from real measurements.

Projections of tracks to vertical and horizontal plane are reconstructed separately by combining the recorded digits. These two projections are then combined into a three dimensional track. A Kalman filter [51] is used to reject noise digits not belonging to the track, and to reconstruct the track curvature in the spectrometers to measure the particle momentum [52].

The events which happened during the CNGS time window are classified into these categories [53]:

- CONTAINED - interactions which happened in the target area,
- SPECTRO - interactions which happened in spectrometers,
- FRONTMUON - external muons coming from the front direction,
- SIDEMUON - external muons coming from the side of the detector, and
- BRODERSOFTNC - external events mimicking muon-less interactions on the border of the detector.
- NODECISION - none of the above

4.4.5 OpEmuRec

OpEmuRec package simulates the work done in scanning laboratories to reconstruct neutrino interactions in the ECC brick. The author is the responsible person for OpEmuRec software development and MC production within the OPERA collaboration since late 2012. Since then, results of the OpEmuRec simulation have been used to re-evaluate event location efficiencies within the OPERA ECC brick and have been used in analyses published in [9, 14, 15, 54].

Schematic overview of simulation steps is shown in Figure 4.5. Steps of OpEmuRec algorithm closely follow the ECC event reconstruction described in "ECC event reconstruction" part of Section 3.3.3. The reader is advised to consult that chapter if any of the terminologies used here are unfamiliar.

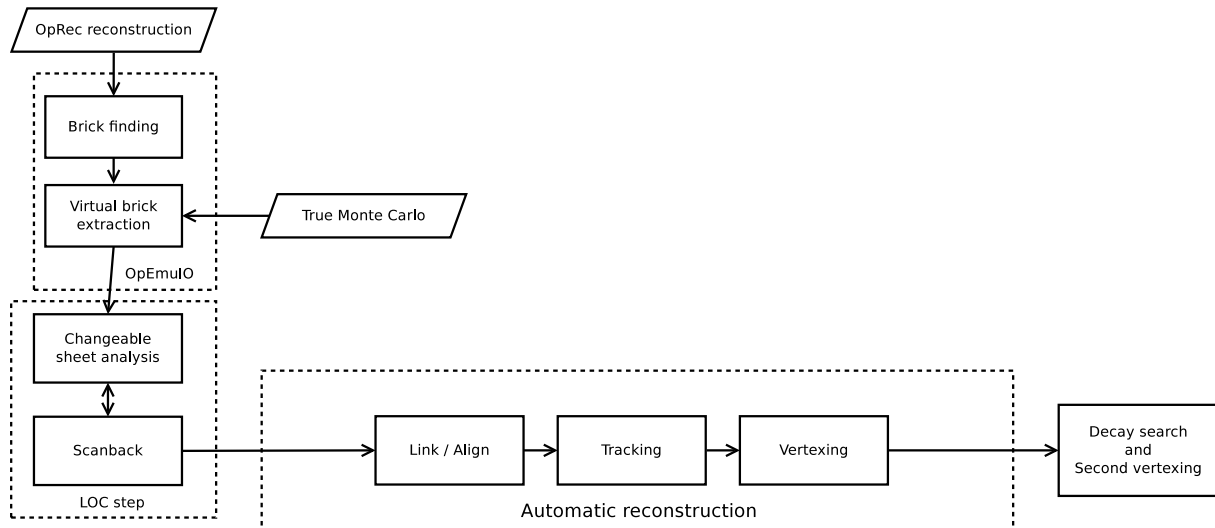


Figure 4.5: Schematic overview of the OpEmuRec simulation of ECC reconstruction.

OpEmuIO

OpEmuIO step simulates the extraction of the ECC brick from the detector and applies the scanning efficiencies on the microtracks produced by *OpDigit*. First, the BrickFinding (BF) algorithm is applied to the fully simulated and reconstructed electronic detector (ED) data. Bricks predicted by this algorithm are then *virtually extracted*. Virtual brick extraction applies the scanning system efficiency to microtracks contained in the brick and saves them in a special data structure called a *virtual brick*.

Location step

Procedures leading to the location of the stopping point of tracks entering the ECC are simulated in this step.

First, the track identification in changeable sheet (CS) part of the ECC is simulated. This follows procedures performed at the dedicated LNGS facility, resulting in a set of

candidate CS tracks. These tracks are then followed through the virtual brick until they stop by the algorithm called SCANBACK.

If CS analysis fails to find any tracks entering the virtual ECC or if SCANBACK algorithm fails to find a stopping point, the next virtual brick ranked by BF algorithm according to a probability that it contains a primary interaction vertex is processed through the location step. After third brick in the ranking is processed and no stopping point is found then the *OpEmuRec* algorithm terminates.

Automatic reconstruction

This step simulates the volume scan and the automatic reconstruction of the tracks and vertices using microtracks contained within.

A virtual volume scan is first performed around the stopping point of tracks from the location step. A virtual volume scan simply copies all microtracks contained within the volume of interest in virtual ECC to a different data structure. Automatic reconstruction algorithms which run on real data can be directly applied to the virtual volume scan. The reconstruction algorithm thus aligns the virtual plates, finds tracks and vertices exactly as it would for the real data.

Decay search and second vertexing

This step simulates the manual procedures done at the emulsion scanning laboratories after the automatic reconstruction. It uses the output of the previous step and attempts to find additional tracks attached to primary and/or secondary vertex.

After this step is done, the output of simulated ECC reconstruction is identical to the one done on real data. As an example, charged hadron multiplicity distribution obtained using *OpEmuRec* compared to real data is shown in Figure 4.6.

4.4.6 Event reweighting

Simulated events produced by the OPERA MC chain are not weighted in any way, i.e. they all have weight $w = 1$. A dedicated tool was built for this analysis that reweights all simulated events according to the neutrino interaction probability.

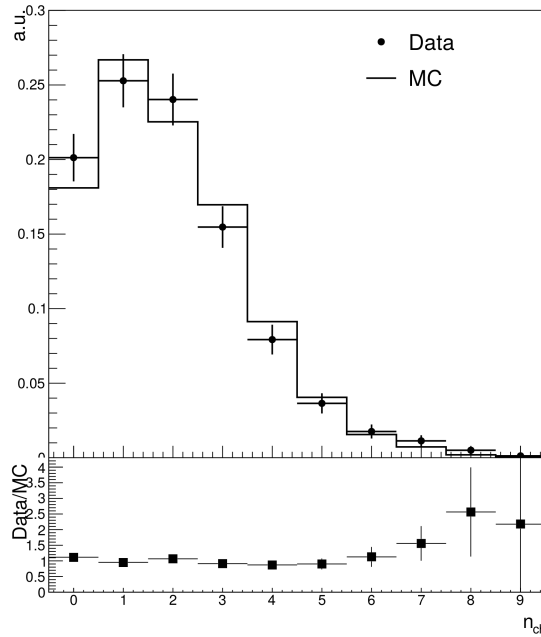


Figure 4.6: Charged hadron multiplicity in the ν_μ CC interaction measured by OPERA. Solid line is MC prediction obtained using *OpEmuRec*, dots are data obtained from OPERA ECC. Figure taken from [54].

First, a total interaction rate per p.o.t. of a flux component⁸ is calculated for a sub-volume⁹ in which events are simulated. The rates are calculated using the equation (4.14). Ingredients needed to calculate an interaction rate are: total mass of the material, molar mass of the material, neutrino cross-sections in a material, and the energy spectrum of the CNGS beam.

Total mass and molar mass of all materials in OPERA detector were obtained from the OPERA geometry software implementation. Neutrino cross-sections were calculated using *Genie 2.8.6*, by running the bundled `mksp1` utility. CNGS energy spectra shown in Figure 3.2 were used.

Total interaction rates were calculated for all 12 flux components (4 prompt and 8 appearance¹⁰) and all 7 sub-volumes. These interaction rates were multiplied by the total integrated intensity of a CNGS beam, which is $1.797 \cdot 10^{20}$ p.o.t, which yields the total number of expected interactions.

Events simulated in each subvolume were then reweighted in such a way that their

⁸See Section 4.2.

⁹See Section 4.4.2.

¹⁰An appearance flux component for oscillation channel $\nu_\alpha \rightarrow \nu_\beta$ is constructed by using the prompt energy spectrum of ν_α and replacing its neutrino flavour by ν_β .

total weight is equal to expected number of events.

Event weights of the prompt flux components represent the expected number of events assuming no oscillation hypothesis.

On the other hand, event weights of the appearance fluxes do not represent the expected value of events in any physical way¹¹. Only when they are reweighted by the appearance probability, they represent the expected number of events in the appearance channel. The event weights of appearance fluxes before the oscillation probability is applied are called the **unoscillated** weights, to discern them from weights obtained using the no oscillation hypothesis.

4.5 Dedicated Monte Carlo production

A dedicated full Monte Carlo simulation has been produced by the author for the purposes of this work.

Materials in OPERA are classified into three categories¹² - LEAD, IRON and ISO. Since all flux components have different weak interaction cross-sections and particle products, a beamfile for each combination of material and flux component would be required. There are 4 prompt flux components and $4 \times 2 = 8$ appearance components, making a total of 12 flux components. The total number of different beamfiles that must be produced would therefore be $12 \times 3 = 38$.

A single configuration of the OPERA simulation chain is defined by a flux component and an OPERA sub-volume¹³. Since there are 7 subvolumes, a full simulation would have to be run in 84 different configurations.

To avoid an overproduction of simulated data in production channels¹⁴ which negligibly contribute to the total number of events which triggered the OPERA detector, a small production was initially done using ν_μ prompt flux. This allowed to estimate the trigger efficiency in different channels with respect to number of interactions in that channel.

¹¹For example, weights of $\nu_\mu \rightarrow \nu_\tau$ flux component would represent the number of ν_τ interactions if ν_τ were a prompt neutrino component of the beam with the energy spectrum of ν_μ .

¹²Described in Section 4.3.2.

¹³Defined in Section 4.4.2.

¹⁴A production channel here is defined by the flux component and subvolume.

These trigger¹⁵ efficiencies were then used as an approximation for other flux components, knowing that they are actually an upper limit when applied to other fluxes since OPERA detector is most efficient when interactions contain muons. Only production channels which are expected to contribute with more than 1 observed event in the OPERA detector have been chosen.

First, beamfiles needed for the full simulation were generated using Genie 2.8.6 in all required materials. The output of Genie was then run through the purpose built program which converts the output format of Genie to OPERA data model and rotates all particle momenta to account for the beam tilt. The number of generated neutrino interactions is shown in Table 4.3.

Table 4.3: Number of generated interactions for different oscillation channels and different materials.

Flux	ν flavour	Number of events			Oscillation channel
		LEAD	IRON	ISO	
ν_μ	ν_μ	10^6	10^6	$3 \cdot 10^6$	$\nu_\mu \rightarrow \nu_\mu$
	ν_e	10^6	10^6	10^6	$\nu_\mu \rightarrow \nu_e$
	ν_τ	10^6	10^6	10^6	$\nu_\mu \rightarrow \nu_\tau$
$\bar{\nu}_\mu$	$\bar{\nu}_\mu$	10^6	10^6	10^6	$\bar{\nu}_\mu \rightarrow \bar{\nu}_\mu$
ν_e	ν_e	10^6	10^6	10^6	$\nu_e \rightarrow \nu_e$
$\bar{\nu}_e$	$\bar{\nu}_e$	10^6	10^6	10^6	$\bar{\nu}_e \rightarrow \bar{\nu}_e$

These beamfiles were then used to produce full OPERA electronic detector simulation for the channels chosen by the trigger analysis described above. The production numbers are shown in Table 4.4, which contains the following quantities:

- Subvolume - OPERA subvolume defined in Section 4.4.2,
- Flux component - the flux component as defined in Section 4.4.2,
- N_{prod} - the total number of produced MC events,
- w_{unosc} - the total unoscillated weight of produced events,
- N_{trig} - the total number of simulated events which triggered the detector,
- $w_{\text{unosc}}^{(\text{trig})}$ - total unoscillated weight of triggered events,

¹⁵See Section 4.4.3.

- $w_{\text{noosc}}^{(\text{trig})}$ - total weight of triggered events assuming no oscillations, and
- $w_{\text{osc}}^{(\text{trig})}$ - total weight of triggered events assuming standard oscillation parameters (see Table 2.4).

The of total 412 million simulated events were produced, out of which 2.5 million trigger the detector.

The total weight of all triggered events is an expected number of events recorded by OPERA detector, including interactions occurring in the apparatus and in the material surrounding it. The expected number of events for no oscillation hypothesis is 96051 events, and assuming standard oscillations is 95056. This is to be compared with the total number of events passing the trigger actually recorded by OPERA, which is 93458. The expected and measured number of events agree well within the quoted (10 - 20) % uncertainty of the CNGS flux prediction.

One would expect that the total unoscillated weight of $\nu_\mu \rightarrow \nu_e$ events is approximately equal to $\nu_\mu \rightarrow \nu_\mu$, since ν_μ and ν_e have the same interaction cross-sections on nuclei in CNGS energy region¹⁶. The reason why these numbers are different in the Table 4.4 is because prompt unoscillated flux components are used to produce NC interactions along with CC interactions, while appearance flux components are used only for producing CC interactions (see Section 4.2).

A part of this production was used as an input to *OpEmuRec* to simulate event reconstruction in emulsions, which was used in ν_e appearance analysis [9] and the final ν_τ analysis [15].

The full production was used in this work to constrain oscillation parameters using OPERA electronic detector data, as described in the next chapter.

¹⁶ ν_τ has a smaller interaction cross-section because of tau lepton production threshold induced by its mass.

Table 4.4: Number of produced MC events in different subvolumes and for different oscillation channels. See text for the description of quantities shown in the table.

Subvolume	Flux component	N_{prod}	w_{unosc}	N_{trig}	$w_{\text{unosc}}^{(\text{trig})}$	$w_{\text{hoosc}}^{(\text{trig})}$	$w_{\text{osc}}^{(\text{trig})}$
opdy_lead	$\nu_\mu \rightarrow \nu_\mu$	1000000	16548.1	969237	15008.1	15008.1	14759.3
	$\bar{\nu}_\mu \rightarrow \bar{\nu}_\mu$	47500	343.8	45084	305.3	305.3	301.0
	$\nu_e \rightarrow \nu_e$	20000	149.0	19510	136.0	136.0	135.9
	$\bar{\nu}_e \rightarrow \bar{\nu}_e$	4000	8.7	3834	7.8	7.8	7.8
opdy_iso	$\nu_\mu \rightarrow \nu_e$	10000	12701.4	9993	11876.7	0.0	8.8
	$\nu_\mu \rightarrow \nu_\tau$	10000	5851.2	9940	5442.3	0.0	68.8
opdy_iron	$\nu_\mu \rightarrow \nu_\mu$	500000	3239.1	443080	2808.3	2808.3	2762.9
	$\bar{\nu}_\mu \rightarrow \bar{\nu}_\mu$	10000	74.4	8722	63.5	63.5	62.6
	$\nu_e \rightarrow \nu_e$	5000	29.2	4438	25.3	25.3	25.3
	$\bar{\nu}_e \rightarrow \bar{\nu}_e$	1000	1.9	861	1.6	1.6	1.6
	$\nu_\mu \rightarrow \nu_\tau$	2000	1115.4	1798	979.7	0.0	11.8
	$\nu_\mu \rightarrow \nu_e$	2000	2451.3	1801	2158.3	0.0	1.5
borexino	$\nu_\mu \rightarrow \nu_\mu$	1000000	30664.7	533960	16474.5	16474.5	16211.5
	$\bar{\nu}_\mu \rightarrow \bar{\nu}_\mu$	100000	680.6	51430	352.2	352.2	347.8
	$\nu_e \rightarrow \nu_e$	30000	276.2	15201	140.8	140.8	140.7
	$\bar{\nu}_e \rightarrow \bar{\nu}_e$	2000	17.2	959	8.3	8.3	8.3
front_rock	$\nu_\mu \rightarrow \nu_\tau$	20000	10659.1	10536	5649.8	0.0	59.6
	$\nu_\mu \rightarrow \nu_e$	20000	23324.5	9356	10978.4	0.0	6.0
	$\nu_\mu \rightarrow \nu_\mu$	1000000	65913.1	152361	10104.4	10104.4	9965.6
	$\bar{\nu}_\mu \rightarrow \bar{\nu}_\mu$	150000	1512.6	29150	295.8	295.8	293.0
below_hallc	$\nu_e \rightarrow \nu_e$	150001	593.2	14091	56.1	56.1	56.0
	$\bar{\nu}_e \rightarrow \bar{\nu}_e$	4000	38.1	351	3.4	3.4	3.4
	$\nu_\mu \rightarrow \nu_\mu$	385000000	42858750.0	186425	20880.8	20880.8	20783.1
side_and_above_hallc	$\bar{\nu}_\mu \rightarrow \bar{\nu}_\mu$	10000000	984859.0	11700	1159.4	1159.4	1156.3
	$\nu_e \rightarrow \nu_e$	4400000	385730.9	20	1.8	1.8	1.8
Total	$\nu_\mu \rightarrow \nu_\mu$	2500000	2483795.9	18396	18389.3	18389.3	18178.5
	$\bar{\nu}_\mu \rightarrow \bar{\nu}_\mu$	1000000	57075.6	10957	629.2	629.2	625.2
	$\nu_e \rightarrow \nu_e$	300000	22354.3	431	32.3	32.3	32.3
Total	$\nu_\mu \rightarrow \nu_\mu$	3990000	4070297.1	8780	9011.8	9011.8	8886.2
	$\bar{\nu}_\mu \rightarrow \bar{\nu}_\mu$	1000000	93532.1	1654	155.7	155.7	153.8
-		412277501	51132587.7	2574056	133136.6	96051.6	95056.3

Chapter 5

Analysis

This chapter describes the analysis of OPERA electronic detector data and constrains to $|\Delta m_{32}^2|$ implied by this data. The chapter starts with the definition of statistical formalism used to constrain the parameter, in which likelihood function and test statistic play a principal role. Then it explains in detail how the likelihood function is constructed, how statistical distributions entering the likelihood are obtained, and the selection of OPERA data. After that, two test statistics are constructed using this likelihood function, and the way p -values were obtained for different values of Δm_{32}^2 is explained. Finally, constraints on $|\Delta m_{32}^2|$ obtained by this method are presented.

5.1 Statistical formalism

Any statistical treatment of an experimental data set can only reject a theoretical hypothesis, it can never explicitly confirm one. A theoretical hypothesis, in the sense used here, is a theory that explains (or not) data recorded by the experiment. In this case, it consists of the underlying neutrino oscillation theory with its own set of parameters which we wish to extract, the theory of neutrino interactions with matter (given by the event generator), our knowledge of the neutrino beam (given by the incoming neutrino spectrum), and the detector response (given by the MC simulation of the detector).

5.1.1 Test statistic and the p -value

Test statistic is a real valued function on a data set, usually constructed in such a way that larger values indicate greater incompatibility between data and null hypothesis. Null hypothesis is a hypothesis (theory) which is either rejected or not by the data. It is important to note that since data are a random variable, the test statistic is too, following a certain probability density function. Given this probability density function, which can be calculated (at least in principle) for any test statistic, one can construct a p -value for any null hypothesis:

$$p_{t_{H_0}} = \int_{t_{H_0}^{\text{obs}}}^{\infty} f_{t_{H_0}}(t) dt , \quad (5.1)$$

where p_{H_0} is the p -value given by a test statistic t_{H_0} assuming the null-hypothesis H_0 , $t_{H_0}^{\text{obs}}$ is a value of a test statistic given observed data, and $f_{t_{H_0}}$ is a probability density function of the test statistic t_{H_0} . Thus, a p -value is a probability that the observed data set is this or more incompatible with the null hypothesis.

The p -value will be used as a rejection criterion for a given null hypothesis. Null hypotheses with p -value below a predefined threshold will be rejected and not-rejected hypotheses will be regarded as possible ones.

5.1.2 Likelihood function

The likelihood function is a very commonly used object in the data analysis theory, the detailed description can be found in, for example in Chapter 6 of the book [55].

In general, a likelihood function is a function of parameters included in the theoretical model of the experiment and the data measured by the experiment. Since data is intrinsically a statistical random variable, the likelihood function is a random variable as well. The theoretical parameters are divided into the parameters of interest (i.e the ones one wishes to constrain), those that are known *a priori* (i.e. the ones known from other sources), and the *nuisance* parameters which one is not interested in, but are nevertheless present in the model. The nuisance parameters are usually describing the systematic uncertainties of the experiment, but can include the physical parameters as well if one is not interested in them. Introduction of nuisance parameters increases the uncertainty on parameters of interest obtained from the analysis.

The following notation shall be used when dealing with likelihoods:

$$L(\Theta, \Phi; \text{data}) , \tag{5.2}$$

where Θ are a set of parameters of interest, Φ a set of nuisance parameters, and L is a label for a likelihood function.

Profile likelihood

Given the likelihood $L(\Theta, \Phi; \text{data})$, the profile likelihood is defined as:

$$\lambda(\Theta; \text{data}) = \frac{L\left(\Theta, \hat{\Phi}; \text{data}\right)}{L\left(\hat{\Theta}, \hat{\Phi}; \text{data}\right)} , \tag{5.3}$$

where $\hat{\Phi}$ is a value of nuisance parameters which maximizes the likelihood function with a fixed Θ , while $\hat{\Theta}$ and $\hat{\Phi}$ are a set of parameters of interest and nuisance parameters which maximize the likelihood simultaneously, i.e. $L\left(\hat{\Theta}, \hat{\Phi}; \text{data}\right)$ is a global maximum of the likelihood function given data. It should be noted that the profile likelihood is bounded between 0 and 1 by construction. The profile likelihood is a function only of the parameters of interest, and not the nuisance parameters.

Profile likelihood is often used in construction of test statistics for a certain hypothesis. The general form of such a test statistic is:

$$t_{\Theta} = -2 \ln \lambda(\Theta; \text{data}) . \tag{5.4}$$

The higher values of this test statistic indicate greater incompatibility between data and null-hypothesis Θ . This simple form must be used with care, because it doesn't take into account the theoretical boundaries of parameters of interest Θ [56].

5.2 Construction of the likelihood function

The largest systematic uncertainty important in this analysis is the limited knowledge of the incoming neutrino flux. Since OPERA experiment does not include a near detector

(i.e. a detector placed close to the beam source), one is forced to use the simulated beam profile at the location of the OPERA detector. The simulation was done by the CNGS team, with the uncertainty of the flux estimated to be 10 – 20% [57]. Since OPERA detector is sensitive both to NC and CC neutrino interactions, the ratio of number of NC over CC events as a function of an observable was used in this analysis to mitigate the effects of beam uncertainty to a large degree. Since NC interaction rate is invariant in the standard neutrino oscillation theory, it can be used as a way to measure the initial neutrino flux (but very limited by OPERA statistics). This was necessary since the dominant effect of neutrino oscillations visible in the electronic detectors of the OPERA detector is *disappearance* of muon neutrinos, which is very sensitive to the flux normalization.

Ratios of number of observed events follow different statistical distributions than standard Poissonian distributions which govern standard analyses most common in the literature. Therefore, special statistical methods had to be used to properly construct the uncertainties in the measurements presented here.

5.2.1 Statistics of a counting histogram

Suppose there is a physical observable a which one can measure for each event. This observable is just a function of output of various sensors of the experimental apparatus.

Suppose one creates a histogram of this observable a which has N bins. The i -th bin ($i = 1, \dots, N$) of the histogram covers the interval $[a_{i-1}, a_i)$, and the set of bin boundaries a_0, \dots, a_N is called a *range* of the histogram. The expected number of events in the i -th bin, λ_i , can be calculated from theory¹, and will in general depend on the physical quantity one wants to measure. The actual number of observed events in i -th bin is a Poisson random variable. That is, the probability to observe k_i events in i -th bin is given by

$$P_i(k|\lambda) = \frac{\lambda_i^k e^{-\lambda}}{k!} . \quad (5.5)$$

Actually, counting the number of events in two different bins can be considered as two independent experiments.

Suppose there is a physical parameter ψ one wants to measure. Unlike λ_i 's which are

¹Theory here means both *physical* theory and our knowledge of the apparatus. The point is that we, in principle, don't have to measure anything to get this number.

dependant on the experimental setup, ψ is a purely theoretical parameter independent of the experiment². The examples relevant for this thesis would be mixing angles and mass square differences in the theory of neutrino oscillations. Since λ_i 's are functions of ψ , by knowing which values of λ_i 's are possible given the experimental data, one can infer which values of ψ are possible given the experimental data³.

5.2.2 Statistics of a ratio of two Poisson random variables

Single Poisson measurement

Suppose one measures a single outcome k of a Poisson random variable with the unknown parameter λ . The probability of λ given k can be calculated using Bayes theorem:

$$P_{\Lambda|K}(\lambda|k) = \frac{P_{K|\Lambda}(k|\lambda)P_{\Lambda}(\lambda)}{P_K(k)} = \frac{P_{K|\Lambda}(k|\lambda)P_{\Lambda}(\lambda)}{\int_0^{\infty} P_{K|\Lambda}(k|\lambda)P_{\Lambda}(\lambda)d\lambda}, \quad (5.6)$$

where $P_{\Lambda|K}(\lambda|k)$ is a probability density function of λ given the outcome k , $P_{K|\Lambda}(k|\lambda)$ is a probability to obtain an outcome k given the Poisson parameter λ , $P_{\Lambda}(\lambda)$ is a *prior* on λ (the probability density function of λ independent of measurement which reflects our prior knowledge about the parameter), and $P_K(k)$ is an *a priori* probability to measure k which enters the equation only as a normalizing factor. Assuming no prior knowledge on λ , all λ 's are equally probable, i.e. they form a *flat* prior:

$$P_{\Lambda}(\lambda) = \begin{cases} 1/\lambda_c & \text{if } 0 \leq \lambda < \lambda_c \\ 0 & \text{otherwise} \end{cases}, \quad (5.7)$$

where λ_c is an arbitrary cut-off one is forced to introduce to preserve the normalization of $P_{\Lambda}(\lambda)$. However, for any k , one can choose such $\lambda_c \gg k$ that for each $\lambda^* > \lambda_c$, the value of

$$P_{K|\Lambda}(k|\lambda^*) = \frac{(\lambda^*)^k e^{-\lambda^*}}{k!} \quad (5.8)$$

²If the theory in question is sufficiently good in describing the natural phenomena.

³Actually, the most correct statement would be that one can infer which values of ψ are not impossible.

is arbitrarily small. Then the following approximations hold:

$$P_{K|\Lambda}(k|\lambda)P_{\Lambda}(\lambda) \approx P_{K|\Lambda}(k|\lambda)/\lambda_c, \quad (5.9a)$$

$$\int_0^{\infty} P_{K|\Lambda}(k|\lambda)P_{\Lambda}(\lambda)d\lambda \approx 1/\lambda_c. \quad (5.9b)$$

Using the above approximations, the equation (5.6) becomes:

$$P_{\Lambda|K}(\lambda|k) \approx P_{K|\Lambda}(k|\lambda) = \frac{\lambda^k e^{-\lambda}}{k!}. \quad (5.10)$$

This is a probability density function of a variable λ with an integer k as a parameter. It is a special case of a Gamma distribution [58]:

$$P_{\Gamma}(x; \alpha, \theta) = \frac{x^{\alpha-1} e^{-\frac{x}{\theta}}}{\Gamma(\alpha)\theta^{\alpha}}. \quad (5.11)$$

It is easy to see $P_{\Lambda|K}(\lambda|k)$ is given by:

$$P_{\Lambda|K}(\lambda|k) = P_{\Gamma}(\lambda; k+1, 1). \quad (5.12)$$

Measurement of a ratio of two Poisson random variables

Suppose one measures the outcomes k and l of two independent Poisson random variables with unknown means λ_k and λ_l , respectively. Suppose that the parameter of interest is a ratio between the two means

$$x \equiv \frac{\lambda_l}{\lambda_k}, \quad (5.13)$$

rather than individual parameters λ_l and λ_k .

The probability density $P_X(x)$ of the random variable X can be found using the formula for the distribution of a ratio of two random variables.

Given probability density functions $f_X(x)$ and $f_Y(y)$, the distribution $f_Z(z)$ of ratio of random variables x/y , with $Z \equiv X/Y$ and $z \equiv x/y$ is given by a formula:

$$f_Z(z) = \int_{-\infty}^{\infty} f_X(zx)f_Y(x)|x|dx. \quad (5.14)$$

By setting

$$f_X(x) = P_{\Lambda|L}(x) , \quad (5.15a)$$

$$f_Y(x) = P_{\Lambda|K}(x) , \quad (5.15b)$$

$$f_Z(x) \equiv P_{X|L,K}(x|l, k) , \quad (5.15c)$$

and doing the integration (5.14), one obtains a formula:

$$P_{X|L,K}(x|l, k) = \frac{(k+l+1)!}{k! l!} \frac{x^l}{(1+x)^{k+l+2}} . \quad (5.16)$$

This is a probability density function of a ratio of two Poisson expected values λ_l and λ_k , given the measurements l and k . It is a function of a continuous variable x with two integer parameters l and k . The simplified notation

$$P_{l/k}(x) \equiv P_{X|L,K}(x|l, k) \quad (5.17)$$

will be used in the remainder of the text.

It is interesting that this simple closed form is possible for the ratio of two distributions $P_{\Lambda|K}(\lambda|k)$ for arbitrary k , while for the ratio of two arbitrary Gaussians the closed form does not exist.

5.2.3 NC-like and CC-like event selection

The selection between NC-like and CC-like events is based on the detection of a muon in the electronic detectors. In short, CC-like events are the ones in which a *clean* muon track is reconstructed, while the NC-like events are the ones in which there are no *clean* muon tracks reconstructed. The events that do not fall in either of these two categories are discarded from the analysis⁴. The requirements for the CC-like events are as follows:

- At least one reconstructed muon track, based on the OPERA muon reconstruction algorithm.

⁴One could, for example, have an event in which there is a reconstructed muon track, but it is not classified as *clean*. In that case, the event is completely discarded from the analysis.

- There is *bending topology* - at least one digit in each of the arms of at least one spectrometer. This insures that the muon reconstruction algorithm used both⁵ arms of at least one spectrometer.
- A spectrometer reconstructed charge of a muon track is negative and the reconstructed momentum is classified as *good*. The positive muon tracks are not used since the uncertainty on prompt $\bar{\nu}_\mu$ flux component is significantly larger than the one on ν_μ component.

The NC-like events are defined as follows:

- No tracks are reconstructed as muon tracks.
- There is no *bending topology*.

In addition to the NC/CC classification, there is also a global event selection. An event is selected if:

- It passes the simulated detector trigger - simulation of the trigger is applied to both MC and data. The actual detector trigger has varied during the data taking run. To mitigate this, the simulated trigger threshold is a bit higher than the highest one used during data taking, so a small number of data events are rejected here too.
- Is classified as *CONTAINED* by OPERA reconstruction software.
- Is successfully processed by the *Brick finding* algorithm.
- More than 600 photoelectrons accumulated in PT's of TT system.
- Brick finding algorithm predicts it has occurred in the first 20 brick walls in the target area of a single supermodule - this is a fiducial volume cut.
- Is classified as either NC-like or CC-like.

The CC-like and NC-like selections are mutually exclude, i.e. no event can be a member of both sets. Table 5.1 shows the efficiency of the global selection in three

⁵As opposed to the single arm of the spectrometer, which is also possible but has larger momentum uncertainty.

exclusive interaction volumes, calculated using MC simulation. One can see that global selection strongly rejects neutrino events happening outside the OPERA target, while retaining almost half of the events happening inside the target.

Table 5.1: Efficiency of the global selection wrt. all triggered events calculated using MC simulation, for three different neutrino interaction position volumes. Volumes are: Target - ECC bricks, their support structures and scintillator target trackers, Internal - all other parts of the OPERA detector (spectrometer, support structures, etc.), External - material outside of the OPERA detector (Borexino detector and its supporting infrastructure, and rock around the experimental hall). Together these volumes contain all simulated neutrino interactions.

	Efficiency (%)
Target	44.3
Internal	0.2
External	0.06

The expected flavour composition and interaction type (CC or NC) of neutrino events selected by the three cuts is shown in the Table 5.2. The CC-like selection is very efficient in selecting the actual CC events coming from the ν_μ flavour component of the beam, with purity of 99.5%. The NC-like selection is less pure since (i) the physical muon track may not be reconstructed in the detector due to detection efficiency and (ii) the CC interactions of other neutrino flavours do not produce a muon. This is mitigated to a large degree in the analysis where the effect of neutrino oscillations is calculated for both NC-like and CC-like sample.

Table 5.2: Neutrino interaction type and flavour composition of Monte Carlo samples for global, CC-like and NC-like selections, under the assumption of world average neutrino oscillation parameters. 'Other CC' events include disappearance of prompt flux flavours $\bar{\nu}_\mu$, ν_e , $\bar{\nu}_e$ and flavours coming from the appearance effects $\nu_\mu \rightarrow \nu_\tau$, $\nu_\mu \rightarrow \nu_e$.

Selection	Proportion of events (%)		
	ν_μ CC	ν and $\bar{\nu}$ NC	Other CC
Global	82.0	16.8	1.2
CC-like	99.5	0.2	0.3
NC-like	20.2	75.3	4.5

The full interaction type and flavour composition of the selected samples is shown in Figure 5.1.

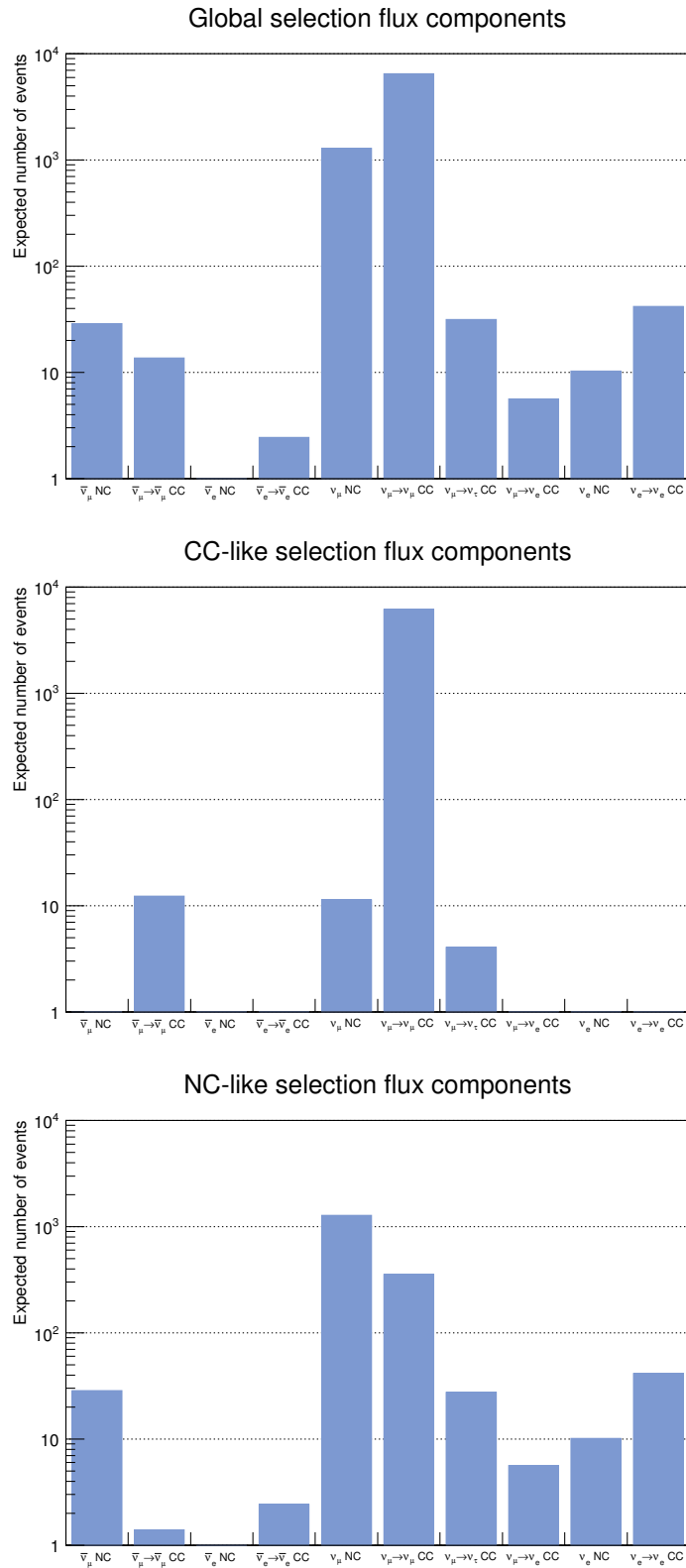


Figure 5.1: Neutrino flavours and interaction type distribution in the three selection samples, assuming the world average neutrino oscillation parameter values. The vertical axis shows the expected number of events under assumption of total delivered CNGS integrated intensity of $18.24 \cdot 10^{19}$ p.o.t. Contributions from flux components with less than one expected event are outside of the vertical axis range, but are included in the analysis.

5.2.4 Neutrino energy proxy variable

Since it is physically impossible to measure the energy of an incoming neutrino in a NC interaction because of the unknown amount of energy carried away by the invisible neutrino, one must use a proxy variable instead. The total energy deposited in the scintillator E_{tt} is used for this purpose, since it is well defined for both NC-like and CC-like events.

A distribution of number of observed and predicted events vs. E_{tt} is shown in Figure 5.2.

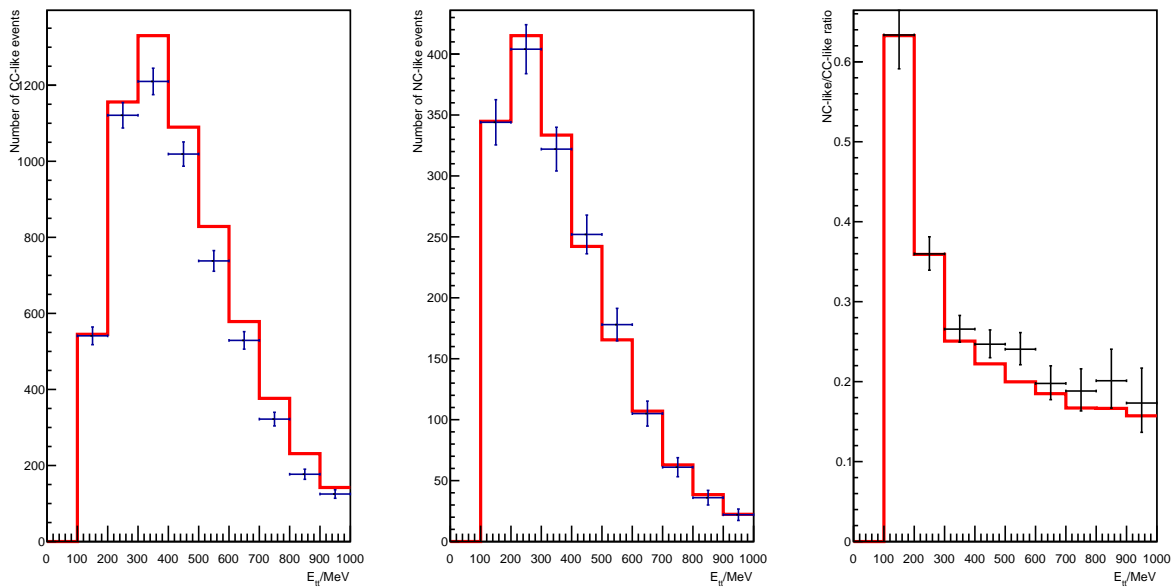


Figure 5.2: Left - distribution of observed CC-like events, vs. E_{tt} . Middle - distribution of observed NC-like events vs. E_{tt} . Right - distribution of observed NC-like/CC-like ratio vs. E_{tt} . The crosses are data points, the red line is the prediction to MC. Note how absolute difference between MC and data is reduced when using the ratio.

5.2.5 Construction of likelihood function

The likelihood function is constructed using three histograms, which have identical ranges in E_{tt} :

1. Histogram of NC-like events vs. E_{tt} (real data),

2. Histogram of CC-like events vs. E_{tt} (real data), and
3. Histogram of NC-like/CC-like ratio vs. E_{tt} as predicted by the MC simulation - this histogram is dependant on the neutrino oscillation parameters.

The likelihood function is then constructed as:

$$L(\Delta m_{23}^2, \theta_{13}, \theta_{23}) = \prod_{i=1}^N P_{\text{NC}_i/\text{CC}_i} (R_i(\Delta m_{23}^2, \theta_{13}, \theta_{23})) , \quad (5.18)$$

where $i = 1, \dots, N$ is a bin label on all three histograms, NC_i and CC_i are numbers of events in the i -th bin of the NC-like and CC-like histograms respectively, $R_i(\Delta m_{23}^2, \theta_{13}, \theta_{23})$ is the NC-like/CC-like ratio predicted by MC simulation as a function of oscillation parameters, and $P_{\text{NC}_i/\text{CC}_i} (R_i(\dots))$ is a probability distribution defined in the equation (5.16).

To calculate $R_i(\Delta m_{23}^2, \theta_{13}, \theta_{23})$, the unoscillated⁶ MC data set must be reweighted according to the oscillation probability of each simulated event. This reweighted MC set is then used to construct the histogram described in the point 3 above.

Reweighting of an event i is done using the formula:

$$w_i^{\text{osc}} = w_i^{\text{unosc}} \cdot P_i(E_\nu^{(i)}; \Delta m_{23}^2, \theta_{13}, \theta_{23}) , \quad (5.19)$$

where w_i^{osc} is the oscillated weight of the event, w_i^{unosc} is unoscillated event weight, $E_\nu^{(i)}$ is simulated neutrino energy, and P_i is an oscillation probability formula for a flux component⁷ that was used to generate the simulated interaction. The true NC interactions are, of course, not re-weighted.

5.3 Construction of test statistics

In order to construct the test statistics, one must decide which parameters will be the paramaters of interest, which ones will be nuisance paramaters and which ones will be considered to be known a priori. Since the theory model contains many independent parameters (e.g. oscillation parameters, neutrino interaction cross sections, neutrino beam

⁶Unoscillated event weights are different than event weights in case of no oscillation for appearance channels.

⁷Essentially the flavour of neutrino. See Section 4.2.

shapes, sensor responses, etc...), it is not reasonable to expect that the data set will be able to provide information on all of them. In this work, the only parameter of interest will be Δm_{32}^2 , while all the others will be considered to be known a priori.

Parametrization of neutrino oscillations

Under the assumption that the mass splitting Δm_{21}^2 can be neglected, only three parameters entering the oscillation theory are left, as shown in Chapter 2.2.5. The set of oscillation equations used in this analysis are:

$$P_{ee} = 1 - M_{ee} \sin^2 \frac{\phi_{32}}{2}, \quad (5.20a)$$

$$P_{e\mu} = M_{e\mu} \sin^2 \frac{\phi_{32}}{2}, \quad (5.20b)$$

$$P_{\mu\mu} = 1 - M_{\mu\mu} \sin^2 \frac{\phi_{32}}{2}, \quad (5.20c)$$

$$P_{\mu\tau} = (M_{\mu\mu} - M_{e\mu}) \sin^2 \frac{\phi_{32}}{2}, \quad (5.20d)$$

where M_{xx} are the *mixing amplitudes*. Since the oscillation formulas are CP and T invariant under the approximation $\Delta m_{12}^2 = 0$, these formulas are valid both for particles and antiparticles, and in both time directions (e.g. $P_{\mu \rightarrow e} = P_{e \rightarrow \mu} = P_{\bar{\mu} \rightarrow \bar{e}} = P_{\bar{e} \rightarrow \bar{\mu}} = P_{e\mu}$).

The mixing amplitudes as functions of mixing angles are found using equations (2.73):

$$M_{ee} = 4s_{13}^2 c_{13}^2, \quad (5.21a)$$

$$M_{e\mu} = 4s_{13}^2 c_{13}^2 s_{23}^2, \quad (5.21b)$$

$$M_{\mu\mu} = 4s_{23}^2 c_{13}^2 (1 - s_{23}^2 c_{13}^2). \quad (5.21c)$$

The ϕ_{23} phase is defined in the equation (2.41c) to be:

$$\phi_{32} = \frac{\Delta m_{32}^2 L}{2E}. \quad (5.22)$$

Test statistics for Δm_{23}^2 as a parameter of interest

Two different test statistics are used when dealing with the Δm_{23}^2 as a single parameter of interest, one to obtain a two-sided confidence interval and one to obtain the upper limit. All other oscillation parameters are a priori fixed to central values quoted in Table 2.4, and there are no nuisance parameters.

Test statistic used for two-sided confidence interval is defined as:

$$t_{\Delta m_{32}^2} = -2 \ln \lambda(\Delta m_{32}^2) . \quad (5.23)$$

Test statistic for the upper limit case is defined as:

$$q_{\Delta m_{32}^2} = \begin{cases} -2 \ln \lambda(\Delta m_{32}^2) & \widehat{\Delta m_{32}^2} \leq \Delta m_{32}^2 \\ 0 & \widehat{\Delta m_{32}^2} > \Delta m_{32}^2 \end{cases} . \quad (5.24)$$

To see why test statistic $q_{\Delta m_{32}^2}$ is a test statistic for the upper limit, one must first remember that $\widehat{\Delta m_{32}^2}$ is a value of Δm_{32}^2 which maximizes the likelihood (5.18), i.e. it is a best fit value of Δm_{32}^2 given observed data. This test statistic is constructed in such a way that it yields the p -value $p = 1$ when⁸ the best fit is larger than the null-hypothesis value of Δm_{32}^2 . Therefore it has a power to discard only null hypotheses in which best fit is larger than the assumed value.

5.3.1 Construction of test statistic distributions and p -values

Test statistic distributions are obtained by creating a set of pseudo-experiments. A pseudo-experiment is conducted by randomly simulating a data set from the existing MC simulation⁹ and then performing the analysis on the simulated pseudo-data set as it were real data. Each pseudo-experiment yields a single value of a test statistic for the null-hypothesis under which MC simulation has been constructed, i.e. Δm_{32}^2 . By performing a number of pseudo-experiments for a single null-hypothesis, one obtains a random sample of test statistics for this null-hypothesis. By definition, this random sample is coming

⁸Since test statistics used here are larger than zero by construction, the integral $\int_{t_{H_0}^{\text{obs}}}^{\infty} f_{t_{H_0}}(t) dt$ from equation (5.1) is equal to one if $t_{H_0} = 0$.

⁹A simulation is assumed to depend on Δm_{32}^2 .

from the probability density function $f_{t_{H_0}}(t)$ defined in the equation (5.1). This sample can then be used to estimate the p -value of the observed¹⁰ test statistic.

The equation (5.1) states that p -value is a probability that a random¹¹ test statistic t_{H_0} is larger than the observed test statistic $t_{H_0}^{\text{obs}}$, under a null-hypothesis H_0 . A randomly generated pseudo-data set, produced with assumption of null-hypothesis H_0 , is used to construct a set of test statistics $t_{H_0}^{(i)}$ with $i = 1, \dots, N$ where N is the number of pseudo-experiments. The probability that k random test statistics out of the set of N pseudo-experiments is larger than the observed one is given by the binomial distribution:

$$P_B(k|p, N) = \binom{N}{k} p^k (1-p)^{N-k} , \quad (5.25)$$

where p is the actual p -value.

Given the values of k and N , the best estimate for a binomial parameter p (the p -value) is

$$\hat{p} = k/N . \quad (5.26)$$

The central confidence intervals around this value are constructed as described in the Appendix B.

Generation of a pseudo-data set

To generate a pseudo data set under an assumption of Δm_{32}^2 , the full MC set is first reweighted according to the oscillation probability defined by Δm_{32}^2 as described in Section 5.2.3.

Events are then randomly selected from a complete¹² reweighted MC set, with the probability of selecting an event into the pseudo-data set directly proportional to its oscillated MC event weight.

The algorithm for creation of a pseudo-data set is as follows:

1. Suppose that there are N events in the MC set after the selection cuts have been applied, and that w_i is the weight of the i -th event ($i = 1, \dots, N$). Construct an

¹⁰Calculated essentially by maximizing the likelihood (5.18) constructed with real data.

¹¹A random realization from the probability density function $f_{t_{H_0}}(t)$ in the equation (5.1).

¹²Including all simulated neutrino interactions, occurring both in the detector and in the surrounding material

array of MC event weight partial sums W_i , $i = 0, \dots, N$, such that $W_0 = 0$ and $W_i = \sum_{k=1}^i w_k$.

2. Generate a uniform random number s from the interval $[0, W_N)$.
3. Find the smallest integer k with the property $W_k > s$.
4. Apply global selection defined in Section 5.2.3 in the k -th element of MC set.
5. If global selection is passed, add the k -th element of the MC set to pseudo-data set.
6. Return to the step 2 until the pseudo-data set contains approximately the same number of events as selected real data.

5.4 Measurement of $|\Delta m_{32}^2|$

Test statistics $t_{\Delta m_{32}^2}$ and $q_{\Delta m_{32}^2}$, defined by equations (5.23) and (5.24) respectively, were used to measure confidence intervals for the mass splitting parameter Δm_{32}^2 with all other oscillation parameters fixed. The test statistic distributions were produced using the procedure described in Section 5.3.1. The null-hypothesis in this case is that the data is described by neutrino oscillation theory with the single parameter of interest Δm_{32}^2 . p -values have been calculated for 101 values of Δm_{32}^2 in the interval $[0.0, 6.0] \cdot 10^{-3} \text{ eV}^2$, which corresponds to the grid spacing of $6.0 \cdot 10^{-5} \text{ eV}^2$. For each value of Δm_{32}^2 , 10000 pseudo-experiments were constructed to obtain test statistic distributions.

The experimental data was used to calculate $t_{\Delta m_{32}^2}^{\text{obs}}$ and $q_{\Delta m_{32}^2}^{\text{obs}}$, which was then used in the formula (5.1) to calculate the p -value under the assumption of Δm_{32}^2 for each of the two test statistics. The p -values between the neighbouring grid points are linearly interpolated.

The results of this calculation are shown in the Figures 5.3 and 5.5. Vertical width of the p -value lines is the 90% confidence interval, where the uncertainty on its value is a consequence of the fact p -values were calculated using finitely many pseudo-experiments. Red lines on the plots show four thresholds on the p -value, below which the null-hypothesis can be rejected by a predefined probability.

Rejection probabilities shown on the plots are: 0.32 corresponding to 1σ , 0.1 corresponding to 90% confidence level, 0.05 corresponding to 2σ , and 0.003 corresponding to 3σ significance. The confidence intervals extracted from this analysis are shown in Tables 5.3 and 5.4. The 90% confidence intervals in data space are shown in Figures 5.4 and 5.6.

Table 5.3: $|\Delta m_{32}^2|$ confidence intervals obtained using the $t_{\Delta m_{32}^2}$ test statistic

$ \Delta m_{32}^2 /10^{-3} \text{ eV}^2$		Confidence
Low bound	High bound	
2.0	3.8	1σ
1.5	4.2	90%
0.9	4.4	2σ
0.0	5.0	3σ

Table 5.4: $|\Delta m_{32}^2|$ confidence intervals obtained using the $q_{\Delta m_{32}^2}$ test statistic.

$ \Delta m_{32}^2 /10^{-3} \text{ eV}^2$		Confidence
Low bound	High bound	
0.0	3.5	1σ
0.0	4.1	90%
0.0	4.3	2σ
0.0	5.0	3σ

Lower limit of the confidence interval extracted using $t_{\Delta m_{32}^2}$ is driven by the data points at E_{tt} energies higher than 400 MeV (see Figure 5.7), where the effect of oscillations is expected to be small. Additionally, data in that region is systematically higher than the expected MC value (see Figure 5.4). The probability that data points in six consecutive bins is higher than the true value due to statistical fluctuations is $2^{-6} \approx 1.7\%$, compatible with the p -value for the null-hypothesis of no oscillations obtained in the analysis. Therefore this is most probably the effect of systematic effects not accounted for, which cause the underestimation of expected NC-like/CC-like ratio in the MC simulation.

The test statistic $q_{\Delta m_{32}^2}$ is by construction invariant to effects driving the lower limit, so the upper limit on mass splitting obtained from it may be safely considered a conservative limit on the $|\Delta m_{32}^2|$ value obtained from this analysis.

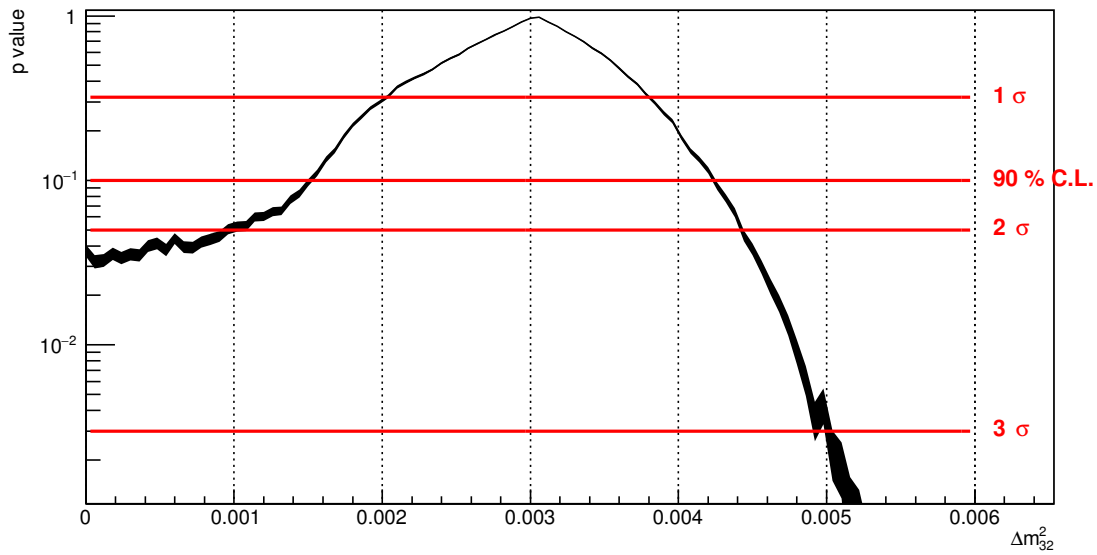


Figure 5.3: A plot of p -values (black line) using test statistic $t_{\Delta m_{32}^2}$ as a function of different null-hypothesis values of Δm_{32}^2 . Vertical width of the p -value line is the 90% confidence interval, where the uncertainty on its value is a consequence of the fact that p -values were calculated using finitely many pseudo-experiments. Red lines are four thresholds on the p -value, below which the null-hypothesis can be rejected by a predefined probability. Detailed explanation can be found in the text.

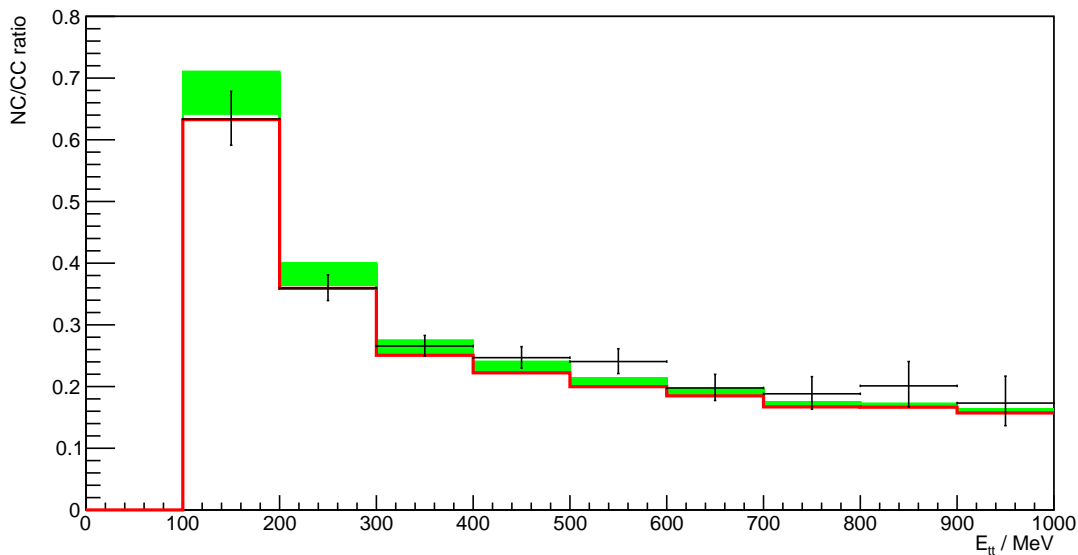


Figure 5.4: The distribution of NC-like/CC-like ratio obtained by the upper limit analysis using $t_{\Delta m_{32}^2}$. The green area is a 90% confidence interval quoted in Table 5.4. The red line is the distribution under no oscillation hypothesis. The crosses are data, their vertical width is approximate 68% C.L. of $P_{lk}(x)$ distribution defined in equation 5.16. The excluded lower limit is barely visible because of the quadratic dependence of oscillation probability on $|\Delta m_{32}^2|$.

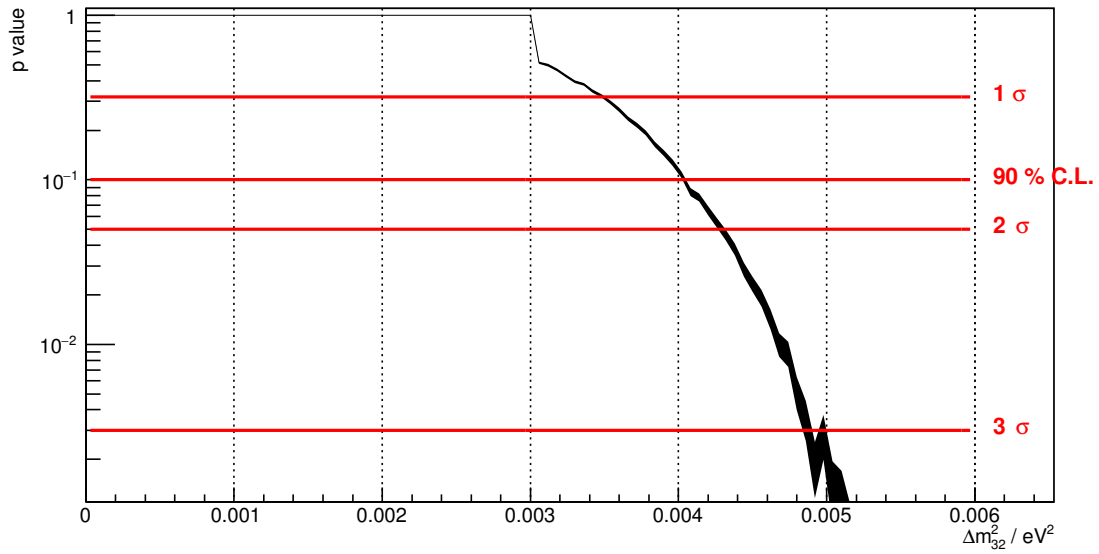


Figure 5.5: A plot of p -values (black line) using test statistic $q_{\Delta m_{32}^2}$ as a function of different null-hypothesis values of Δm_{32}^2 . Vertical width of the p -value line is the 90% confidence interval, where the uncertainty on its value is a consequence of the fact that p -values were calculated using finitely many pseudo-experiments. Red lines are four thresholds on the p -value, below which the null-hypothesis can be rejected by a predefined probability. Detailed explanation can be found in the text.

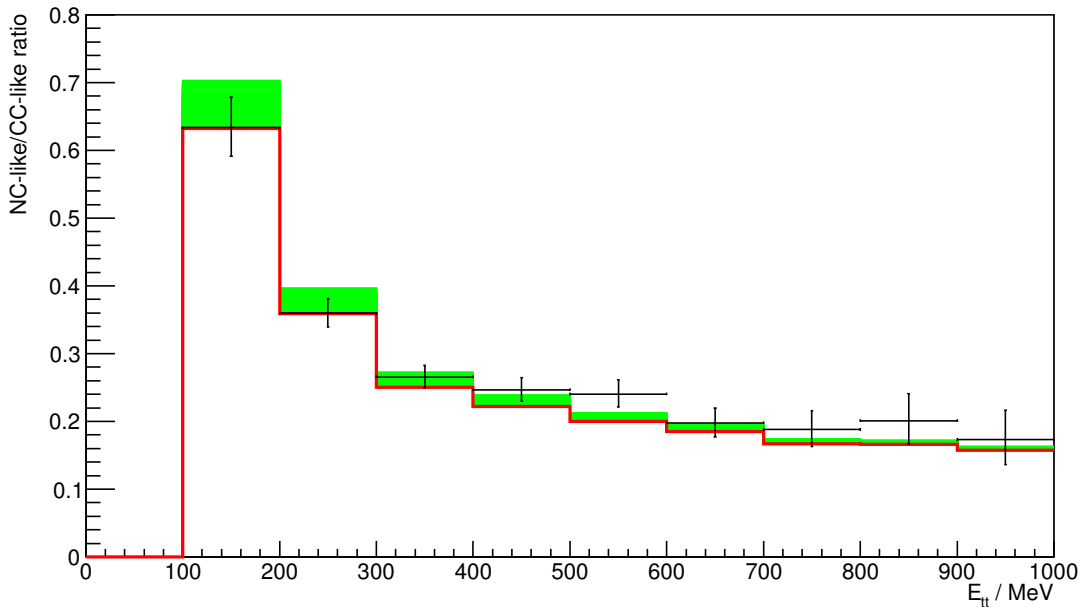
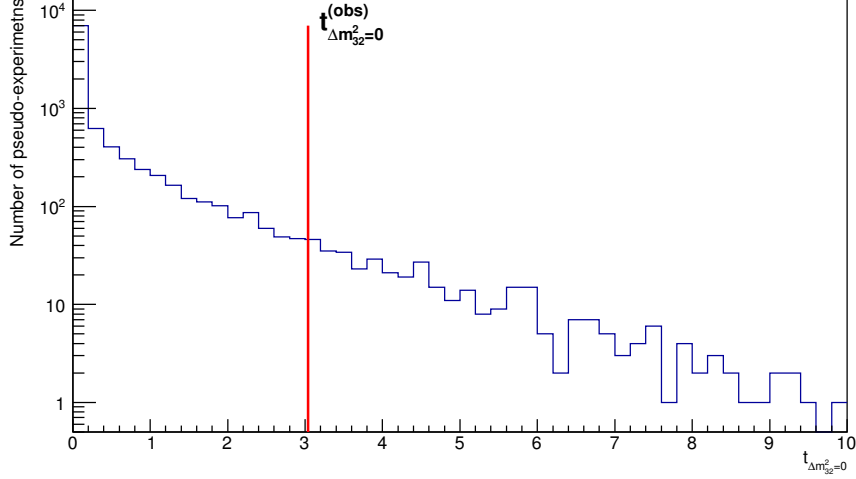
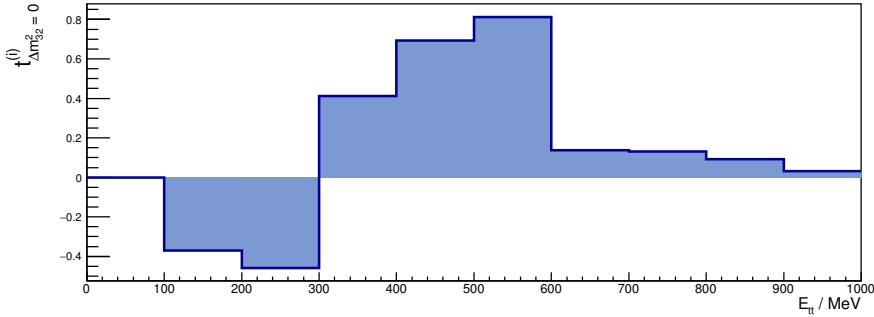


Figure 5.6: The distribution of NC-like/CC-like ratio obtained by the upper limit analysis using $q_{\Delta m_{32}^2}$. The green area is a 90% confidence interval quoted in Table 5.4. The red line is the distribution under no oscillation hypothesis. The crosses are data, their vertical width is approximate 68% C.L. of $P_{lk}(x)$ distribution defined in equation 5.16.



(a) The histogram of $t_{\Delta m_{32}^2=0}$ sample obtained by pseudo-experiments. Red line is the observed value $t_{\Delta m_{32}^2=0}^{(\text{obs})}$ of the test statistic. The p -value is calculated by dividing the number of pseudo-experiments yielding $t_{\Delta m_{32}^2=0} > t_{\Delta m_{32}^2=0}^{(\text{obs})}$ with the total number of pseudo-experiments. Thus, the p -value is smaller when $t_{\Delta m_{32}^2=0}^{(\text{obs})}$ is larger.



(b) Contribution of each E_{tt} bin to the total value of $t_{\Delta m_{32}^2=0}^{(\text{obs})}$. Values larger than zero indicate that no-oscillation hypothesis is less compatible with data than the best fit, while those lower than zero indicate that no-oscillation hypothesis is more compatible with data. The sum of these bin values is the observed $t_{\Delta m_{32}^2=0}^{(\text{obs})}$ (the total is always larger than zero by construction). The largest contribution to the total observed test statistic is coming from bins $E_{tt} > 400$ MeV, which means they are actually responsible for excluding $\Delta m_{32}^2 = 0$.

Figure 5.7: Distribution of $t_{\Delta m_{32}^2=0}$ and the contribution to $t_{\Delta m_{32}^2=0}^{(\text{obs})}$ from each E_{tt} histogram bin.

5.4.1 Effect of the beam uncertainty on the measurement

To investigate whether systematic effects on the lower limit of the confidence interval are induced by the uncertainty in the CNGS beam flux, a dedicated analysis was performed in which the smearing of the original neutrino flux was implemented.

To implement the uncorrelated smearing of the original neutrino spectrum, the full set of simulated neutrino events has been divided into subsets (bins) according to true neutrino energy. The bins were 10 GeV wide, and the weight of every event in a single bin was multiplied by the same Gaussian random number with the mean value of 1 and standard deviation of 0.15. Event weights in different bins were multiplied by different random numbers from the same Gaussian distribution. In this way, a set of 1000 different smeared fluxes have been generated.

The likelihood function has been modified to take into account these multiple smeared fluxes as follows:

$$L(\Delta m_{32}^2) = \prod_{i=1}^N \left(\frac{1}{M} \sum_{j=1}^M P_{\text{NC}_i/\text{CC}_i} \left(R_i^{(j)}(\Delta m_{32}^2) \right) \right), \quad (5.27)$$

where M is a number of smeared fluxes, and $R_i^{(j)}(\Delta m_{32}^2)$ is a MC predicted NC-like over CC-like event ratio in the i -th E_{tt} bin obtained using j -th smeared input flux. The factor $1/M$ is introduced simply to obtain a similar normalization of the modified likelihood function w.r.t. the original one, but is otherwise irrelevant to the analysis¹³.

The test statistic distributions have been constructed using pseudo-experiments, where pseudo-data sets have been constructed from the original (unsmeared) MC sample. This is consistent with the fact that there is only one data set, while the uncertainty is in the MC simulation.

Results of this procedure are shown in the Figures 5.8 and 5.9. The pink line shows the results of the smeared analysis, and the black line results of the original analysis. The effect of the beam smearing is small enough to be neglected compared to the statistical uncertainty in the data.

¹³Likelihood function may be in general multiplied by an arbitrary real number without affecting the results of this analysis since multiplicative factors cancel in the equation (5.3)

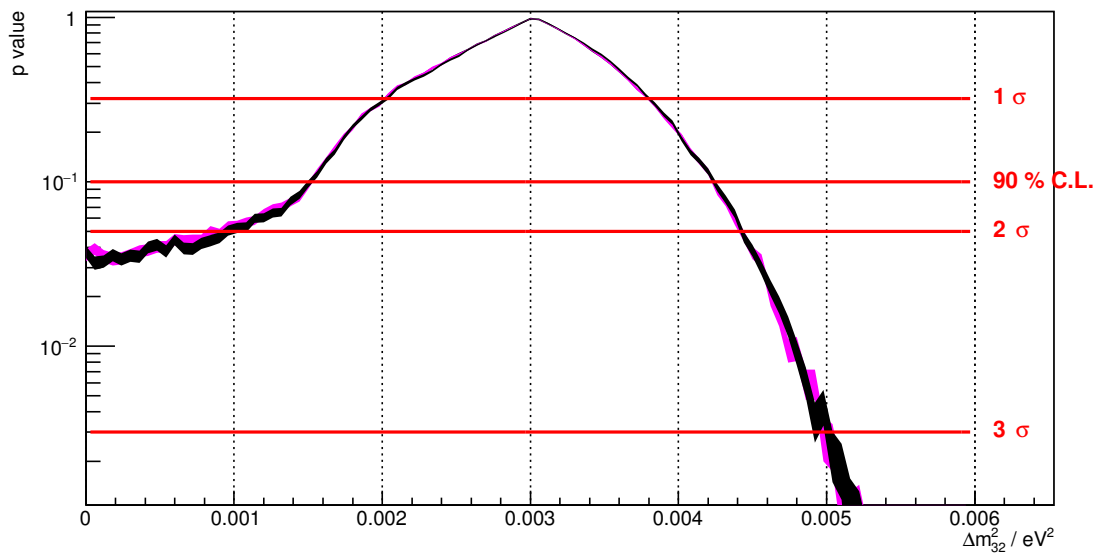


Figure 5.8: A plot of p -values using test statistic $t_{\Delta m_{32}^2}$ as a function of different null-hypothesis values of Δm_{32}^2 . Vertical width of the p -value line is the 90% confidence interval, where the uncertainty on its value is a consequence of the fact that p -values were calculated using finitely many pseudo-experiments. Red lines are four thresholds on the p -value, below which the null-hypothesis can be rejected by a predefined probability. Pink line corresponds to the smeared MC and the black one is the original MC.

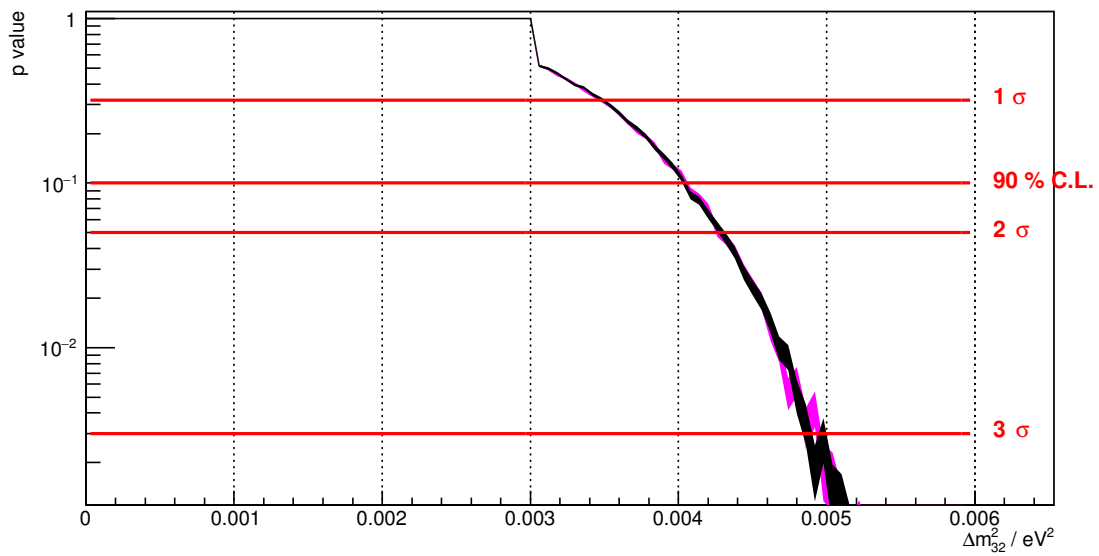


Figure 5.9: A plot of p -values using test statistic $q_{\Delta m_{32}^2}$ as a function of different null-hypothesis values of Δm_{32}^2 . Vertical width of the p -value line is the 90% confidence interval, where the uncertainty on its value is a consequence of the fact that p -values were calculated using finitely many pseudo-experiments. Red lines are four thresholds on the p -value, below which the null-hypothesis can be rejected by a predefined probability. Pink line corresponds to the smeared MC and the black one is the original MC.

Chapter 6

Conclusions

The OPERA experiment was designed to directly observe $\nu_\mu \rightarrow \nu_\tau$ appearance and it accomplished this physical goal. This was achieved using the high energy CNGS ν_μ beam which was optimized for tau appearance rather than measurement of neutrino oscillation parameters. In particular the lack of a near detector, unnecessary for tau appearance search, severely limits the knowledge of the initial ν_μ flux since the only available neutrino spectra are a result of a MC simulation rather than measurements. These facts make measurement of neutrino oscillation parameters via $\nu_\mu \rightarrow \nu_\mu$ disappearance quite difficult. The uncertainty of beam normalization was mitigated below the statistical error by using NC interactions observed in the OPERA detector as a way to effectively measure the flux. Even with this large reduction of systematic uncertainty, the signal of neutrino oscillations is too small compared to residual discrepancy between data and MC to exclude the no-oscillation hypothesis. An upper limit of $|\Delta m_{32}^2| < 4.1 \cdot 10^{-3} \text{ eV}^2$ at 90 % confidence level was obtained in this work.

The dedicated Monte Carlo simulation was produced using an up-to-date interaction generator and simulating all neutrino interaction channels inside and outside of OPERA detector to properly evaluate the contribution of external events to the total event rate. This simulation was also used by the OPERA Collaboration to constrain neutrino oscillation parameters $|\Delta m_{32}^2|$ and $\sin^2 \theta_{13}$ in $\nu_\mu \rightarrow \nu_\tau$ and $\nu_\mu \rightarrow \nu_e$ oscillation channels respectively.

The 90 % confidence intervals on the constrained oscillation parameters are listed in Table 6.1.

Table 6.1: 90 % confidence intervals of neutrino oscillation parameters obtained by the OPERA experiment

Oscillation parameter	Lower limit	Upper limit	Dominant oscillation channel
$ \Delta m_{32}^2 / 10^{-3} \text{ eV}^2$	2.0	5.0	$\nu_\mu \rightarrow \nu_\tau$
$ \Delta m_{32}^2 / 10^{-3} \text{ eV}^2$	0.0	4.1	$\nu_\mu \rightarrow \nu_\mu$
$\sin^2 \theta_{13}$	0.0	0.12	$\nu_\mu \rightarrow \nu_e$

These results are compatible with the global fit values quoted in the Table 2.4.

The OPERA experiment has published the oscillation physics results for all three possible oscillation channels of a single neutrino flavour. A publication combining all neutrino oscillation physics results obtained by the OPERA experiment is in preparation within the Collaboration, in which the work presented here will be one of the three main components.

Bibliography

- [1] A. Gando et al. “Reactor On-Off Antineutrino Measurement with KamLAND”. In: *Phys. Rev.* D88.3 (2013), p. 033001. DOI: 10.1103/PhysRevD.88.033001. arXiv: 1303.4667 [hep-ex] (cit. on pp. iii, 24, 31, 37, 40).
- [2] F. P. An et al. “New Measurement of Antineutrino Oscillation with the Full Detector Configuration at Daya Bay”. In: *Phys. Rev. Lett.* 115.11 (2015), p. 111802. DOI: 10.1103/PhysRevLett.115.111802. arXiv: 1505.03456 [hep-ex] (cit. on pp. iii, iv, 41, 42).
- [3] F. P. An et al. “New measurement of θ_{13} via neutron capture on hydrogen at Daya Bay”. In: *Phys. Rev.* D93.7 (2016), p. 072011. DOI: 10.1103/PhysRevD.93.072011. arXiv: 1603.03549 [hep-ex] (cit. on pp. iii, 41).
- [4] J. H. Choi et al. “Observation of Energy and Baseline Dependent Reactor Antineutrino Disappearance in the RENO Experiment”. In: *Phys. Rev. Lett.* 116.21 (2016), p. 211801. DOI: 10.1103/PhysRevLett.116.211801. arXiv: 1511.05849 [hep-ex] (cit. on pp. iii, iv, 41).
- [5] Y. Abe et al. “Measurement of ϑ_{13} in Double Chooz using neutron captures on hydrogen with novel background rejection techniques”. In: *JHEP* 01 (2016), p. 163. DOI: 10.1007/JHEP01(2016)163. arXiv: 1510.08937 [hep-ex] (cit. on pp. iii, 41).
- [6] K. Abe et al. “Observation of Electron Neutrino Appearance in a Muon Neutrino Beam”. In: *Phys. Rev. Lett.* 112 (2014), p. 061802. DOI: 10.1103/PhysRevLett.112.061802. arXiv: 1311.4750 [hep-ex] (cit. on pp. iii, 41).
- [7] P. Adamson et al. “Electron neutrino and antineutrino appearance in the full MINOS data sample”. In: *Phys. Rev. Lett.* 110.17 (2013), p. 171801. DOI: 10.1103/PhysRevLett.110.171801. arXiv: 1301.4581 [hep-ex] (cit. on pp. iii, 41).

- [8] N. Agafonova et al. “Search for $\nu_\mu \rightarrow \nu_e$ oscillations with the OPERA experiment in the CNGS beam”. In: *JHEP* 07 (2013), p. 004. DOI: 10.1007/JHEP07(2013)004. arXiv: 1303.3953 [hep-ex] (cit. on pp. iii, 41, 61). Addendum in: *JHEP* 07 (2013), p. 085. DOI: 10.1007/JHEP07(2013)085.
- [9] N. Agafonova et al. “Final results of the search for $\nu_\mu \rightarrow \nu_e$ oscillations with the OPERA detector in the CNGS beam”. In: (2018). arXiv: 1803.11400 [hep-ex] (cit. on pp. iii, 41, 61, 79, 85).
- [10] P. Adamson et al. “First measurement of muon-neutrino disappearance in NOvA”. In: *Phys. Rev. D* 93.5 (2016), p. 051104. DOI: 10.1103/PhysRevD.93.051104. arXiv: 1601.05037 [hep-ex] (cit. on pp. iv, 41).
- [11] K. Abe et al. “Precise Measurement of the Neutrino Mixing Parameter θ_{23} from Muon Neutrino Disappearance in an Off-Axis Beam”. In: *Phys. Rev. Lett.* 112.18 (2014), p. 181801. DOI: 10.1103/PhysRevLett.112.181801. arXiv: 1403.1532 [hep-ex] (cit. on pp. iv, 41).
- [12] P. Adamson et al. “Combined analysis of ν_μ disappearance and $\nu_\mu \rightarrow \nu_e$ appearance in MINOS using accelerator and atmospheric neutrinos”. In: *Phys. Rev. Lett.* 112 (2014), p. 191801. DOI: 10.1103/PhysRevLett.112.191801. arXiv: 1403.0867 [hep-ex] (cit. on pp. iv, 41, 43).
- [13] M. G. Aartsen et al. “Determining neutrino oscillation parameters from atmospheric muon neutrino disappearance with three years of IceCube DeepCore data”. In: *Phys. Rev. D* 91.7 (2015), p. 072004. DOI: 10.1103/PhysRevD.91.072004. arXiv: 1410.7227 [hep-ex] (cit. on pp. iv, 41).
- [14] N. Agafonova et al. “Discovery of τ Neutrino Appearance in the CNGS Neutrino Beam with the OPERA Experiment”. In: *Phys. Rev. Lett.* 115.12 (2015), p. 121802. DOI: 10.1103/PhysRevLett.115.121802. arXiv: 1507.01417 [hep-ex] (cit. on pp. iv, 43, 58–60, 79).
- [15] N. Agafonova et al. “Final results of the OPERA experiment on ν_τ appearance in the CNGS beam”. In: *Phys. Rev. Lett.* 120.21 (2018), p. 211801. DOI: 10.1103/PhysRevLett.120.211801. arXiv: 1804.04912 [hep-ex] (cit. on pp. iv, 60, 79, 85).

- [16] *CNGS beam profile*. CERN. 2016. URL: <http://www.mi.infn.it/~psala/Icarus/cngs.html> (visited on 05/23/2018) (cit. on pp. iv, 70).
- [17] J. A. Formaggio and G. P. Zeller. “From eV to EeV: Neutrino Cross Sections Across Energy Scales”. In: *Rev. Mod. Phys.* 84 (2012), pp. 1307–1341. DOI: 10.1103/RevModPhys.84.1307. arXiv: 1305.7513 [hep-ex] (cit. on pp. 4, 11).
- [18] F. Vannucci. “Interactions of neutrinos with matter”. In: *Prog. Part. Nucl. Phys.* 95 (2017), pp. 1–47. DOI: 10.1016/j.pnpnp.2017.03.003 (cit. on pp. 4, 24).
- [19] Carlo Giunti and Chung W. Kim. *Fundamentals of Neutrino Physics and Astrophysics*. Oxford, UK: Univ. Pr. (2007) 710 p, 2007. ISBN: 9780198508717. DOI: 10.1093/acprof:oso/9780198508717.001.0001 (cit. on pp. 12, 20, 28).
- [20] S. Schael et al. “Precision electroweak measurements on the Z resonance”. In: *Phys. Rept.* 427 (2006), pp. 257–454. DOI: 10.1016/j.physrep.2005.12.006. arXiv: hep-ex/0509008 [hep-ex] (cit. on p. 20).
- [21] C. Patrignani et al. “Review of Particle Physics”. In: *Chin. Phys.* C40.10 (2016), p. 100001. DOI: 10.1088/1674-1137/40/10/100001. And 2017 update. (Cit. on pp. 20, 24, 28, 29, 33, 35, 41).
- [22] Aldo M. Serenelli, W. C. Haxton, and Carlos Pena-Garay. “Solar models with accretion. I. Application to the solar abundance problem”. In: *Astrophys. J.* 743 (2011), p. 24. DOI: 10.1088/0004-637X/743/1/24. arXiv: 1104.1639 [astro-ph.SR] (cit. on p. 27).
- [23] M. Honda et al. “Atmospheric neutrino flux calculation using the NRLMSISE-00 atmospheric model”. In: *Phys. Rev.* D92.2 (2015), p. 023004. DOI: 10.1103/PhysRevD.92.023004. arXiv: 1502.03916 [astro-ph.HE] (cit. on p. 30).
- [24] Y. Fukuda et al. “The Super-Kamiokande detector”. In: *Nucl. Instrum. Meth.* A501 (2003), pp. 418–462. DOI: 10.1016/S0168-9002(03)00425-X (cit. on p. 30).
- [25] M. Sajjad Athar et al. “India-based Neutrino Observatory: Project Report. Volume I.” In: 2006. URL: <http://www.imsc.res.in/~ino/OpenReports/INOReport.pdf> (cit. on p. 30).

- [26] M. Agostini et al. “Spectroscopy of geoneutrinos from 2056 days of Borexino data”. In: *Phys. Rev.* D92.3 (2015), p. 031101. DOI: 10.1103/PhysRevD.92.031101. arXiv: 1506.04610 [hep-ex] (cit. on p. 31).
- [27] Itaru Shimizu. “Past and Present Experiments of Geoneutrinos”. In: *Phys. Procedia* 61 (2015), pp. 355–358. DOI: 10.1016/j.phpro.2014.12.075 (cit. on p. 31).
- [28] G. Fiorentini et al. “Mantle geoneutrinos in KamLAND and Borexino”. In: *Phys. Rev.* D86 (2012), p. 033004. DOI: 10.1103/PhysRevD.86.033004. arXiv: 1204.1923 [hep-ph] (cit. on p. 31).
- [29] C. L. Cowan et al. “Detection of the Free Neutrino: a Confirmation”. In: *Science* 124.3212 (1956), pp. 103–104. ISSN: 0036-8075. DOI: 10.1126/science.124.3212.103 (cit. on p. 33).
- [30] Carlo Bemporad, Giorgio Gratta, and Petr Vogel. “Reactor based neutrino oscillation experiments”. In: *Rev. Mod. Phys.* 74 (2002), p. 297. DOI: 10.1103/RevModPhys.74.297. arXiv: hep-ph/0107277 [hep-ph] (cit. on pp. 34, 35).
- [31] Q. R. Ahmad et al. “Direct evidence for neutrino flavor transformation from neutral current interactions in the Sudbury Neutrino Observatory”. In: *Phys. Rev. Lett.* 89 (2002), p. 011301. DOI: 10.1103/PhysRevLett.89.011301. arXiv: nucl-ex/0204008 [nucl-ex] (cit. on p. 36).
- [32] B. Aharmim et al. “Combined Analysis of all Three Phases of Solar Neutrino Data from the Sudbury Neutrino Observatory”. In: *Phys. Rev.* C88 (2013), p. 025501. DOI: 10.1103/PhysRevC.88.025501. arXiv: 1109.0763 [nucl-ex] (cit. on p. 36).
- [33] R. Wendell et al. “Atmospheric neutrino oscillation analysis with sub-leading effects in Super-Kamiokande I, II, and III”. In: *Phys. Rev.* D81 (2010), p. 092004. DOI: 10.1103/PhysRevD.81.092004. arXiv: 1002.3471 [hep-ex] (cit. on p. 41).
- [34] C. Sirignano. “R&D on OPERA ECC: studies on emulsion handling and event reconstruction techniques”. PhD thesis. University of Salerno, 2006 (cit. on p. 49).
- [35] C. Bozza et al. “An integrated system for large scale scanning of nuclear emulsions”. In: *Nucl. Instrum. Meth.* A703 (2013), pp. 204–212. DOI: 10.1016/j.nima.2012.11.099 (cit. on p. 49).

- [36] N. Agafonova et al. “Evidence for $\nu_\mu \rightarrow \nu_\tau$ appearance in the CNGS neutrino beam with the OPERA experiment”. In: *Phys. Rev.* D89.5 (2014), p. 051102. DOI: 10.1103/PhysRevD.89.051102. arXiv: 1401.2079 [hep-ex] (cit. on pp. 50, 58).
- [37] N. Agafonova et al. “Momentum measurement by the Multiple Coulomb Scattering method in the OPERA lead emulsion target”. In: *New J. Phys.* 14 (2012), p. 013026. DOI: 10.1088/1367-2630/14/1/013026. arXiv: 1106.6211 [physics.ins-det] (cit. on p. 51).
- [38] R. Acquafredda et al. “The OPERA experiment in the CERN to Gran Sasso neutrino beam”. In: *JINST* 4 (2009), P04018. DOI: 10.1088/1748-0221/4/04/P04018 (cit. on pp. 52–54, 57).
- [39] M. Ambrosio et al. “The OPERA magnetic spectrometer”. In: *IEEE Trans. Nucl. Sci.* 51 (2004), pp. 975–979. DOI: 10.1109/TNS.2004.829659. arXiv: physics/0409137 [physics] (cit. on p. 52).
- [40] N. Agafonova et al. “Determination of the muon charge sign with the dipolar spectrometers of the OPERA experiment”. In: *JINST* 11.07 (2016), P07022. DOI: 10.1088/1748-0221/11/07/P07022. arXiv: 1404.5933 [physics.ins-det] (cit. on p. 52).
- [41] N. Agafonova et al. “The Detection of neutrino interactions in the emulsion/lead target of the OPERA experiment”. In: *JINST* 4 (2009), P06020. DOI: 10.1088/1748-0221/4/06/P06020. arXiv: 0903.2973 [hep-ex] (cit. on pp. 55, 58).
- [42] N. Agafonova et al. “Observation of a first ν_τ candidate in the OPERA experiment in the CNGS beam”. In: *Phys. Lett.* B691 (2010), pp. 138–145. DOI: 10.1016/j.physletb.2010.06.022. arXiv: 1006.1623 [hep-ex] (cit. on p. 58).
- [43] N. Agafonova et al. “New results on $\nu_\mu \rightarrow \nu_\tau$ appearance with the OPERA experiment in the CNGS beam”. In: *JHEP* 11 (2013), p. 036. DOI: 10.1007/JHEP11(2013)036. arXiv: 1308.2553 [hep-ex] (cit. on pp. 58, 60, 121). Erratum in: *JHEP* 04 (2014), p. 014. DOI: 10.1007/JHEP04(2014)014.

- [44] N. Agafonova et al. “Observation of tau neutrino appearance in the CNGS beam with the OPERA experiment”. In: *PTEP* 2014.10 (2014), p. 101C01. DOI: 10.1093/ptep/ptu132. arXiv: 1407.3513 [hep-ex] (cit. on p. 58).
- [45] N. Agafonova et al. “Procedure for short-lived particle detection in the OPERA experiment and its application to charm decays”. In: *Eur. Phys. J. C* 74.8 (2014), p. 2986. DOI: 10.1140/epjc/s10052-014-2986-0. arXiv: 1404.4357 [hep-ex] (cit. on p. 59).
- [46] A. Longhin, A. Paoloni, and F. Pupilli. “Large-angle scattering of multi-GeV muons on thin Lead targets”. In: *IEEE Trans. Nucl. Sci.* 62.5 (2015), pp. 2216–2225. DOI: 10.1109/TNS.2015.2473674. arXiv: 1506.08759 [physics.ins-det] (cit. on p. 59).
- [47] M. Guler et al. *An appearance experiment to search for $\nu_\mu \leftrightarrow \nu_\tau$ oscillations in the CNGS beam: experimental proposal*. Tech. rep. CERN-SPSC-2000-028. LNGS-2000-25. SPSC-P-318. Geneva: CERN, July 2000. URL: <http://cds.cern.ch/record/456523> (cit. on p. 60).
- [48] C. Andreopoulos et al. “The GENIE Neutrino Monte Carlo Generator”. In: *Nucl. Instrum. Meth.* A614 (2010), pp. 87–104. DOI: 10.1016/j.nima.2009.12.009. arXiv: 0905.2517 [hep-ph] (cit. on p. 70).
- [49] I. Hrivnacova et al. “The Virtual Monte Carlo”. In: *eConf* C0303241 (2003), THJT006. arXiv: cs/0306005 [cs-se] (cit. on p. 72).
- [50] R. Brun et al. *GEANT 3: user’s guide Geant 3.10, Geant 3.11; rev. version*. Geneva: CERN, 1987. URL: <https://cds.cern.ch/record/1119728> (cit. on p. 72).
- [51] Pierre Billoir. “Track Fitting With Multiple Scattering: A New Method”. In: *Nucl. Instrum. Meth.* A225 (1984), pp. 352–366. DOI: 10.1016/0167-5087(84)90274-6 (cit. on p. 79).
- [52] N. Agafonova et al. “Study of neutrino interactions with the electronic detectors of the OPERA experiment”. In: *New J. Phys.* 13 (2011), p. 053051. DOI: 10.1088/1367-2630/13/5/053051. arXiv: 1102.1882 [hep-ex] (cit. on p. 79).

- [53] A. Bertolin and N. T. Tran. *OpCarac: an algorithm for the classification of the neutrino interactions recorded by OPERA*. OPERA public note 100. Aug. 2009. URL: <http://operaweb.lngs.infn.it/Opera/publicnotes/note100.pdf> (cit. on p. 79).
- [54] N. Agafonova et al. “Study of charged hadron multiplicities in charged-current neutrino–lead interactions in the OPERA detector”. In: *Eur. Phys. J. C* 78.1 (2018), p. 62. DOI: 10.1140/epjc/s10052-017-5509-y. arXiv: 1706.07930 [hep-ex] (cit. on pp. 79, 82).
- [55] G. Cowan. *Statistical Data Analysis*. Oxford science publications. Clarendon Press, 1998. ISBN: 9780198501558. URL: <https://books.google.hr/books?id=ff8ZyW0n1JAC> (cit. on p. 88).
- [56] G. Cowan et al. “Asymptotic formulae for likelihood-based tests of new physics”. In: *Eur. Phys. J. C* 71 (2011), p. 1554. DOI: 10.1140/epjc/s10052-011-1554-0. arXiv: 1007.1727 [physics.data-an] (cit. on p. 89). Erratum in: *Eur. Phys. J. C* 73 (2013), p. 2501. DOI: 10.1140/epjc/s10052-013-2501-z.
- [57] A. Ferrari, A. Guglielmi, and P. R. Sala. “CNGS neutrino beam systematics for theta(13)”. In: *Nucl. Phys. Proc. Suppl.* 145 (2005). [93(2005)], pp. 93–97. DOI: 10.1016/j.nuclphysbps.2005.03.042. arXiv: hep-ph/0501283 [hep-ph] (cit. on p. 90).
- [58] *Gamma Distribution*. Wolfram MathWorld. 2018. URL: <http://mathworld.wolfram.com/GammaDistribution.html> (visited on 05/23/2018) (cit. on p. 92).
- [59] Edmond L. Berger et al. “The Minimum Invariant Mass: A Technique for Heavy Quark Searches at Collider Energy”. In: *Phys. Lett.* 140B (1984), pp. 259–263. DOI: 10.1016/0370-2693(84)90931-6 (cit. on p. 120).

Appendix A

OPERA tau candidate selection cuts

Tau candidate selection in the OPERA emulsion is defined by hard cuts on several kinematical parameters which can be reconstructed in the ECC brick.

Primary vertex is a vertex in which CC interaction has occurred. Tracks emerging from the primary vertex are called **primaries**.

Secondary vertex is a vertex in which short primary track called **parent** decays. Tracks emerging from secondary vertex are called **daughters**.

The global selection criterion is that there must be no muon or electron tracks emerging from the primary vertex. If this is the case, selection is made on the following parameters:

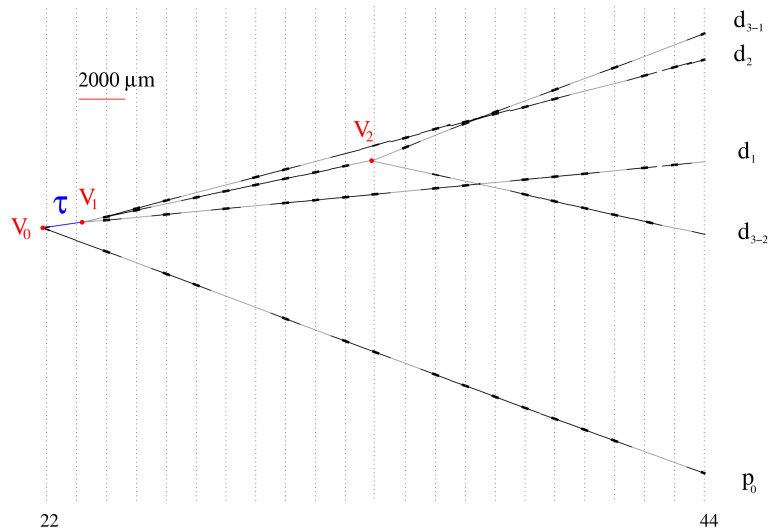
- z_{dec} : shortest distance between the decay vertex position and the downstream face of lead plate in which interaction occurred. Cut on this variable ensures that tau tracks are neither too short nor too long, excluding hadronic reinteraction and large angle scatterings of primaries.
- p_T^{miss} : beam transverse component of the vectorial sum of all particles from both vertices except the parent.
- $p_T^{2\text{ry}}$: transverse momentum component of the daughter wrt. the parent direction. Applicable only to 1-prong decays.
- $p^{2\text{ry}}$: scalar sum of all daughter momenta.
- θ_{kink} : kink angle - the average 3D angle between the parent and daughters.

- m : invariant mass of daughters assuming they all have mass of π meson.
- m_{\min} : the minimal invariant mass as defined in [59].
- Φ_{IH} : this parameters is defined for vector components of track momenta in the plane perpendicular to the beam axis, called transverse components. It is the angle between transverse component of parent momentum and a transverse component of vectorial sum of all other primary particles. This variable is intended to make use of the fact that in CC neutrino scatterings charged lepton and hadronic system are back-to-back in beam transverse plane. For an example see Figure A.1.

Selection cuts on these variables for different tau decay channels are shown in Table A.1.

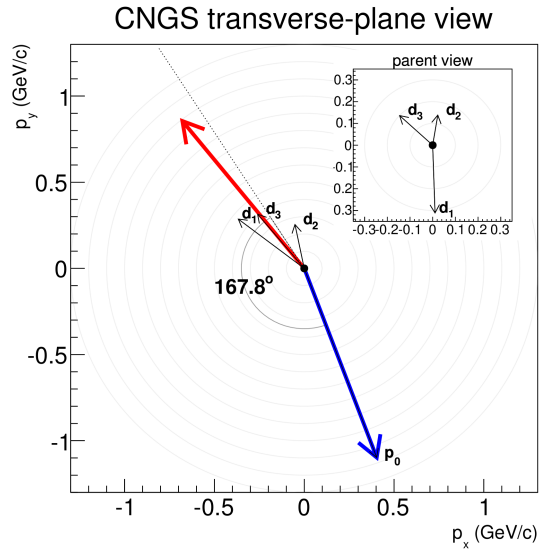
Table A.1: OPERA tau candidate selection cuts. Cut marked with a * is applied when there is a gamma photon attached to the secondary vertex.

Parameter	$\tau \rightarrow 1h$	$\tau \rightarrow 3h$	$\tau \rightarrow \mu$	$\tau \rightarrow e$
$z_{\text{dec}}/\mu\text{m}$	$44 < z_{\text{dec}} < 2600$	< 2600	$44 < z_{\text{dec}} < 2600$	< 2600
$p_T^{\text{miss}}/\text{GeV}$	< 1	< 1	-	-
$p_T^{2\text{ry}}/\text{GeV}$	> 0.6 (0.3)*	-	> 0.25	> 0.1
$p^{2\text{ry}}/\text{GeV}$	> 2	< 3	$1 < p^{2\text{ry}} < 15$	$1 < p^{2\text{ry}} < 15$
$\theta_{\text{kink}}/\text{mrad}$	> 20	< 500	> 20	> 20
m/GeV	-	$0.5 < m < 2$	-	-
m_{\min}/GeV	-	$0.5 < m_{\min} < 2$	-	-
$\Phi_{\text{IH}}/\text{rad}$	$> \pi/2$	$> \pi/2$	-	-



(a) ECC reconstruction of the 2nd tau candidate. Tau neutrino exhibits CC interaction in a lead plate, producing tau lepton (track τ) and a hadron (track \mathbf{p}_0). Tau lepton decays into three hadron tracks \mathbf{d}_1 , \mathbf{d}_2 , \mathbf{d}_3 . Particle associated with the track \mathbf{d}_3 interacts 1.4 cm downstream of the secondary vertex, producing two hadron tracks and four back-scattered nuclear fragments^a (not visible in the display). Vertical dotted lines are emulsion plates. Track segments measured in emulsion plates are shown as short thick lines superimposed to reconstructed particle tracks.

^aThis is how it is known that it was a hadronic reinteraction and not particle decay.



(b) Beam transverse view of the event. Primary hadron and tau daughter tracks measured transverse momenta are shown. Dotted line is a direction of tau candidate track^a. Red arrow line is a vectorial sum of daughter momenta. By definition, Φ_{IH} is an angle between \mathbf{p}_0 and tau direction (dotted line). In this case it is determined to be 167.8° . Inset shows the projections of three daughter momenta to parent track (tau) transverse plane.

^aIt is impossible to measure its momentum because the track is too short.

Figure A.1: Reconstruction of the second OPERA tau candidate event. The observed event is in the $\tau \rightarrow 3h + \nu_\tau$ decay channel. Figures are taken from [43].

Appendix B

Confidence intervals for the binomial distribution

Binomial distribution is given by the formula:

$$P_B(k|p, N) = \binom{N}{k} p^k (1-p)^{N-k} . \quad (\text{B.1})$$

Suppose one can measure the values of k and N and wishes to infer the value of p . The best estimate of the value of p is given by the formula

$$\hat{p} = \frac{k}{N} . \quad (\text{B.2})$$

To obtain the confidence intervals around this central value, one may find the probability density function of p given k and N using Bayes theorem with a flat prior:

$$P_B(p|k, N) = \frac{1}{N} P_B(k|p, N) = \frac{1}{N} \frac{N!}{k!(N-k)!} p^k (1-p)^{N-k} . \quad (\text{B.3})$$

This is a special case of beta distribution

$$P_\beta(x; \alpha, \beta) = \frac{\Gamma(\alpha + \beta)}{\Gamma(\alpha)\Gamma(\beta)} x^{\alpha-1} (1-x)^{\beta-1} , \quad (\text{B.4})$$

with parameters $x = p$, $\alpha = k + 1$ and $\beta = N - k + 1$.

The cumulative density function of P_β is defined as

$$D_\beta(x; \alpha, \beta) = \int_0^x P_\beta(x'; \alpha, \beta) dp' . \quad (\text{B.5})$$

To obtain a symmetrical confidence interval of confidence level β and significance $\alpha = 1 - \beta$, one must solve the following equations:

$$D_\beta(p_-, k + 1, N - k + 1) = \frac{\alpha}{2} , \quad (\text{B.6a})$$

$$D_\beta(p_+, k + 1, N - k + 1) = 1 - \frac{\alpha}{2} , \quad (\text{B.6b})$$

where p_- and p_+ are lower and upper limits, respectively, of the confidence interval.

In practice, these equations are easily solved with the knowledge of the inverse of the cumulative distribution D_β :

$$Q_\beta(x; \alpha, \beta) = D_\beta^{-1}(x; \alpha, \beta) , \quad (\text{B.7})$$

which is available in the standard ROOT mathematics package.

The symmetrical confidence interval, except for the special cases of $k = 0$ or $k = N$ is then given by:

$$p_- = Q_\beta(\alpha/2; k + 1, N - k + 1) , \quad (\text{B.8a})$$

$$p_+ = Q_\beta(1 - \alpha/2; k + 1, N - k + 1) . \quad (\text{B.8b})$$

In the case $k = 0$, the confidence interval is constructed as one-sided CL:

$$p_- = 0 , \quad (\text{B.9a})$$

$$p_+ = Q_\beta(1 - \alpha; k + 1, N - k + 1) , \quad (\text{B.9b})$$

and similarly for the case $k = N$:

$$p_- = Q_\beta(\alpha; k + 1, N - k + 1) , \quad (\text{B.10a})$$

$$p_+ = 1 . \quad (\text{B.10b})$$

Appendix C

Photograph of OPERA using OPERA nuclear emulsion

A photograph of the OPERA detector within the Hall C of the LNGS underground laboratory was made by Donato di Ferdinando from the University of Bologna, a member of the OPERA Collaboration. The photograph was made using a hand-made pinhole camera constructed from an aluminium cola can pierced by a sewing needle. The emulsion was exposed for 30 hours. The photograph is shown in Figure C.1.

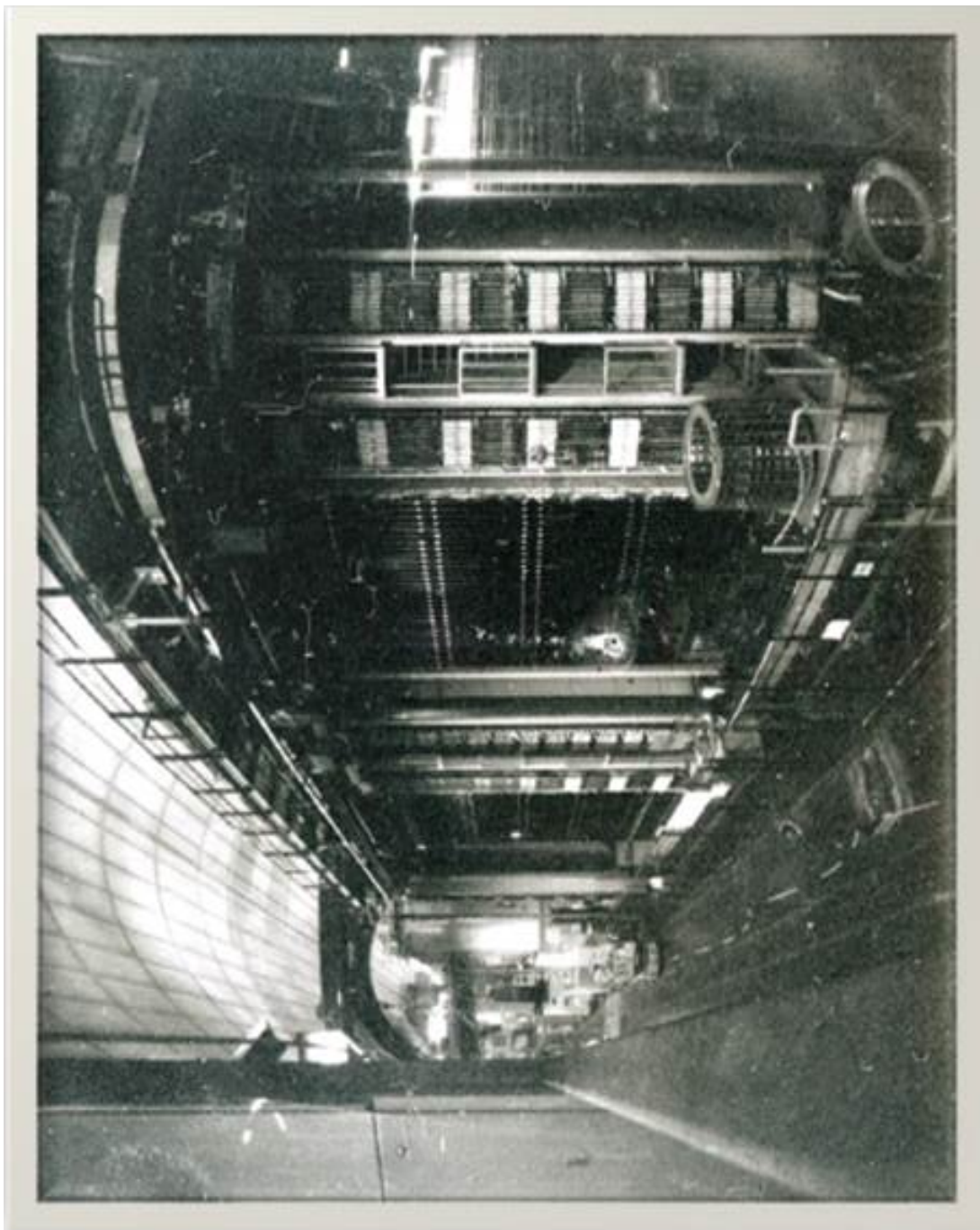


Figure C.1: A photograph of the OPERA detector using OPERA nuclear emulsion made by Donato di Ferdinando from the University of Bologna. Used with permission from the author.

Curriculum vitae

Budimir Kliček was born in Varaždin (Croatia) in 1983. He graduated from high-school in 2001, earning an occupational title of a Computer technician. During his high-school senior year, he was awarded the first prize in the experimental physics competition of senior high school students on a national level. In 2001 he started his undergraduate study of Physics at the Faculty of science, University of Zagreb (Croatia). In 2007 he joined the OPERA experiment as an undergraduate student, working on the slow control system of the OPERA electronic detectors. He earned his Master of Physics degree in 2009 with a master thesis titled "Determination of electroweak mixing angle using neutrino interactions". He entered the PHD programme in particle physics at the Faculty of science, University of Zagreb in 2009. He is employed at the Ruđer Bošković Institute since 2009, holding a position of an research associate. He continued his OPERA activities by doing various shifts at the experiment, most notably being the youngest Run Coordinator within the Collaboration, a duty he performed frequently since 2010 until the end of the OPERA data taking run in 2012. Since 2011 he is a full representative of the Zagreb group in the OPERA Collaboration Board. In 2012 he became in charge of the working group within the OPERA Collaboration tasked with producing the software framework for simulation of event location and reconstruction in the OPERA ECC detectors, a project he successfully brought to completion. In 2017 he applied for funding, under the ESSnuSB Collaboration and within the Horizon 2020 framework, for the design study of the next major neutrino experiment in Europe. The funding was granted and he is currently the leader of the Ruđer Bošković Institute group within the ESSnuSB, working on neutrino detector design.

List of publications

- [1] R. Acquafredda et al. “The OPERA experiment in the CERN to Gran Sasso neutrino beam”. In: *JINST* 4 (2009), P04018. DOI: 10.1088/1748-0221/4/04/P04018.
- [2] N. Agafonova et al. “The Detection of neutrino interactions in the emulsion/lead target of the OPERA experiment”. In: *JINST* 4 (2009), P06020. DOI: 10.1088/1748-0221/4/06/P06020. arXiv: 0903.2973 [hep-ex].
- [3] N. Agafonova et al. “Measurement of the atmospheric muon charge ratio with the OPERA detector”. In: *Eur. Phys. J. C* 67 (2010), pp. 25–37. DOI: 10.1140/epjc/s10052-010-1284-8. arXiv: 1003.1907 [hep-ex].
- [4] N. Agafonova et al. “Observation of a first ν_τ candidate in the OPERA experiment in the CNGS beam”. In: *Phys. Lett. B* 691 (2010), pp. 138–145. DOI: 10.1016/j.physletb.2010.06.022. arXiv: 1006.1623 [hep-ex].
- [5] A. Bertolin et al. “Long term performances of OPERA bakelite RPC system”. In: *Nucl. Instrum. Meth. A* 661 (2012), S60–S63. DOI: 10.1016/j.nima.2010.08.090.
- [6] N. Agafonova et al. “Study of neutrino interactions with the electronic detectors of the OPERA experiment”. In: *New J. Phys.* 13 (2011), p. 053051. DOI: 10.1088/1367-2630/13/5/053051. arXiv: 1102.1882 [hep-ex].
- [7] N. Agafonova et al. “Momentum measurement by the Multiple Coulomb Scattering method in the OPERA lead emulsion target”. In: *New J. Phys.* 14 (2012), p. 013026. DOI: 10.1088/1367-2630/14/1/013026. arXiv: 1106.6211 [physics.ins-det].
- [8] N. Agafonova et al. “Search for $\nu_\mu \rightarrow \nu_\tau$ oscillation with the OPERA experiment in the CNGS beam”. In: *New J. Phys.* 14 (2012), p. 033017. DOI: 10.1088/1367-2630/14/3/033017.
- [9] N. Yu. Agafonova et al. “Determination of a time-shift in the OPERA set-up using high energy horizontal muons in the LVD and OPERA detectors”. In: *Eur. Phys. J. Plus* 127 (2012), p. 71. DOI: 10.1140/epjp/i2012-12071-5. arXiv: 1206.2488 [hep-ex].

- [10] T. Adam et al. “Measurement of the neutrino velocity with the OPERA detector in the CNGS beam”. In: *JHEP* 10 (2012), p. 093. DOI: 10.1007/JHEP10(2012)093. arXiv: 1109.4897 [hep-ex].
- [11] T. Adam et al. “Measurement of the neutrino velocity with the OPERA detector in the CNGS beam using the 2012 dedicated data”. In: *JHEP* 01 (2013), p. 153. DOI: 10.1007/JHEP01(2013)153. arXiv: 1212.1276 [hep-ex].
- [12] N. Agafonova et al. “Search for $\nu_\mu \rightarrow \nu_e$ oscillations with the OPERA experiment in the CNGS beam”. In: *JHEP* 07 (2013), p. 004. DOI: 10.1007/JHEP07(2013)004. arXiv: 1303.3953 [hep-ex]. Addendum in: *JHEP* 07 (2013), p. 085. DOI: 10.1007/JHEP07(2013)085.
- [13] N. Agafonova et al. “New results on $\nu_\mu \rightarrow \nu_\tau$ appearance with the OPERA experiment in the CNGS beam”. In: *JHEP* 11 (2013), p. 036. DOI: 10.1007/JHEP11(2013)036. arXiv: 1308.2553 [hep-ex]. Erratum in: *JHEP* 04 (2014), p. 014. DOI: 10.1007/JHEP04(2014)014.
- [14] N. Agafonova et al. “Evidence for $\nu_\mu \rightarrow \nu_\tau$ appearance in the CNGS neutrino beam with the OPERA experiment”. In: *Phys. Rev. D* 89.5 (2014), p. 051102. DOI: 10.1103/PhysRevD.89.051102. arXiv: 1401.2079 [hep-ex].
- [15] N. Agafonova et al. “Measurement of the TeV atmospheric muon charge ratio with the complete OPERA data set”. In: *Eur. Phys. J. C* 74 (2014), p. 2933. DOI: 10.1140/epjc/s10052-014-2933-0. arXiv: 1403.0244 [hep-ex].
- [16] N. Agafonova et al. “Procedure for short-lived particle detection in the OPERA experiment and its application to charm decays”. In: *Eur. Phys. J. C* 74.8 (2014), p. 2986. DOI: 10.1140/epjc/s10052-014-2986-0. arXiv: 1404.4357 [hep-ex].
- [17] N. Agafonova et al. “Observation of tau neutrino appearance in the CNGS beam with the OPERA experiment”. In: *PTEP* 2014.10 (2014), p. 101C01. DOI: 10.1093/ptep/ptu132. arXiv: 1407.3513 [hep-ex].
- [18] N. Agafonova et al. “Limits on muon-neutrino to tau-neutrino oscillations induced by a sterile neutrino state obtained by OPERA at the CNGS beam”. In: *JHEP* 06 (2015), p. 069. DOI: 10.1007/JHEP06(2015)069. arXiv: 1503.01876 [hep-ex].

- [19] N. Agafonova et al. “Discovery of τ Neutrino Appearance in the CNGS Neutrino Beam with the OPERA Experiment”. In: *Phys. Rev. Lett.* 115.12 (2015), p. 121802. DOI: 10.1103/PhysRevLett.115.121802. arXiv: 1507.01417 [hep-ex].
- [20] A. Anokhina et al. “Search for sterile neutrinos in muon neutrino disappearance mode at FNAL”. In: *Eur. Phys. J. C* 77.1 (2017), p. 23. DOI: 10.1140/epjc/s10052-016-4569-8. arXiv: 1503.07471 [hep-ph].
- [21] N. Agafonova et al. “Determination of the muon charge sign with the dipolar spectrometers of the OPERA experiment”. In: *JINST* 11.07 (2016), P07022. DOI: 10.1088/1748-0221/11/07/P07022. arXiv: 1404.5933 [physics.ins-det].
- [22] N. Agafonova et al. “Study of charged hadron multiplicities in charged-current neutrino–lead interactions in the OPERA detector”. In: *Eur. Phys. J. C* 78.1 (2018), p. 62. DOI: 10.1140/epjc/s10052-017-5509-y. arXiv: 1706.07930 [hep-ex].
- [23] N. Agafonova et al. “Final results of the OPERA experiment on ν_τ appearance in the CNGS beam”. In: *Phys. Rev. Lett.* 120.21 (2018), p. 211801. DOI: 10.1103/PhysRevLett.120.211801. arXiv: 1804.04912 [hep-ex].